Tiago André Nogueira Morgado

TAILORING THE NEAR- AND FAR- FIELDS
WITH WIRE MEDIA

UNIVERSIDADE DE COIMBRA

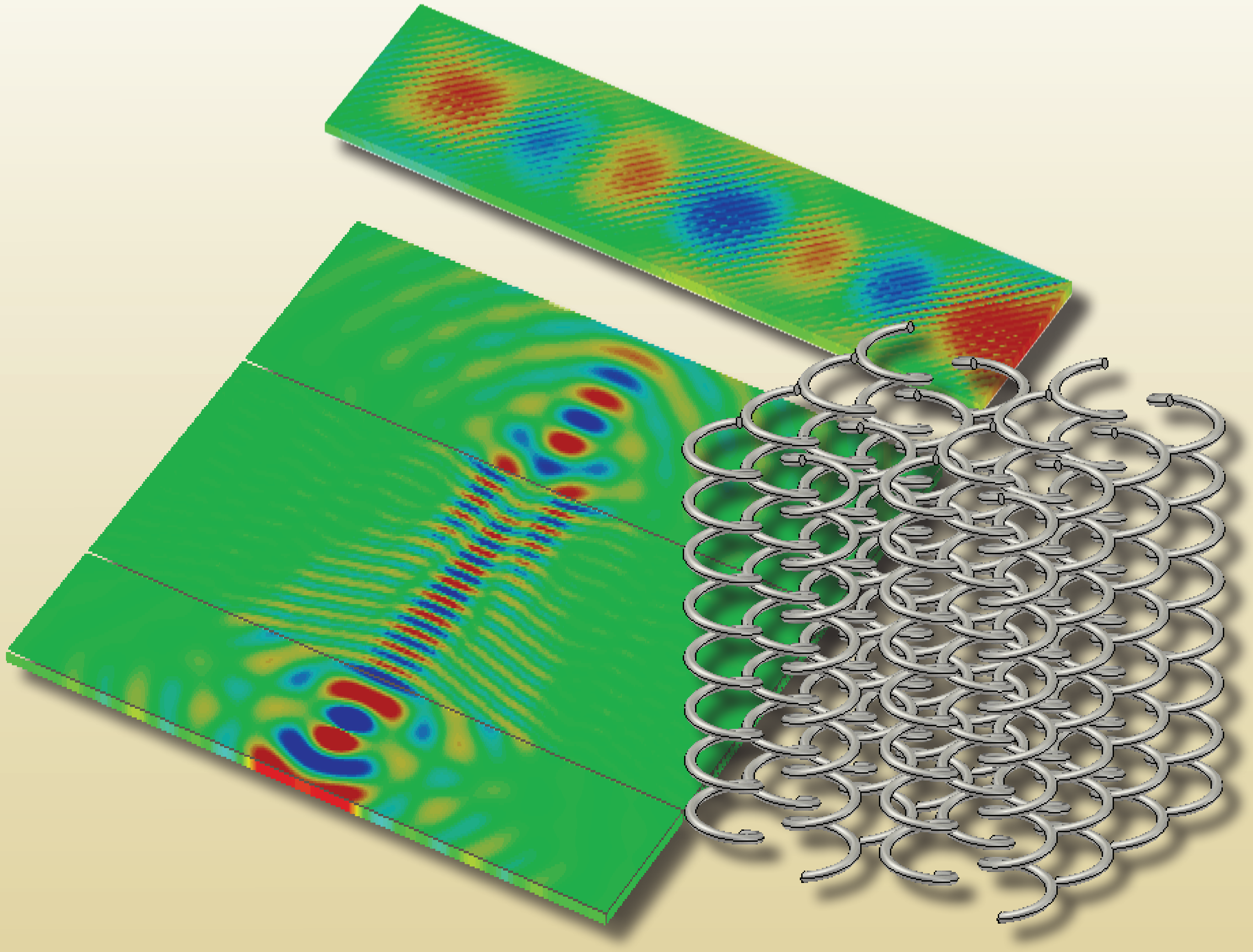

Tiago André Nogueira Morgado

TAILORING THE NEAR- AND FAR- FIELDS WITH WIRE MEDIA

Volume I

Dissertação de Doutoramento na área científica de Engenharia Electrotécnica e de Computadores, especialidade de Telecomunicações, orientada pelo Doutor Mário Gonçalo Mestre Veríssimo Silveirinha da FCTUC/IT, e apresentada ao Departamento de Engenharia Electrotécnica e de Computadores da Faculdade de Ciências e Tecnologia da Universidade de Coimbra.

Setembro de 2011

· U C ·

UNIVERSIDADE DE COIMBRA

To all those who make me who I am

“Para ser grande, sê inteiro: nada
Teu exagera ou exclui.
Sê todo em cada coisa. Põe quanto és
No mínimo que fazes.
Assim como em cada lago a lua toda
Brilha, porque alta vive.”

(Ricardo Reis, heterónimo de Fernando Pessoa, 1888-1935)

“To be great, be whole: exclude nothing,
Exaggerate nothing that is not you.
Be whole in everything. Put all you are
Into the smallest thing you do.
So, in each lake, the moon shines with splendor
Because it blooms up above.”

(Ricardo Reis, Fernando Pessoa’s heteronym, 1888-1935)

Abstract

Over the years, there has been a growing interest in the design of artificial structured materials (known as “metamaterials”) that may interact in a controlled and desired way with electromagnetic radiation. Among the variety of media belonging to the class of metamaterials, a structure that has attracted significant attention due to its interesting potentials in the manipulation of electromagnetic fields is that formed by arrays of parallel metallic wires, known as "wire medium".

This thesis is devoted to the analytical, numerical and experimental study of structured materials formed by arrays of metallic wires (not necessarily straight wires). The main topics that are studied are near-field transport and manipulation, negative refraction and far-field focusing, and subwavelength waveguiding.

The possibility of near-field transport using an array of tilted metallic wires is analytically and numerically investigated. It is demonstrated that wire media may enable the restoration of the electric field component parallel to the wires at the image plane, even when there is no electric field normal to interface. Moreover, we experimentally verified the full reconstruction (both in amplitude and phase) of the near-field using a lens formed by tilted wires. This suggests exciting applications for the tilted wire medium lens in near-field measurement.

The phenomenon of negative refraction and the prospects of far-field focusing are investigated in two different wire medium configurations. Firstly, we demonstrate analytically and numerically that an array of helical shaped metallic wires (or helices) may be regarded as a local uniaxial Epsilon-Negative (ENG) material even when the conductivity of the metal is very large (e.g., in the microwave regime) and, as a result, enables a strong negative refraction over a wide frequency range. Then, taking advantage of the negative refraction, we demonstrate partial focusing of electromagnetic radiation using a planar lens formed by such composite material. On the other hand, the phenomenon of negative refraction and the related far-field focusing effect are also investigated in a spatially dispersive material formed by nonconnected crossed metallic wires. It is analytically, as well as numerically and experimentally demonstrated that a flat slab of such structured material may also provide partial focusing of electromagnetic radiation. Quite interestingly, it is shown that, in this case, the strength of the negative refraction effect can be controlled by changing the angle between the two sets of parallel metallic wires.

A very promising route to achieve broadband and ultra-subwavelength waveguiding (e.g., at infrared, terahertz and microwave frequencies) is proposed. The idea is to couple the electromagnetic radiation to the spatially induced charge density waves supported by strongly coupled grids of metallic wires. It is shown both theoretically and experimentally that the characteristic spatial scale of these mesoscopic excitations (which are designated as "interlaced plasmons") is determined by geometrical features, rather than from the electrical length of the metal elements, and that due to their wide band nature, weak sensitivity to metallic absorption, and subwavelength mode sizes, such spatially induced plasmons may have exciting applications in waveguiding in the nanoscale.

Keywords

Metamaterials, Wire Media, Spatial Dispersion, Subwavelength Imaging, Negative Refraction, Partial Focusing, Subwavelength Waveguiding.

Resumo

Ao longo dos anos tem havido um interesse crescente em materiais artificialmente estruturados (designados por "metamateriais") que interajam de uma forma controlada e desejada com a radiação electromagnética. Entre a variedade de meios pertencentes à classe dos metamateriais, uma estrutura que tem atraído grande interesse em virtude das suas potencialidades na manipulação dos campos electromagnéticos é aquela formada por agregados de fios metálicos paralelos, designada por *wire medium*.

Esta tese é dedicada ao estudo analítico, numérico e experimental de materiais estruturados formados por agregados de fios metálicos (não necessariamente fios rectos). Os principais tópicos estudados são o transporte e manipulação do campo próximo, a refracção negativa e focagem de campo distante, e o guiamento sub-λ (λ representa o comprimento de onda) de ondas electromagnéticas.

A possibilidade de transporte do campo próximo usando um agregado de fios metálicos inclinados é investigada analiticamente e numericamente. É demonstrado que os agregados de fios (*wire media*) permitem a restauração da componente do campo eléctrico paralela aos fios, mesmo quando não existe campo eléctrico incidente normal à interface. Para além disso, demonstra-se experimentalmente a reconstrução total do campo próximo (amplitude e fase) utilizando uma lente de fios inclinados. Tal resultado sugere aplicações muito interessantes para a lente de fios inclinados na medição do campo próximo.

Em seguida, investiga-se o fenómeno da refracção negativa e a focagem do campo distante em duas configurações diferentes de agregados de fios. Em primeiro lugar, demonstra-se analiticamente e numericamente que um agregado de fios metálicos em forma helicoidal (ou hélices) se comporta como um meio local uniaxial com permitividade negativa (*ENG*) mesmo quando a condutividade do metal é muito grande (como acontece para frequências microondas). Como consequência, este meio estruturado possibilita uma refracção negativa forte numa banda de frequências larga. Em seguida, tirando partido da refracção negativa, demonstra-se um efeito de focagem parcial da radiação usando uma lente formada por fios helicoidais e com interfaces planas. Por outro lado, investiga-se também o fenómeno da refracção negativa e focagem do campo distante num meio com forte dispersão espacial formado por agregados de fios metálicos cruzados e não conectados. Demonstra-se analiticamente, bem como numericamente e experimentalmente que uma lente formada por tal material estruturado com interfaces planas também possibilita uma focagem parcial da radiação. De forma muito interessante, demonstra-se que neste caso a intensidade da refracção negativa pode ser controlada através da alteração do ângulo entre os dois conjuntos de fios metálicos paralelos.

Por último, propõe-se uma nova e promissora forma de conseguir guiamento sub-λ e de banda-larga de ondas electromagnéticas nas bandas de frequências de microondas, terahertz e infra-vermelho. A ideia é acoplar a radiação electromagnética às ondas de densidade de carga espacialmente induzidas que são suportadas por grelhas de fios metálicos fortemente acopladas. É demonstrado, tanto teoricamente como experimentalmente, que o período espacial característico destas excitações mesoscópicas (que são designadas como "plasmons entrelaçados") é determinado por características geométricas, e não pelo comprimento eléctrico dos elementos metálicos. O facto de estas excitações existirem numa banda-larga de frequências, a sua fraca sensibilidade à absorção metálica, e a sua dimensão característica sub-λ fazem com que os plasmons espacialmente induzidos possam ter aplicações promissoras no guiamento de ondas electromagnéticas na nano-escala.

Palavras-Chave

Metamateriais, *Wire Media*, Dispersão Espacial, *Imaging* Sub-λ, Refracção Negativa, Focagem Parcial, Guiamento Sub-λ de Ondas Electromagnéticas.

Preface

This dissertation is the result of work carried out under the supervision of Prof. Mário Silveirinha, at Instituto de Telecomunicações – Coimbra and Department of Electrical and Computer Engineering of the Faculty of Sciences and Technology of the University of Coimbra between October 2007 and August 2011. The originality of this thesis is sustained in a series of journal and conference papers that have been published while I was studying for my PhD. Future publications are still in order regarding some sections of the thesis. Except where explicit reference is made to the work of others, the work contained in this dissertation is my own.

Acknowledgments

Building up a doctoral thesis is not a lonely adventure, but an exciting journey full of challenges, experiences and discoveries that would be impossible without the crucial help of many people. Thus, it is fair to express here my most profound and sincere gratitude to all those who helped make this thesis possible.

In the first place, I want to express my deepest gratitude to my supervisor Prof. Mário Silveirinha for giving me such a unique opportunity to discover a whole new world, which has broadened my personal and professional horizons immensely. This thesis would never have been possible without his constant encouragement, endless support, and invaluable guidance. I consider myself very fortunate to have had the opportunity to study all these years under the tutelage of such a great person and scientist, and I will always have profound feelings of gratitude and admiration towards him.

I also want to express my huge gratitude to Dr. Stanislav Maslovski for all his help and valuable suggestions to my work. He was like a co-supervisor of my research work with whom I have had the great privilege to learn and work over the last three years.

I am also thankful to all my colleagues and friends of the Microwave Laboratory. Especially, I am immeasurably grateful to my dear friend João Costa for his endless friendship and constant presence during all these years. I cannot forget at this moment everything we have lived over these long years since the beginning of our undergraduate studies. I am also very thankful to João Marcos for his vital help in the fabrication of the prototypes as well as with the experimental measurements.

I also want to thank all my close friends for being there whenever I need them. They have also been an important part during these years.

I deeply want to express my gratitude to my family, especially my mother, father, brother, sister and nephew, for their endless love, constant understanding and care. Without them this would not have ever been possible or worthwhile. I am also very grateful to my relatives in Brazil, especially Silvério and Laura, whose absence makes my heart grow fonder. Very especially, this work is also dedicated to the memory of my grandparents and my cousin Dagoberto, who have always been a great source of inspiration to me.

Last but not least, very special thanks go to my girlfriend, Cristina, for bringing me a new and special shine to my life, and for all the support and encouragement she has given me especially during the writing of this thesis.

Finally, I would like to fully acknowledge the technical and financial support of *Instituto de Telecomunicações – Pólo de Coimbra* in the person of its coordinator Prof. Henrique Silva, as well as the financial support during these four years of research of the *Fundação para a Ciência e Tecnologia* under the fellowship SFRH/BD/37876/2007.

Contents

List of Symbols

a	Lattice period
r_w	Wire radius
L	Slab thickness
L_w	Length of the wires
p	Helix pitch
R	Helix radius
V_{cell}	Volume of the unit cell
f_v	Volume fraction
$\mathbf{E}$	Electric field vector
$\mathbf{H}$	Magnetic field vector
$\mathbf{J}_{\mathrm{d,av}}$	Averaged microscopic current
$\mathbf{S}$	Poynting vector
ρ	Reflection coefficient
t	Transmission coefficient
ε_0	Permittivity of free-space
μ_0	Permeability of free-space
ε_r	Relative permittivity
μ_r	Relative permeability
ε_t	Relative permittivity along the transverse direction
ε_h	Relative permittivity of the dielectric host

ε_{eff}	Effective (relative) permittivity
ε_m	Complex permittivity of the metal
ω	Angular frequency
f	Frequency
c	Speed of light in vacuum
λ_0	Wavelength in free-space
λ_h	Wavelength in the dielectric host
k_0	Wave number in free-space
γ_0	Free-space propagation constant
$\mathbf{k}$	Wave vector
(k_x, k_y, k_z)	Components of the wave vector
(x, y, z)	Position coordinates
$\mathbf{r}$	Spatial coordinate vector
$\hat{\mathbf{u}}_i$	Unit vector along the *i*-direction
$\bar{\bar{\mathbf{I}}}$	Identity dyadic
β_p	Plasma wave number
n_{eff}	Effective index of refraction
v_g	Group velocity
w_0	Gaussian beam waist
Δ	Spatial shift of the Gaussian beam
j	Imaginary unit ($\sqrt{-1}$)

I. INTRODUCTION

I.1. Overview

Nowadays, controlling and manipulating electromagnetic waves is essential in a broad variety of technologies and applications including telecommunication networks, and imaging and sensing systems. Lenses and optical fibers are some examples of important instruments developed for this purpose. These established devices exploit the interaction between electromagnetic waves and their constituent materials in order to achieve advantageous electromagnetic responses.

Over the last years, however, a tremendous technological progress in several different areas has placed challenging demands related to the properties of materials. The desired electromagnetic responses are, in most cases, beyond the reach of naturally available materials. In fact, the electromagnetic properties of the materials directly available in nature correspond to a small subset of the physically realizable electromagnetic responses, implying that sometimes it may not be possible to find a natural material with the desired electromagnetic response. Hence, the study and design of artificial structured materials with tailor-made and often hitherto unattainable electromagnetic responses has been sought during the last years, stimulated by a continuous improvement of the characterization and fabrication technologies.

Photonic and electromagnetic crystals (or band-gap materials) [1-4] are one of the examples of artificial structured media developed over the last twenty years that may go beyond the limitations of conventional materials. They consist of periodic arrangements of dielectric or metal-dielectric elements. Similar to semiconductor materials in which the periodic potential affects the electron motion by creating allowed and forbidden electronic energy bands, in photonic and electromagnetic crystals the periodically distributed refractive index results in frequency band-gaps where the propagation of electromagnetic waves is forbidden. This anomalous response gives rise to multiple opportunities. The first reported application of photonic crystals was the inhibition of the spontaneous emission [1, 5]. Later, photonic crystals have proven to be useful in many other applications such as waveguide and resonator components [6-9], antennas setups [10-11], lasing systems [12-14], etc.

In photonic crystals, the periodicity of the structure has to be comparable with the radiation wavelength ($a \approx \lambda$, where a is the lattice period of the crystal and λ the wavelength) so that electromagnetic waves undergo diffraction effects and, as a consequence, there are electromagnetic band-gaps. On one hand, such requirement strongly restricts the range of frequencies where the structure can be operated. On the other hand, it precludes the treatment of the structure as a homogeneous material, and hence, the homogenization approach is not the most convenient way to describe the electromagnetic response of photonic crystals.

A more recent and perhaps even more revolutionary development in the field of artificial structured materials goes by the name of metamaterials. This relatively new class of artificial materials typically consists of dielectric or metallic inclusions properly tailored in shape and size and arranged in a regular lattice, similarly to photonic crystals. However, unlike photonic crystals, the unit cell of metamaterials is much smaller than the wavelength of radiation ($a << \lambda$). Hence, in contrast to photonic crystals and somehow similar to conventional solid-state materials, the waves which pass through a metamaterial see the medium as a bulk material, or in other words, the waves do not feel the granularity of the material. Therefore, metamaterials can be characterized by physically meaningful homogenized constitutive parameters, i.e., effective permittivities and permeabilities [15-16].

The main difference between metamaterials and standard solid-state materials is that the electromagnetic properties of such man-made materials are mainly determined by the geometry of the constitutive materials (inclusions), rather from the chemical composition of the constituent basic units. Hence, metamaterials offer a tremendous flexibility and an uncountable number of degrees of freedom in terms of possibly realizable electromagnetic responses. As a result, such microstructured composites may enable a meticulous and powerful manipulation of the electromagnetic fields and consequently an unprecedented control of the propagation of electromagnetic waves.

Complex materials with anomalous properties such as negative index of refraction [17-19], high index of refraction [20-23], extreme anisotropy [24], or near zero permittivity [25] have been a topic of intense research, mainly due to the possibility of overcoming the resolution and miniaturization barriers imposed by diffraction effects. This is known as diffraction limit and it is the major obstacle to the imaging of the fine details of an object source, as well as to the confinement and concentration of energy in small volumes. Nevertheless, it has been demonstrated that unlike what was believed before, the diffraction limit does not strictly prohibit spatial resolution and field confinement smaller than half of wavelength ($\lambda/2$). This opens exciting new possibilities in several fields such as the realization of imaging devices with super-resolution [24, 26-27], fabrication of compact subwavelength waveguides and cavities [28-30], realization of recording media with ultrahigh storage capacity [31], delivery and concentration (nanofocusing) of the optical energy on the nanoscale [32], just to name a few.

An important class of metamaterials consists of periodic arrays of metallic wires. Such “wire media” have attracted considerable attention mainly due to their potentials in transporting and manipulating the electromagnetic radiation in the subwavelength scale [24, 31, 33-35]. Moreover, several other interesting opportunities such as superlensing [36-38] and negative refraction [39-40] were reported in recent works. In this thesis, we investigate in detail novel potential applications of metamaterials structures formed by arrays of metallic wires (not necessarily straight wires). The electromagnetic problems are initially analyzed and discussed from a theoretical perspective using analytical models, and subsequently, numerically validated. Finally, using the insights given by the analytical and numerical approaches, we design and test experimentally the proposed solutions.

Throughout this work the time dependence $e^{j\omega t}$ is assumed.

I.2. Organization of the Thesis

The thesis is organized in 5 chapters and 1 appendix.

In Chapter II, we investigate the near-field imaging capabilities of a metamaterial lens formed by tilted metallic wires. In order to provide sufficient background to this study, we start the chapter by reviewing some of the most well-known and relevant near-field imaging mechanisms. After this review, we address the problem of plane wave reflection and refraction at the interfaces of a metamaterial slab formed by tilted metallic wires using a nonlocal homogenization model and full-wave simulations. Moreover, we study the potentials of near-field transport of the proposed lens in different scenarios and for different source polarizations. In the last part of this chapter, we investigate theoretically and experimentally the possibility of reconstructing all the near-field Cartesian components of the electric field at the image plane by using the proposed tilted wire medium lens.

The third chapter of the thesis is dedicated to the study of the related topics of negative refraction and far-field focusing in two different metamaterial structures formed by metallic wires. In the first part of the chapter (Sec. III.2), the electromagnetic response of a structured material formed by helical shaped wires (or helices) is thoroughly investigated using a developed analytical model based on homogenization theory and numerical simulations. In particular, the effective parameters of the composite material, as well as the band structures and the isofrequency contours are analytically and numerically characterized. In addition, the transmission characteristics of finite-thickness slabs formed by helical shaped wires are also characterized using the proposed analytical model and full-wave simulations. Then, in Sec. III.2.4.3 we investigate the refraction of a Gaussian beam at the interfaces of the considered metamaterial slab. Finally, in Sec. III.2.5 we numerically study the imaging of a magnetic line source by a flat slab made of helical shaped wires. On the other hand, in Sec. III.3 we study the phenomenon of negative refraction in a crossed wire mesh of nonconnected metallic wires, and the possibility of taking advantage of this effect to obtain partial focusing. Specifically, in Sec. III.3.4 we investigate analytically, as well as numerically and experimentally, the possibility of using a flat slab of the considered structured material to produce a partial focusing of the electromagnetic radiation. Finally, in Sec. III.3.5 we discuss theoretically and numerically a strategy to boost the negative refraction effect in the crossed wire mesh.

In Chapter IV, we discuss the possibility of trapping and guiding the radiation field far beyond the diffraction limit in an ultra-compact waveguide made of two mutually orthogonal and nonconnected meshes of parallel metallic wires. Specifically, we study the dispersion properties of the surface wave modes supported by the considered metamaterial slab for a configuration with magnetic field perpendicular to both the arrays of wires and the direction of propagation (TM guided modes). In a first stage, we discuss heuristically the physical nature of these transverse magnetic guided modes. After this, we analyze analytically and numerically the dispersion characteristic of the guided modes, firstly assuming perfectly electric conducting (PEC) wires and then considering realistic metals (specifically, Ag wires). Finally, in Sec. IV.3.5, the dispersion properties of the TM guided modes supported by the structured slab are experimentally verified at microwaves using a fabricated prototype.

In chapter V, the main conclusions of this work are outlined, as well as some future work. In Appendix A we study the transverse magnetic modes supported by a crossed wire grid formed by sets of wires perpendicular and parallel to the interface plane.

I.3. Main Contributions

The key contributions of the present thesis are:

- Improvement of the polarization sensitivity of the wire medium lenses.
- Establishment of a simple and practical method to fully restore the near-field radiated by an arbitrary source using a tilted wire medium lens.
- Establishment of a new way to suppress the spatial dispersion effects that are inherent to wire media at microwave and low infrared frequencies by using helical shaped wires.
- Demonstration of all-angle broadband negative refraction and partial focusing of electromagnetic radiation with a flat slab formed by helical shaped metallic wires.

- Demonstration that a spatially dispersive material formed by nonconnected crossed metallic wires may be used as a planar lens that focuses electromagnetic radiation.
- Establishment of a novel route to achieve broadband and ultra-subwavelength waveguiding in the perfectly conducting limit using strongly coupled wire grids.

In the next chapters we expand each of the above topics, and compare the new contributions with the open literature.

I.4. List of Author Publications

I.4.1. Articles in Journal

[J.1] **T. A. Morgado**, J. S. Marcos, M. G. Silveirinha, S. I. Maslovski, “Ultraconfined Interlaced Plasmons”, *Phys. Rev. Lett.*, vol. 107, no. 6, p. 063903 (4 pages), August 2011.

[J.2] S. I. Maslovski, **T. A. Morgado**, M. G. Silveirinha, C. S. R. Kaipa, A. B. Yakovlev, "Generalized additional boundary conditions for wire media", *New J. Phys.*, vol. 12, no. 11, p. 113047 (19 pages), November 2010.

[J.3] **T. A. Morgado**, J. S. Marcos, M. G. Silveirinha, S. I. Maslovski, “Experimental verification of full reconstruction of the near-field with a metamaterial lens”, *Appl. Phys. Lett.*, vol. 97, no. 14, p. 144102 (3 pages), October 2010.

[J.4] **T. A. Morgado**, M. G. Silveirinha, “Focusing of electromagnetic radiation by a flat slab of a crossed wire mesh metamaterial”, *Metamaterials*, vol. 4, no. 2-3, pp. 112-118, February 2010.

[J.5] **T. A. Morgado**, M. G. Silveirinha, “Transport of an arbitrary near-field component with an array of tilted wires”, *New J. Phys.*, vol. 11, no. 8, p. 083023 (21 pages), August 2009.

I.4.2. Articles in Conference Proceedings

[C.1] **T. A. Morgado**, J. S. Marcos, M. G. Silveirinha, S. I. Maslovski, "Trapping the light in a crossed wire mesh: broadband and ultra-subwavelength waveguiding", in *Proc. Metamorphose International Congress on Advanced Electromagnetic Materials in Microwaves and Optics – Metamaterials 2011*, Barcelona, Spain, October 2011.

[C.2] **T. A. Morgado**, M. G. Silveirinha, "Partial Focusing of Electromagnetic Radiation by a Planar Lens Formed by Crossed Metallic Wires", in *Proc. Metamorphose International Congress on Advanced Electromagnetic Materials in Microwaves and Optics – Metamaterials 2010*, Karlsruhe, Germany, September 2010.

[C.3] S. I. Maslovski, **T. A. Morgado,** M. G. Silveirinha, “The auxiliary source method and its application to the reflection problem at an interface with tilted wires”, in *Proc. International Symposium on Electromagnetic Theory*, Berlin, Germany, August 2010.

[C.4] **T. A. Morgado**, J. S. Marcos, S. I. Maslovski, M. G. Silveirinha, “Experimental Study of the Transport of an Arbitrary near-Field Component with an Array of Tilted Wires”, in *Proc. IEEE AP-S/URSI International Symposium on Antennas and Propagation*, Toronto, Canada, July 2010.

[C.5] **T. A. Morgado**, M. G. Silveirinha, "Transport of an Arbitrary Near-Field Component with an Array of Tilted Wires", in *Proc. Metamorphose International Congress on Advanced Electromagnetic Materials in Microwaves and Optics – Metamaterials 2009*, London, United Kingdom, September 2009.

[C.6] **T. A. Morgado**, M. G. Silveirinha, "Guided Modes in a Metamaterial Slab Formed by Crossed Metallic Wires", in *Proc. Conf. on Telecommunications- ConfTele*, Santa Maria da Feira, Portugal, May 2009.

References

[1] E. Yablonovitch, “Photonic band-gap crystals”, *J. Phys: Condens. Matter*, vol. 5, p. 2443, 1993.

[2] J. B. Pendry, “Photonic band structures”, *J. Mod. Opt.*, vol. 41, p. 209, 1994.

[3] J. D. Joannopoulos, R. D. Meade, J. N. Winn, *Photonic Crystals: Molding the Flow of Light*, Princeton, NJ: Princeton University Press, 1995.

[4] J. D. Joannopoulos, P. R. Villeneuve, S. Fan, “Photonic crystals: putting a new twist on light”, *Nature*, vol. 386, p. 143, 1997.

[5] E. Yablonovitch, “Inhibited Spontaneous Emission in Solid-State Physics and Electronics”, *Phys. Rev. Lett.*, vol. 58, p. 2059, 1987.

[6] A. Mekis, J. C. Chen, I. Kurland, S. Fan, P. R. Villeneuve, and J. D. Joannopoulos, “High Transmission through Sharp Bends in Photonic Crystal Waveguides”, *Phys. Rev. Lett.*, vol. 77, p. 3787, 1996.

[7] S. G. Johnson, S. Fan, P. R. Villeneuve, and J. Joannopoulos, L. A. Kolodziejski, “Guided modes in photonic crystal slabs”, *Phys. Rev. B*, vol. 60, p. 5751, 1999.

[8] M. Loncar, D. Nedeljković, T. Doll, J. Vučković, A. Scherer, and T. P. Pearsall, “Waveguiding in planar photonic crystals”, *Appl. Phys. Lett.*, vol. 77, p. 1937, 2000.

[9] M. Bayindir, B. Temelkuran, and E. Ozbay, “Propagation of photons by hopping: A waveguiding mechanism through localized coupled cavities in three-dimensional photonic crystals”, *Phys. Rev. B*, vol. 61, p. 11855, 2000.

[10] E. R. Brown, C. D: Parker, and E. Yablonovitch, “Radiation properties of a planar antenna on a photonic-crystal substrate”, *J. Opt. Soc. Am. B*, vol. 10, p. 404, 1993.

[11] B. Temerkuran, M. Bayindir, E. Ozbay, R. Biswas, M. M. Sigalas, G. Tuttle, and K. M. Hom “Photonic crystal-based resonant antenna with a very high directivity”, *J. Appl. Phys.*, vol. 87, p. 603, 2000.

[12] O. Painter, R. K. Lee, A. Scherer, A. Yariv, J. D. O'Brien, P. D. Dapkus, and I. I. Kim., "Two-Dimensional Photonic Band-Gap Defect Mode Laser", *Science*, vol. 284, p. 1819, 1999.

[13] S. Noda, A. Chutinan, and M. Imada, "Trapping and emission of photons by a single defect in a photonic bandgap structure", *Nature*, vol. 407, p. 608, 2000.

[14] S. Noda, M. Yokoyama, M. Imada, A. Chutinan, and M. Mochizuki, "Polarization Mode Control of Two-Dimensional Photonic Crystal Laser by Unit Cell Structure Design", *Science*, vol. 293. p. 1123, 2001.

[15] M. G. Silveirinha, "Metamaterial homogenization approach with application to the characterization of microstructured composites with negative parameters", *Phys. Rev. B*, vol. 75, p. 115104, 2007.

[16] C. R. Simovski and S. A. Tretyakov, "Local constitutive parameters of metamaterials from an effective medium perspective", *Phys. Rev. B*, vol. 75, p. 195111, 2007.

[17] D. R. Smith, W. J. Padilla, D. C. Vier, S. C. Nemat-Nasser, and S. Schultz, "Composite Medium with Simultaneously Negative Permeability and Permittivity", *Phys. Rev. Lett.*, vol. 84, p. 4184, 2000.

[18] R. A. Shelby, D. R. Smith, and S. Schultz, "Experimental Verification of Negative Index of Refraction", *Science*, vol. 292, p. 77, 2006.

[19] J. Valentine, S. Zhang, T. Zentgraf, E. Ulin-Avila, D. A. Genov, G. Bartal, X. Zhang, "Three-dimensional optical metamaterials with a negative refractive index", *Nature*, vol. 455, p. 376, 2008.

[20] J. T. Shen, P. B. Catrysse, S. Fan, "Mechanism for Designing Metallic Metamaterials with a High Index of Refraction", *Phys. Rev. Lett.*, vol. 94, p. 197401, 2005.

[21] J. Shin, J.-T. Shen, S. Fan, "Three-Dimensional Metamaterials with an Ultrahigh Effective Refractive Index over a Broad Bandwidth", *Phys. Rev. Lett.*, vol. 102, p. 093903, 2009.

[22] M. G. Silveirinha, C. A. Fernandes, "Nonresonant structured material with extreme effective parameters", *Phys. Rev. B*, vol. 78, p. 033108 , 2008.

[23] M. G. Silveirinha, C. A. Fernandes, J. R. Costa, C. R. Medeiros, "Experimental Demonstration of a Structured Material with Extreme Effective Parameters at Microwaves", *Appl. Phys. Lett.*, vol. 93, p. 174103, 2008.

[24] P. A. Belov, Y. Hao, and S. Sudhakaran, "Subwavelength microwave imaging using an array of parallel conducting wires as a lens", *Phys. Rev. B*, vol. 73, p. 033108, 2006.

[25] M. Silveirinha, N. Engheta, "Tunneling of Electromagnetic Energy through Subwavelength Channels and Bends using ε-Near-Zero Materials", *Phys. Rev. Lett.*, vol. 97, p. 15703, 2006.

[26] J. B. Pendry, "Negative Refraction Makes a Perfect Lens", *Phys. Rev. Lett.*, vol. 85, p. 3966, 2000.

[27] A. Grbic, and G. V. Eleftheriades, "Overcoming the diffraction limit with a planar left handed transmission line lens", *Phys. Rev. Lett.*, vol. 92, p. 117403, 2004.

[28] N. Engheta, "An Idea for Thin Subwavelength Cavity Resonators Using Materials with Negative Permittivity and Permeability", *IEEE Antennas Wireless Propag. Lett.*, vol. 1, p. 10, 2002.

[29] A. Alù, N. Engheta, "Mode Excitation by a Line Source in a Parallel-Plate Waveguide with a Pair of Parallel Double-Negative and Double Positive Slabs", *Proc. 2003 IEEE Antennas and Propag. Soc. Int. Symposium*, vol. 3, p. 359, 2003.

[30] A. Alù, N. Engheta, "Optical Nanotransmission Lines: Synthesis of Planar Left-Handed Materials in the Infrared and Visible Regimes", *J. Opt. Soc. Am. B*, vol. 23, p. 571, 2006.

[31] M. G. Silveirinha, P. A. Belov, and C. R. Simovski, "Subwavelength Imaging at Infrared Frequencies Using an Array of Metallic Nanorods", *Phys. Rev. B*, vol. 75, p. 035108, 2007.

[32] M. I. Stockman, "Nanofocusing of Optical Energy in Tapered Plasmonic Waveguides", *Phys. Rev. Lett.*, vol. 93, p. 137404, 2004.

[33] P. A. Belov, Y. Zhao, S. Tse, M. G. Silveirinha, C. R. Simovski, S. Tretyakov, Y. Hao, and C. Parini, "Transmission of images with subwavelength resolution to distances of several wavelengths in the microwave range", *Phys. Rev. B*, vol. 77, p. 193108, 2008.

[34] P. Ikonen, C. Simovski, S. Tretyakov, P. Belov, and Y. Hao, "Magnification of subwavelength field distributions at microwave frequencies using a wire medium slab operating in the canalization regime", *Appl. Phys. Lett.*, vol. 91, p. 104102, 2007.

[35] G. Shvets, S. Trendafilov, J. B. Pendry, A. Sarychev, “Guiding, Focusing, and Sensing on the Subwavelength Scale using Metallic Wire Arrays”, *Phys. Rev. Lett.*, vol. 99. p. 053903, 2007.

[36] M. G. Silveirinha, “Artificial plasma formed by connected metallic wires at infrared frequencies”, *Phys. Rev. B*, vol. 79, p. 035118, 2009.

[37] M. G. Silveirinha, C. A. Fernandes, and J. R. Costa, “Superlens made of a metamaterial with extreme effective parameters”, *Phys. Rev. B*, vol. 78, p. 195121, 2008.

[38] M. G. Silveirinha, C. R. Medeiros, C. A. Fernandes, and J. R. Costa, “Experimental verification of broadband superlensing using a metamaterial with an extreme index of refraction”, *Phys. Rev. B*, vol. 81, p. 033101, 2010.

[39] Y. Liu, G. Bartal, X. Zhang, “All-angle negative refraction and imaging in a bulk medium made of metallic nanowires in the visible region”, *Opt. Express*, vol. 16, p. 15439, 2008.

[40] J. Yao, Z. Liu, Y. Liu, Y. Wang, C. Sun, G. Bartal, A. M. Stacy, X. Zhang, “Optical Negative Refraction in Bulk Metamaterials of Nanowires”, *Science*, vol. 321, p. 930, 2008.

II. MANIPULATING THE NEAR-FIELD WITH A TILTED WIRE MEDIUM LENS

II.1. Introduction

It is well known, since the works of Lord Rayleigh [1] and Ernst Abbe [2] that the resolution of common imaging devices is restricted by the wavelength of light (diffraction limit). According to their studies, features smaller than approximately half-wavelength of the light are invariably absent from the image created by conventional optical lenses. But why does this resolution restriction occurs? As discussed next, the answer is enclosed in the near-field spectrum of the object source.

The near-field can be seen as the slight extension of the electromagnetic fields existing inside a certain material beyond its physical boundary. Its existence results from the necessary continuity of the field amplitudes and energy across the interface of the media. In contrast with the far-field that radiates freely from the source and hence can be captured by common lenses, the near-field has an inherent evanescent wave character, which causes the exponential decay of its amplitude in usual natural available materials, and thus the conventional optical systems are unable to interact with such high-frequency spatial harmonics fields. Since the subwavelength details of the object spatial structure are locked away in the near-field, the answer to realize imaging devices with super-resolution may be given by complex materials that could interact with these evanescent fields.

In this chapter, some of the most significant and promising subwavelength imaging approaches and technologies are introduced and explained. After this, we investigate the potentials of near-field transport of a metamaterial lens formed by tilted metallic wires. Finally, in the last part of the chapter we propose a simple and innovative approach to full reconstruct the near-field of an excitation source using the structured lens formed by tilted wires.

II.2. Subwavelength Imaging Mechanisms

II.2.1. Superlensing

In the beginning of last decade, J. B. Pendry introduced a theoretical possibility to surpass the diffraction limit that affects conventional imaging devices. It was theoretically demonstrated in the manuscript of Ref. [3] that a material slab with negative index of refraction ($n=-1$), specifically a double-negative material with $\varepsilon=\mu=-1$, makes a *perfect lens*, with unlimited resolution independent of the wavelength of light and of the polarization of the light. Such lens was designated in Ref. [3] as "superlens", and its operation is based on two distinct phenomena: the propagating modes (associated with the far-field) of a source are focused due to the negative refraction, whereas the evanescent modes (associated with the near-field) are restored due to resonant excitation of surface plasmons supported by the double-negative medium. The superlens proposed by Pendry is exactly the same structure studied by Veselago about thirty years before in his pioneering work [4], denominated there as pseudo-lens. Nevertheless, Veselago only perceived the existence of the negative refraction effect at the interfaces of the double negative lens. The possibility of enhance the near-field spectrum of the source taking advantage of the resonant excitation of surface waves was unnoticed to him. Here, we are specifically interested in the discussion of this possibility of restoring the near-field spectrum. The phenomenon of negative refraction that is directly related to far-field excitations will be discussed later in Chapter III.

Stimulated by such theoretical works and by the development of advanced fabrication technologies, approximately ten years ago researchers have fabricated the first artificially structured material (metamaterial) that exhibits negative isotropic index of refraction at microwave frequencies [5]. On the other hand, a truly negative isotropic index of refraction in the optical domain was only verified very recently [6], owing to the difficulty to create magnetic responses at such range of frequencies.

Despite all the promising imaging potentials of the superlens based on double-negative materials, it soon became evident that such imaging mechanism has some fundamental physical constraints in obtaining high resolutions that can be hardly surpassed. In addition to the numerous practical difficulties related to the realization of materials with negative isotropic index of refraction, the strong sensitivity to losses and material dispersion are also key limitations [7-8].

An alternative solution to the Pendry's *perfect lens* was introduced by Maslovski *et al.* in Ref. [9]. In their work it was shown that a system of two phase conjugation planes or sheets placed in free-space has the same behavior of the Pendry's superlens, providing the negative refraction effect and also the enhancement of the evanescent waves. The drawback of this system is the necessity to involve nonlinear materials or devices, making it only feasible for single-frequency (steady-state) operations. Such idea was also later discussed by Pendry in its publication of Ref. [10] using the equivalent designation of time reversal instead of phase conjugation as in Ref. [9].

In situations where only the restoration of the near-field spectrum of the source is required, without focusing of the propagating waves, there are interesting alternatives to

Pendry's lens. In fact, such possibility was also pointed out by Pendry in Ref. [3]. He stated that "*in a system in which all the dimensions are smaller than the wavelength of light... we can neglect radiative effects decoupling electrostatic and magnetostatic fields*", which means that in the near-field domain the electric and magnetic responses are nearly decoupled. As a consequence, only one of the material parameters (ε or μ) need to be negative to support resonant guided modes for one specific polarization. Hence, it is sufficient to use materials with negative permittivity to restore the evanescent spectrum of TM-polarized waves (or p-polarized waves; magnetic field parallel to the interface), and analogously materials with negative permeability to enhance the near-field of TE-polarized waves (or s-polarized waves; electric field parallel to the interface). In Ref. [3] it was suggested that a simple way to may restore the near-field of TM-polarized waves at optical frequencies is using a slab made of a noble metal (e.g. silver, gold, and copper). The underlying idea is that at such range of frequencies the permittivity of metals is predominantly real and negative, which may contrast with the real and positive permittivity of the surrounding space (e.g. free space). As a consequence, there are plasmonic excitations (surface plasmons) at both metal-dielectric interfaces which may enable the enhancement of the evanescent waves. Following such findings, in Ref. [11] it was experimentally demonstrated the restoration of the near-field using a silver superlens. Similarly, it has been shown that artificial material slabs with an effective negative permeability may also be used as near-field imaging systems for TE-polarized waves owing to the excitation of magnetoinductive surface waves [12-13].

In Ref. [14] new ways to restore the evanescent spectrum and thus achieve subwavelength near-field imaging were also introduced. It was shown that a system of two coupled planar material sheets possessing surface mode resonances can be used to enhance the evanescent waves. This alternative system was proved to be realizable at microwave frequencies by grids or arrays of resonant particles.

In a recent manuscript [15] Silveirinha *et al.* also proposed a new mechanism of near-field superlensing based on a material formed by an ultra-dense array of nonconnected crossed metallic wires. It was shown by the same authors in a preceding publication [16] that such structured material may behave as a material with extremely large positive index of refraction that supports the propagation of ultra-subwavelength guided modes. Following such results, in Ref. [15] it is theoretically proven the possible excitation of these deeply subwavelength guided modes by the evanescent spectrum of a source, enabling in this way the enhancement of evanescent waves and thus the restoration of the near-field. Such near-field imaging mechanism was then experimentally verified at microwave frequencies in Ref. [17].

II.2.2. Subwavelength Imaging with Photonic Crystals

The promising electromagnetic properties achievable with double-negative metamaterials are difficult to realize in practice, as already discussed above. Hence, alternative configurations based on photonic crystals have been also intensively investigated [18-25]. In contrast to Pendry’s lens, in photonic crystals negative refraction may be achieved without relying on a negative index of refraction of the material. Negative refraction is obtained due to a specific form of isofrequency contours, whereas the enhancement of the evanescent spectrum arises due to the excitation of resonant surface plasmons. Refs. [20-21] introduced configurations that exploit the effect of negative refraction and the enhancement of the near-field spectrum close to the band-gap edges of photonic crystals, thus allowing subwavelength imaging.

Nevertheless, similar to the superlens based on double-negative media also the photonic crystal–based superlens presents some practical drawbacks. At first, its resolution depends on the lattice period of the structure and also of the dielectric permittivity of the host medium. Hence, an easy way to increase the resolution could be achieved by simultaneously increasing the host permittivity, and by decreasing the lattice period [20]. However, in the optical domain large permittivity of real media is associated with high losses, which hinder really subwavelength resolutions (less than $\lambda / 4$). On the other hand, in order to achieve negative refraction in photonic crystals, the structure has to be operated close to the band-gap boundary. Hence, there is a limited range of frequencies (or wavelengths) where the photonic crystal can be operated and consequently the crystal-lattice spacing is also restricted ($a \approx \lambda$). Moreover, there still is another factor that deteriorates the imaging properties of superlenses based on photonic crystals, which is related with the multiple reflections suffered at the interfaces and that disturb the image quality. Such problem is a consequence of the finite thickness of the lens and of the mismatch between the wave impedances of air and photonic crystal.

II.2.3. Canalization Regime

Some research groups, during their studies of the imaging properties of photonic crystals noticed that, in certain circumstances, the physical mechanism behind the image transmission was not the negative refraction effect [26-30]. They found that the imaging mechanism was neither based on negative refraction nor on the enhancement of evanescent waves [26-30]. Specifically, such regime relies on the transformation of the whole source-radiation spatial spectrum (including evanescent free-space harmonics) into propagating crystal eigenmodes at the first interface of the crystal. All these eigenmodes travel in a fixed direction with speed of light, carrying the near-field distribution with super-resolution and delivering it at the back interface. Such regime was designated by canalization in Ref. [30], and becomes possible if the crystal has a flat isofrequency contour and its thickness is equal to an integer number of half-wavelengths (Fabry-Perot resonance). The first requisite allows that all the spatial harmonics created by a source (including evanescent waves) and refracted into the interface have the same longitudinal components of the wave vector and the same group velocity. On the other hand, the Fabry-Perot resonance condition allows eliminating the reflections at the interface of the crystal for any angle of incidence, including complex angles (i.e., evanescent waves), and hence there is total transmission of the incident radiation. It is important to stress that, in contrast to an ordinary lens, or even the Pendry's superlens, which form a focal spot of the electromagnetic radiation at the image plane, in the canalization regime the crystal operates as a waveguide delivering the near-field from the input interface to the output interface.

Based on such ideas, a few years ago it was suggested to use an array of parallel metallic wires to achieve such canalization regime at microwave frequencies [31]. In Refs. [31-33], it was demonstrated that such "wire medium lens" is able to manipulate and canalize a complex near-field distribution in the microwave band with super-resolution (at least five times superior to that obtained with conventional lenses). The image resolution of such structured lens depends solely of the lattice period of the structure [32], similar to what happens in photonic crystals, but in contrast here the structure does not have to necessarily operate in a specific frequency band where it exhibits negative refraction and thus the lattice period (i.e., the spatial resolution) can be made as small as required. As explained in

Refs. [31-32], the “wire medium lens” can be regarded as a set of uncoupled waveguides having subwavelength dimensions (each of the metallic wires) that guide the radiation pixel to pixel from the object plane to the image plane. In Ref. [34] it was demonstrated that this “wire medium lens” provide a unique opportunity to transport the subwavelength details of the source without significant distortion to nearly unlimited distances, with good tolerance to material losses and a fairly large bandwidth (around 15%). In addition, it was shown that arrays of wires in which the space between wires is gradually increased (or decreased) may be used to magnify (or demagnify) a near-field distribution [34-35]. Such “magnifying wire medium lens” may allow imaging near-field distributions into images with details larger than wavelength that can be captured in the far-field (e.g., by conventional lenses). On the other hand, the “demagnifying wire medium lens” allows creating complex near-field images from far-field distributions.

The implementation of the canalization regime in terahertz and infrared bands was also numerically demonstrated using a structure formed by silver nanorods embedded in a block of chalcogenide glass [36-37]. Image resolutions of the order of $\lambda/10$ and even larger were reported [36-37]. At higher frequencies including the visible range such “wire medium lens” does not operate so effectively since metals lose the electric conductive properties and begin to exhibit a plasmonic behavior. Nevertheless, it was demonstrated that a similar canalization regime can be obtained at the optical range using a layered metal-dielectric structure [38]. Structured materials consisting of alternating metal-dielectric layers but with cylindrical shape, have been explored as imaging devices that, similar to the “magnifying wire medium lens” at microwave and terahertz frequencies, allow bringing subwavelength images into the far-field at the optical band [39-42]. Such far-field subwavelength imaging devices are designated by hyperlenses.

II.2.4. Radiationless Electromagnetic Interference

A distinct subwavelength focusing approach from all already discussed was recently introduced by Merlin [43] and is designated by Radiationless Electromagnetic Interference (REI). It is based on patterned planar subwavelength structures that interact with an incoming plane wave to obtain a desired near-field distribution. Similar to the Fresnel's zone plates [43-44], the designed structure permits to control the near-field so that the evanescent waves exit the subwavelength plates in a pattern set by the structure design, which forces them to converge to a spot arbitrarily small on the focal plane.

II.3. Transport of an Arbitrary Near-Field Component with a Tilted Wire Medium Lens

Imaging devices relying on the canalization principle are particularly robust solutions, namely those based on arrays of parallel metallic wires [see Sec. II.2.3]. Such "wire medium lens" has several advantages in the manipulation of near-field distributions when compared to imaging devices based on the enhancement of the evanescent spectrum (superlenses). Since the operation of this structured lens does not rely on a resonant response of the material as in a superlens, the wire medium lens is dramatically less sensitive to losses. Moreover, in contrast to the superlens that, in practice, must have thickness less than half-wavelength in order that the evanescent waves can be enhanced, the thickness of the "wire medium lens" may be of several wavelengths. Hence, differently from the superlens, the "wire medium lens" allows imaging the subwavelength details at long distance [34].

In this section we study the potentials of near-field manipulation and transport of a modified configuration of the conventional setup formed by metallic wires normal to the interfaces [31]. The major motivation for this study is that despite all the qualities referred to above (Sec. II.2.3), the standard "wire medium lens" is polarization sensitive and only enables subwavelength imaging of *p*-polarized waves (magnetic field is parallel to the interface). To overcome this deficiency, we investigated if by tilting the wires along a suitable direction of space (so that the electric field has nontrivial projection onto the wires), the near field details can be captured, even when there is only electric field parallel to the interface (*s*-polarized waves).

II.3.1. Homogenization Model

The structure considered here consists of a periodic array of parallel metallic wires with finite length, as illustrated in Fig. 2.1. The wires are arranged in a square lattice with lattice period a and are embedded in a dielectric host with relative permittivity ε_h. The wires have radius r_w and are oriented along the direction $\hat{\mathbf{u}}_\alpha = \sin\alpha\hat{\mathbf{u}}_y + \cos\alpha\hat{\mathbf{u}}_z$ (forming an angle α with the z direction) (Fig. 2.1), where $\hat{\mathbf{u}}_y$ and $\hat{\mathbf{u}}_z$ are the unit vectors along the coordinate axes.

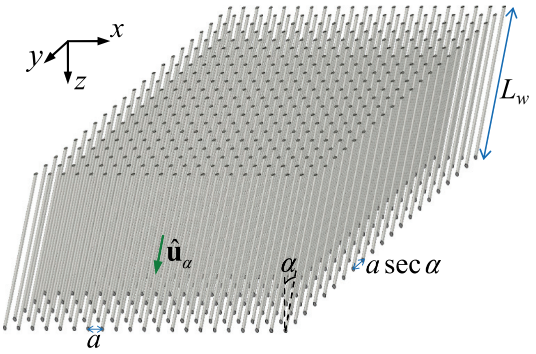

Fig. 2.1. Tilted square array of metallic wires. The metallic wires lie in planes parallel to *yoz* plane and are oriented along the direction $\hat{\mathbf{u}}_\alpha = \sin\alpha\hat{\mathbf{u}}_y + \cos\alpha\hat{\mathbf{u}}_z$.

The tilted wire medium of Fig. 2.1 is characterized by the following dielectric function [45-46]:

$$\overline{\overline{\varepsilon}}_{eff}=\varepsilon_h\left(\hat{\mathbf{u}}_x\hat{\mathbf{u}}_x+\hat{\mathbf{u}}_p\hat{\mathbf{u}}_p+\varepsilon_{eff,\alpha\alpha}\hat{\mathbf{u}}_\alpha\hat{\mathbf{u}}_\alpha\right),\quad \varepsilon_{eff,\alpha\alpha}\left(\omega,k_\alpha\right)=1-\frac{\beta_p^2}{\varepsilon_h\left(\omega/c\right)^2-k_\alpha^2},\tag{2.1}$$

where $\hat{\mathbf{u}}_p=\cos\alpha\hat{\mathbf{u}}_y-\sin\alpha\hat{\mathbf{u}}_z$ is the unit vector normal to the wires (see Fig. 2.2a), $k_\alpha=\mathbf{k}.\hat{\mathbf{u}}_\alpha$ is the projection of the wave vector $\mathbf{k}=(k_x,k_y,k_z)$ onto the direction of the wires, and β_p is the plasma wave number, which only depends on the lattice period a and on the radius of the wires r_w [45],

$$\beta_p^2=\left[2\pi/a^2\right]\Big/\left[\ln\left(\frac{a}{2\pi r_w}\right)+0.5275\right].\tag{2.2}$$

It has been known for some time that the wire media are characterized by a strongly spatially dispersive response [45]. This property is a consequence of the fact that the metallic wires are spanned over several unit cells. As a result, the polarizability acquired by the metallic inclusions in a given unit cell does not depend uniquely on the behavior of the macroscopic fields in the considered cell but also on the macroscopic fields at distances larger than the characteristic dimension of the unit cell, thus implying a nonlocal response of the medium. In fact, this property can be inferred from the dielectric function that describes the medium (Eq. (2.1)), since it depends not only on the frequency but also on the wave vector. One of the consequences of the nonlocal response of a material is the emergence of additional waves, i.e., for a fixed frequency and direction of propagation, the number of planes waves that propagates inside a spatially dispersive material may exceed the two independent plane waves (each one associated with a different polarization) supported by conventional local materials. Specifically, in this particular case the wire medium supports the propagation of three different electromagnetic plane wave modes (transverse electromagnetic (TEM) mode, transverse electric (TE) mode, and transverse magnetic (TM) mode) [45], in contrast with the usual uniaxial crystals which only support two different plane waves (ordinary and extraordinary waves) [47-48]. The emergence of the additional wave (TM mode) is a consequence of the discussed strong spatially dispersive response (or nonlocal response) that characterizes the wire medium even at low frequencies [45]. The dispersion characteristic for the electromagnetic modes can be obtained in the same manner as in Refs. [49-50], and the electric field polarization can be found in [J.5].

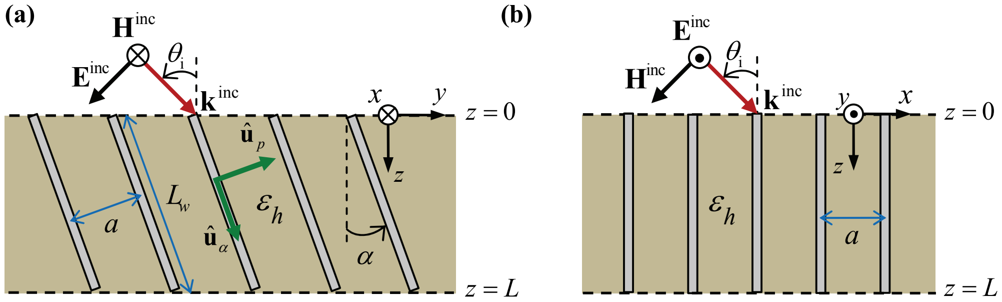

Fig. 2.2. Two different cuts of the tilted wire medium slab (Fig. 2.1). (a) Configuration I: plane of incidence is the *yoz* plane and the incident wave is TM-*z* polarized $[\mathbf{k}^{\text{inc}}=(0,k_y,k_z^{\text{inc}}),\ \mathbf{H}^{\text{inc}}=H\hat{\mathbf{u}}_x]$. (b) Configuration II: plane of incidence is the *xoz* plane and the incident wave is TE-*z* polarized $[\mathbf{k}^{\text{inc}}=(k_x,0,k_z^{\text{inc}}),\ \mathbf{E}^{\text{inc}}=E\hat{\mathbf{u}}_y]$.

Next, we concentrate our study on the analysis of the plane wave scattering problem for two different configurations (Fig. 2.2a-b). In the first configuration, it is assumed that the incident plane wave has wave vector $\mathbf{k}^{\text{inc}}=(0,k_y,k_z^{\text{inc}})$ and that the magnetic field is parallel to the interface (TM-*z* polarization) (Fig. 2.2a). On the other hand, in the second configuration the incoming wave propagates in the *xoz* plane with wave vector $\mathbf{k}^{\text{inc}}=(k_x,0,k_z^{\text{inc}})$, and the incident electric field is parallel to the interface (TE-*z* polarization) (Fig. 2.2b).

The electromagnetic fields in all space for both configurations (Fig. 2.2a-b) can be written as

$$
\begin{aligned}
&\mathbf{E}=\mathbf{E}^{\text{inc}}e^{-j\mathbf{k}^{\text{inc}}.\mathbf{r}}+\left(\rho_{\text{co}}\mathbf{E}_{\text{co}}^{\text{ref}}+\rho_{\text{cr}}\mathbf{E}_{\text{cr}}^{\text{ref}}\right)e^{-j\mathbf{k}^{\text{ref}}.\mathbf{r}}, \qquad z<0,\\
&\mathbf{E}=A_{\text{TE}}^{+}\mathbf{E}_{\text{TE}}^{+}e^{-j\mathbf{k}_{\text{TE}}^{+}.\mathbf{r}}+A_{\text{TE}}^{-}\mathbf{E}_{\text{TE}}^{-}e^{-j\mathbf{k}_{\text{TE}}^{-}.\mathbf{r}}+A_{\text{TM}}^{+}\mathbf{E}_{\text{TM}}^{+}e^{-j\mathbf{k}_{\text{TM}}^{+}.\mathbf{r}}+A_{\text{TM}}^{-}\mathbf{E}_{\text{TM}}^{-}e^{-j\mathbf{k}_{\text{TM}}^{-}.\mathbf{r}}+\\
&\qquad\qquad A_{\text{TEM}}^{+}\mathbf{E}_{\text{TEM}}^{+}e^{-j\mathbf{k}_{\text{TEM}}^{+}.\mathbf{r}}+A_{\text{TEM}}^{-}\mathbf{E}_{\text{TEM}}^{-}e^{-j\mathbf{k}_{\text{TEM}}^{-}.\mathbf{r}}, \qquad 0<z<L,\\
&\mathbf{E}=\left(t_{\text{co}}\mathbf{E}_{\text{co}}^{\text{tr}}+t_{\text{cr}}\mathbf{E}_{\text{cr}}^{\text{tr}}\right)e^{-j\mathbf{k}^{\text{tr}}.\mathbf{r}}, \qquad z>L,
\end{aligned}
\tag{2.3}
$$

where $(\rho_{\text{co}}, t_{\text{co}})$ are the reflection and transmission coefficients for the co-polarized wave, respectively, whereas $(\rho_{\text{cr}}, t_{\text{cr}})$ are the reflection and transmission coefficients for the cross-polarized wave, respectively. $\mathbf{E}^{\text{inc}}$, $\mathbf{E}_{\text{co}}^{\text{ref}}$, $\mathbf{E}_{\text{cr}}^{\text{ref}}$, $\mathbf{E}_{\text{co}}^{\text{tr}}$, and $\mathbf{E}_{\text{cr}}^{\text{tr}}$ are the incident, reflected co-polarized, reflected cross-polarized, transmitted co-polarized, and transmitted cross-polarized electric fields, respectively. $A_{\text{TE,TM,TEM}}^{\pm}$ are the unknowns amplitudes of the excited modes in the titled wire medium, $\mathbf{k}_{\text{TE,TM,TEM}}^{\pm}$ are the wave vectors of the excited modes [49-50], and $\mathbf{E}_{\text{TE,TM,TEM}}^{\pm}$ are the electric fields inside the metamaterial and are defined consistently with Eqs. (3)-(5) of [J.5]. The reflected co-polarized and cross-polarized electric fields are defined by Eqs. (8a-b) of [J.5]. The transmitted co-polarized and cross-polarized electric fields are given by analogous equations. The magnetic field either in the air regions or in the wire medium region can be easily obtained using the classical Maxwell-Faraday equation. For more details about the spatially dispersive homogenization model the reader is referred to the journal publication [J.5] and to Ref. [50].

As a consequence of the strong spatial dispersion effects that characterize the structured medium under study (Fig. 2.1) and which causes the emergence of an additional propagating plane wave, the classical boundary conditions which impose that the tangential components of the electric and magnetic fields are continuous at the interfaces are insufficient to solve the plane wave scattering problem. An additional boundary condition

(ABC) is required at the interfaces between the effective wire medium and air ($z = 0$ and L). In Refs. [49, 50], it was proven that the normal component of the electric field multiplied by the host permittivity ε_h must be continuous at both interfaces, i.e.

$$\mathbf{E}.\hat{\mathbf{u}}_z\big|_{\text{air side}} = \varepsilon_h \mathbf{E}.\hat{\mathbf{u}}_z\big|_{\text{wire medium side}}. \tag{2.4}$$

This ABC is equivalent to impose that the microscopic electric current that flows along each wire vanishes at both interfaces ($\mathbf{J}_{\text{d,av}}.\hat{\mathbf{u}}_\alpha = 0$ at $z = 0^+$ and $z = L^-$) [50]. Using this ABC and the classical boundary conditions, we obtain a 10×10 linear system which can be easily solved numerically with respect to the unknowns.

When the metallic wires are densely packed (limit $a / L_w \to 0$ with r_w / a fixed, being a the lattice constant and L_w the length of the wires), it is a good approximation to describe the wire medium as a material with extreme anisotropy being the optical axis parallel to the wires, i.e., with dielectric function of the form

$$\overline{\overline{\varepsilon}}_{eff} = \varepsilon_h \left(\hat{\mathbf{u}}_x \hat{\mathbf{u}}_x + \hat{\mathbf{u}}_p \hat{\mathbf{u}}_p + \infty \hat{\mathbf{u}}_\alpha \hat{\mathbf{u}}_\alpha \right). \tag{2.5}$$

In such circumstances, the effect of the additional wave (TM mode) can be ignored since its attenuation constant is very large, and thus the wave propagation in the wire medium can be described solely in terms of the TE and of the TEM modes. Hence, the electromagnetic response of the wire medium can be regarded as local (spatial dispersion effects are negligible when $a / L_w \to 0$), and thus the ABCs are not required.

II.3.2. Reflection and Transmission Characteristics

It was shown in previous works [31-34] that an array of metallic wires normal to the interface enables the transport of the subwavelength details associated with the component of electric field parallel to the wires. The subwavelength information associated with the remaining Cartesian components of the field is not imaged. Consequently, the setup introduced in [31] is polarization sensitive, being transparent to the *s*-polarized waves (electric field parallel to the interface). Our objective is to study if by tilting the wires it is still possible to capture and propagate the component of the electric field parallel to the wires. In particular, we want to show that by tilting the wires along a suitable direction of space (so that the electric field has a nontrivial projection onto the wires), it is possible to transport the subwavelength information associated with *s*-polarized waves.

In order to analyze the electromagnetic response of the tilted wire medium slab when illuminated by *p*-polarized waves (configuration I; see Fig. 2.2a) and also *s*-polarized waves (configuration II; see Fig. 2.2b), we define the effective reflection and transmission coefficients in the parallel direction to the wires ($\hat{\mathbf{u}}_\alpha$) as follows:

$$\rho_{\mathrm{eff}} = \left[\left(\rho_{\mathrm{co}}\mathbf{E}_{\mathrm{co}}^{\mathrm{ref}} + \rho_{\mathrm{cr}}\mathbf{E}_{\mathrm{cr}}^{\mathrm{ref}}\right).\hat{\mathbf{u}}_\alpha\right] \Big/ \left[\mathbf{E}^{\mathrm{inc}}.\hat{\mathbf{u}}_\alpha\right], \quad t_{\mathrm{eff}} = \left[\left(t_{\mathrm{co}}\mathbf{E}_{\mathrm{co}}^{\mathrm{tr}} + t_{\mathrm{cr}}\mathbf{E}_{\mathrm{cr}}^{\mathrm{tr}}\right).\hat{\mathbf{u}}_\alpha\right] \Big/ \left[\mathbf{E}^{\mathrm{inc}}.\hat{\mathbf{u}}_\alpha\right]. \quad (2.6)$$

Using Eqs. (2.6), next we study the dependence of the effective reflection and transmission coefficients on the transverse component of the wave vector for the two different configurations (Fig. 2.2), using the spatially dispersive homogenization model (Eq. (2.1)), the extreme anisotropy model (Eq. (2.5)), and full-wave simulations obtained with the electromagnetic simulator CST Microwave Studio 2008 [51].

II.3.2.1 Configuration I

To begin with, we consider the case where the tilted wire medium is illuminated by a plane wave that propagates in the *yoz* plane and is TM-*z* polarized (configuration I; see Fig. 2.2a). It is simple to verify that for such configuration the cross-polarized fields vanish and consequently the cross-polarized coefficients are zero ($\rho_{\rm cr} = t_{\rm cr} = 0$). Hence, Eqs. (2.6) reduce to

$$\rho_{\rm eff} = \left[\rho_{\rm co}\mathbf{E}^{\rm ref}_{\rm co}.\hat{\mathbf{u}}_\alpha\right]\Big/\left[\mathbf{E}^{\rm inc}.\hat{\mathbf{u}}_\alpha\right], \quad t_{\rm eff} = \left[t_{\rm co}\mathbf{E}^{\rm tr}_{\rm co}.\hat{\mathbf{u}}_\alpha\right]\Big/\left[\mathbf{E}^{\rm inc}.\hat{\mathbf{u}}_\alpha\right]. \tag{2.7}$$

The dependence of the effective reflection and transmission coefficients (absolute values) on the normalized transverse component of the wave vector k_y ($k_y = (\omega/c)\sin\theta_i$ for a propagating incoming wave, being θ_i the angle of incidence) are depicted in Fig. 2.3. The solid curves are associated with the spatially dispersive model (nonlocal model), the dashed curves with the extreme anisotropy model (local model), and the discrete symbols represent the full-wave results calculated with [51]. Clearly, the agreement between the three different approaches is very satisfactory.

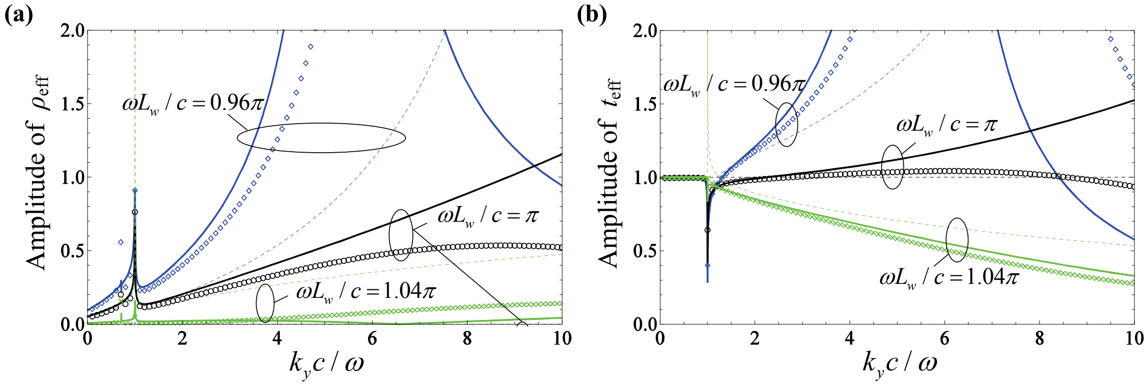

Fig. 2.3. Amplitude of the effective reflection (a) and transmission (b) coefficients as a function of the normalized transverse component of the wave vector k_y for configuration I (Fig. 2.2a), for a fixed normalized frequency $\omega a / c = 0.1$ and different wire lengths L_w. The permittivity of the dielectric substrate is $\varepsilon_h = 1$, the radius of the wires is $r_w = 0.05a$, and the tilt angle is $\alpha = 45^\circ$. Solid lines: spatially dispersive model (or nonlocal model). Dashed lines: extreme anisotropy model (or local model). Discrete symbols: full-wave results obtained with the electromagnetic simulator [51]. Notice that the reflection coefficient calculated using the extreme anisotropy model is exactly zero at the Fabry-Perot resonance ($\omega L_w / c = \pi$), and thus the corresponding curve in panel (a) is coincident with the horizontal axis.

One can see from Fig. 2.3 that, similar to the case of a slab with wires normal to interface [31], when the Fabry-Perot condition is satisfied ($\omega L_w / c = \pi$), the absolute value of the transmission coefficient in the direction parallel to the wires (t_{eff}) is very close to unity (even for evanescent waves), whereas the absolute value of ρ_{eff} is relatively small for all spatial harmonics. Hence, the obtained dependence of the effective reflection and transmission coefficients confirms that the slab of tilted wires can indeed be operated in a canalization regime and is capable of transporting the electric field component parallel to the wires. When $k_y c / \omega = 1$ (grazing incidence), the effective transmission coefficient exhibits an abrupt decay, and conversely the effective reflection coefficient has a very steep growth, exactly as occurs in the standard “wire medium lens”. It is important to stress that the Fabry-Perot resonance is determined by the length of the wires L_w and not by the thickness of the slab ($L = L_w \cos\alpha$). The results associated with the extreme anisotropy model (dashed curves) correspond to the ideal situation, since for $\omega L_w / c = \pi$ the effective reflection coefficient vanishes and the transmission coefficient is unity for the entire spatial spectrum.

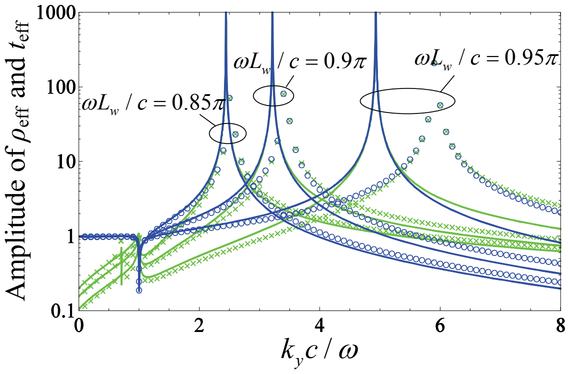

Fig. 2.4. Amplitude of the reflection (green) and transmission (blue) coefficients as a function of the normalized transverse component of the wave vector k_y for configuration I, for a fixed normalized frequency $\omega a / c = 0.1$ and different wire lengths L_w. The permittivity of the dielectric substrate is $\varepsilon_h = 1$, the radius of the wires is $r_w = 0.05a$, and the tilt angle is $\alpha = 45^{\circ}$. Solid lines: spatially dispersive model (or nonlocal model). Discrete symbols: full-wave results obtained with the electromagnetic simulator [51].

Naturally, the behavior of the effective reflection and transmission coefficient is sensitive to variations in the frequency of operation (or equivalently to variations in the electrical length of the wires). If the frequency is slightly lower than the frequency of operation (corresponding to the Fabry-Perot condition) then a resonant phenomenon is observed, as illustrated in Fig. 2.4. The effective reflection and transmission coefficients are greatly enhanced by the excitation of guided modes propagating along the *y* direction of the slab, consistent with the results of Ref. [32].

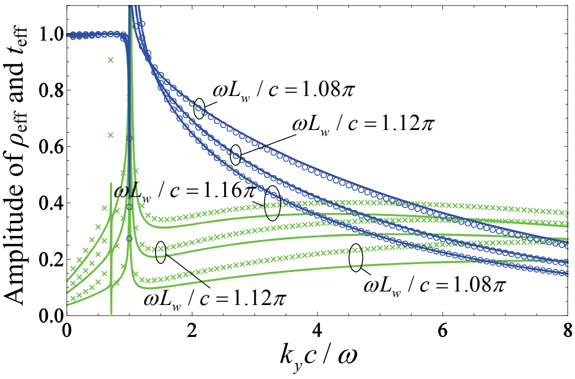

Fig. 2.5. The same as in Fig. 2.4 but for lengths of wires above Fabry-Perot condition.

On the other hand, for wire lengths slightly larger than half-wavelength (or equivalently for frequencies above the Fabry-Perot resonance), the effective reflection and transmission coefficients do not exhibit a resonant behavior. In contrast, and similar to the behavior of the usual wire medium slab [32], the transmission coefficient ($t_{\rm eff}$) for evanescent waves becomes weaker as the frequency increases (or the length of the wires), as shown in Fig. 2.5.

To conclude the analysis of the reflection and transmission properties of the slab of tilted wires for configuration I, it is important to discuss the peculiar resonant behavior exhibited by the effective reflection coefficient at $k_y c/\omega \approx 0.7$, more specifically when the direction of the incoming wave is parallel to the wires (see Fig. 2.3-Fig. 2.5). The reason for such strong variation in ρ_{eff} is only related to its definition (Eq. (2.7)). Indeed, when the incident field is normal to the wires (or equivalently the wave vector is parallel to the wires) both the numerator and the denominator of Eq. (2.7) vanish, since $\mathbf{E}^{\mathrm{inc}}.\hat{\mathbf{u}}_\alpha = 0$ and $\rho_{\mathrm{co}} = 0$ because the wave does not interact with the wires. This explains the abrupt variations in ρ_{eff} seen in Fig. 2.3-Fig. 2.5 around $k_y c / \omega \approx 0.7$. Nevertheless, even though ρ_{eff} may be reasonably large in those circumstances, in practice the reflections are negligible since the projection of the incident wave along the wires is nearly zero.

II.3.2.2 Configuration II

In this section, we study the reflection and transmission properties of the tilted wire medium for configuration II (Fig. 2.2b). Now the incoming wave propagates in the *xoz* plane and is TE-*z* polarized (*s*-polarization). It can be verified that in this configuration the cross components of the reflection and transmission coefficients (ρ_{cr} and t_{cr}, respectively) may be different from zero.

We calculate the effective reflection and transmission coefficients as a function of the normalized transverse component of the wave vector k_x ($k_x = (\omega / c)\sin\theta_i$) using again the nonlocal homogenization model, the extreme anisotropy model (Eq. (2.5)), and full-wave simulations [51]. As seen in Fig. 2.6, similar to the results of configuration I (Sec. II.3.2.1), also here the results for the effective reflection and transmission coefficients obtained using the three different methods concur relatively well.

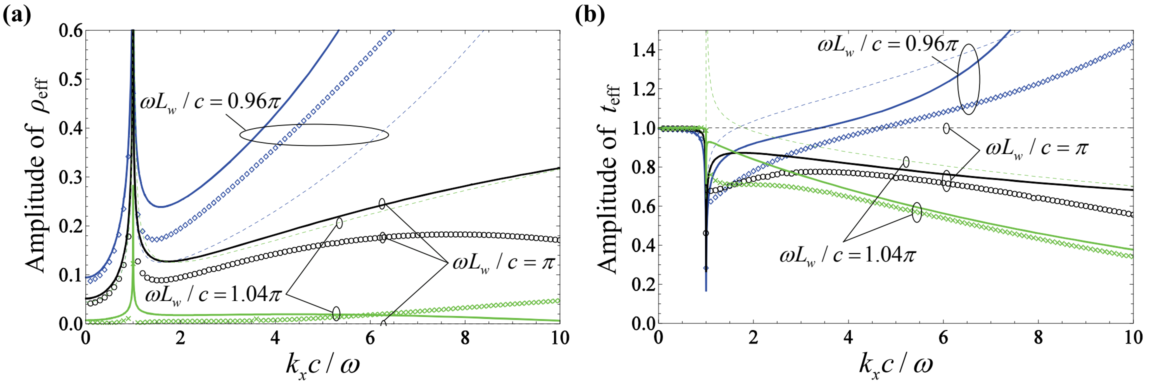

Fig. 2.6. Amplitude of the reflection (a) and transmission (b) coefficients as a function of the normalized transverse component of the wave vector k_x for configuration II (Fig. 2.2b), for a fixed normalized frequency $\omega a / c = 0.1$ and different wire lengths L_w. The permittivity of the dielectric substrate is $\varepsilon_h = 1$, the radius of the wires is $r_w = 0.05a$, and the tilt angle is $\alpha = 45^\circ$. Solid lines: spatially dispersive model (or nonlocal model). Dashed lines: extreme anisotropy model (or local model). Discrete symbols: full-wave results obtained with the electromagnetic simulator [51]. Notice that the reflection coefficient calculated using the extreme anisotropy model is exactly zero at the Fabry-Perot resonance ($\omega L_w / c = \pi$), and thus the corresponding curve in panel (a) is coincident with the horizontal axis.

In Fig. 2.6 it is seen that the behavior of the effective reflection and transmission coefficients for this configuration is similar to that of configuration I (see Fig. 2.3). In particular, when the Fabry-Perot condition is satisfied ($\omega L_w / c = \pi$), the amplitude of the transmission coefficient (for the electric field component parallel to the wires) is still close to unity for all spatial harmonics (including evanescent harmonics). Thus, these results confirm, indeed, that even though for this configuration there is only electric field parallel to interface (see Fig. 2.2b), it is still possible to operate the tilted wire medium in the canalization regime, and hence transport the component of the electric near-field parallel to the wires. As in configuration I, the extreme anisotropy condition corresponds to the ideal situation where at the Fabry-Perot resonance $|t_{\mathrm{eff}}| = 1$ and $|\rho_{\mathrm{eff}}| = 0$ for the entire spatial spectrum.

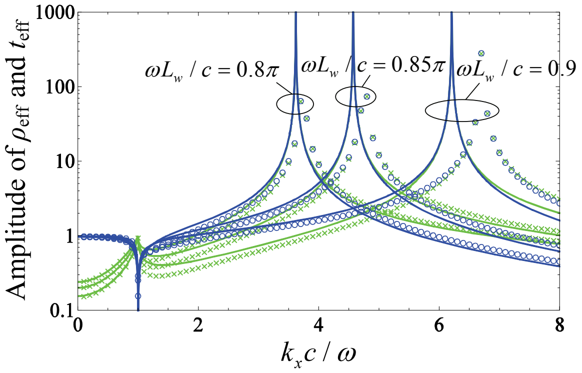

Fig. 2.7. Amplitude of the reflection (green) and transmission (blue) coefficients as a function of the normalized transverse component of the wave vector k_x for configuration II, for a fixed normalized frequency $\omega a / c = 0.1$ and different wire lengths L_w. The permittivity of the dielectric substrate is $\varepsilon_h = 1$, the radius of the wires is $r_w = 0.05a$, and the tilt angle is $\alpha = 45^\circ$. Solid lines: spatially dispersive model (or nonlocal model). Discrete symbols: full-wave results obtained with the electromagnetic simulator [51].

In the same manner as in configuration I, the response of the system change when the wires length (or the frequency) is altered. For wire lengths below half-wavelength ($\omega L_w / c < \pi$) it is clearly visible the sharp resonances in ρ_{eff} and t_{eff} (Fig. 2.7). This property reveals the presence of guided modes that propagate along the x direction and that cause an undesired strong enhancement of certain spatial harmonics.

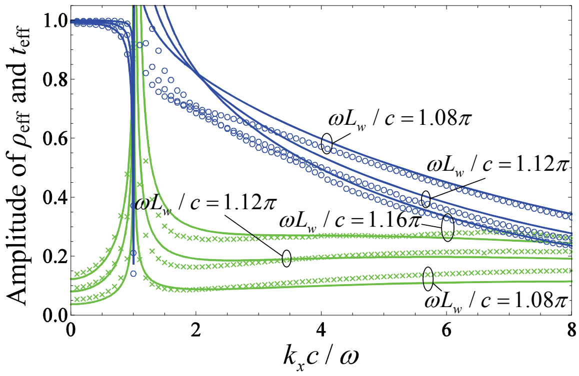

Fig. 2.8. The same as in Fig. 2.7 but for length of wires above the Fabry-Perot condition.

In contrast, for $\omega L_w / c > \pi$ the amplitude of the effective reflection coefficient tends to increase with frequency, whereas the amplitude of the effective transmission coefficient tends to decrease (Fig. 2.8), similarly to what occurs in configuration I as well as in the standard configuration of the “wire medium lens” [32].

II.3.3. Near-Field Transport

In order to verify the results of the previous section (Sec. II.3.2) and evaluate the potentials of near-field transport by the tilted wire medium lens, several numerical simulations of the structure were performed for both configurations. Such results are presented and discussed next.

II.3.3.1 Configuration I

In the first example, we consider a setup based on configuration I (Fig. 2.2a) and formed by an array of 20×20 metallic wires tilted by an angle of 45°. This structure was illuminated by a source which consists in a plane wave ($\mathbf{E}^{\mathrm{inc}} = E\,\hat{\mathbf{u}}_y$, $\mathbf{H}^{\mathrm{inc}} = H\,\hat{\mathbf{u}}_x$) incident onto a perfectly conducting screen with two extremely narrow (subwavelength) slits along the x direction (see Fig. 2.9). The wave diffracted by each slit mimics closely the field radiated by a magnetic line current directed along the direction of the slit [37], and thus the polarization of the wave that impinges on the wire medium slab is predominantly transverse magnetic (TM-z polarized; p-polarization). The length of the wires ($L_w = 15\,\mathrm{cm}$) is tuned so that the first Fabry-Perot resonance occurs at 1 GHz. We have used the electromagnetic simulator [51] to simulate the performance of this setup.

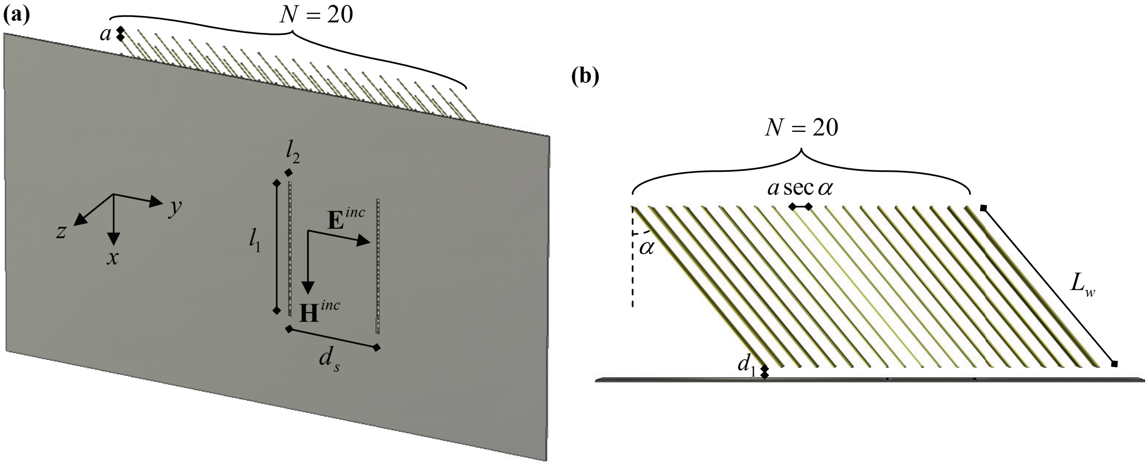

Fig. 2.9. Geometry of the finite-sized slab of tilted wires. The image is created by a metallic screen with two narrow slits that is illuminated by a plane wave. (a) Perspective view. (b) Top view. The wires stand in free space ($\varepsilon_h = 1$), their length is $L_w = 15\text{ cm}$ and they are tilted by an angle $\alpha = 45^\circ$. The period of the lattice is $a = 1\text{ cm}$, and the radius of the wires is $r_w = 0.5\text{ mm}$. The screen is at a distance of $d_1 = 8\text{ mm}$ from the front interface of the slab, and the slits have dimensions $l_1 = 10\text{ cm}$ and $l_2 = 2\text{ mm}$. The slits are separated by $d_s = 7{,}07\text{ cm}$.

In Fig. 2.10 the amplitude of the electric near-field component parallel to the wires ($\mathbf{E}.\hat{\mathbf{u}}_\alpha$) is depicted for frequencies in the interval 950 MHz – 1.05 GHz. It is clear from Fig. 2.10a that, notwithstanding the distance between the slits being very small ($d_s \approx 0.24\lambda_0$), at the Fabry-Perot resonance ($L_w = \lambda_0 / 2$) the two slits are perfectly resolved in the image plane. Therefore, consistently with the homogenization model, the tilted wire medium enables, indeed, the transfer of the subwavelength details of the object source from the front interface to the back interface through an oblique projection. It is important to refer that by properly scaling the structure it may be possible to obtain similar results at terahertz and infrared frequencies [37].

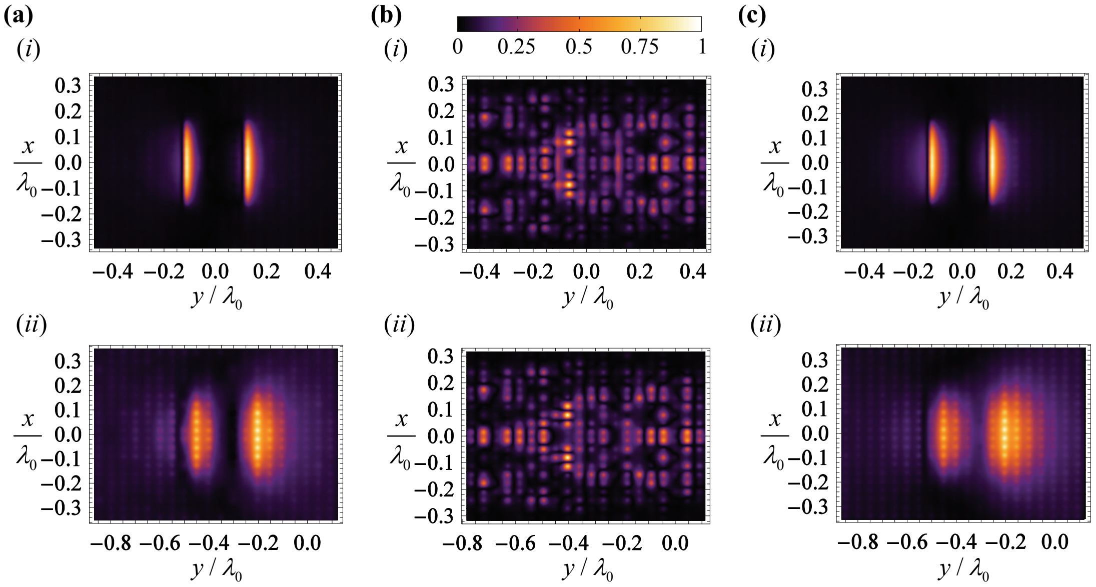

Fig. 2.10. Distribution of the normalized electric field along the direction of the wires (E_α) at the source plane (*i*) and at the image plane (*ii*), obtained from the simulation in [51] of the performance of the setup of Fig. 2.9 for different frequencies of operation. (a) $f = 1\,\text{GHz}$; (b) $f = 950\,\text{MHz}$; (c) $f = 1.05\,\text{GHz}$.

At frequencies lower than the design frequency (Fig. 2.10b), and consistent with the results of [32], the imaging properties are clearly deteriorated, and the two slits are hardly discernible, even at the source plane (Fig. 2.10b(*i*)). This happens due to strong reflections that occur for frequencies below the design frequency (which correspond to the Fabry-Perot resonance), mainly due to the excitation of guided modes (Fig. 2.4).

At higher frequencies, e.g. 1.05 GHz (Fig. 2.10c), the imaging properties are still very good and subwavelength imaging is still achieved. This could be expected from the results of Fig. 2.3 and Fig. 2.5. For frequencies higher than 1.05 GHz it is expected that the imaging properties will be progressively deteriorated due to the decrease of the amplitude of the transmission for high-frequency spatial harmonics (Fig. 2.5).

II.3.3.2 Configuration II

In this section, we consider a setup related to configuration II (Fig. 2.2b) with a source that radiates TE-*z* polarized waves (or *s*-polarized waves; electric field perpendicular to the plane of incidence). Specifically, we study the radiation problem where two electric line sources fed by currents in opposition of phase (and infinitely extended along *y* direction) are placed at a distance d_1 from the front interface (see Fig. 2.11a). The electric field radiated by the line sources is of the form $E_y = \left(E_0 / \left(4j\right)\right)\left(H_0^{(2)}\left(k_0\rho_1\right) - H_0^{(2)}\left(k_0\rho_2\right)\right)$, where E_0 is some constant that depends on the line current, ρ_1 and ρ_2 are the radial distances relative to the sources, and $H_0^{(2)}$ is the Hankel function of second kind and order zero. Using the method of moments (MoM), taking into account in this manner all the fine details of the microstructure of the artificial material, we have calculated the electric field profile along the direction of the wires, at the source and image planes. In the MoM simulation the artificial material slab was assumed periodic along the *y* direction, and finite along the *x* direction with width *W*.

In Fig. 2.11b the amplitude of the normalized electric field along the direction of the wires (E_α) is represented at the source and image planes for a metamaterial slab formed by tilted wires (the wires are tilted in the *yoz* plane) and with different lengths of the wires ($L_w \in \left[0.45\lambda_0, 0.54\lambda_0\right]$), whereas in Fig. 2.11c are depicted the density plots of $\left|E_\alpha\right|^2$ in the *xoz* plane for the same wire lengths. In all the simulations of Fig. 2.11b we only show the field profiles for one of the sources, since it is obvious that by symmetry $\left|E_\alpha\right|$ is an even function of x.

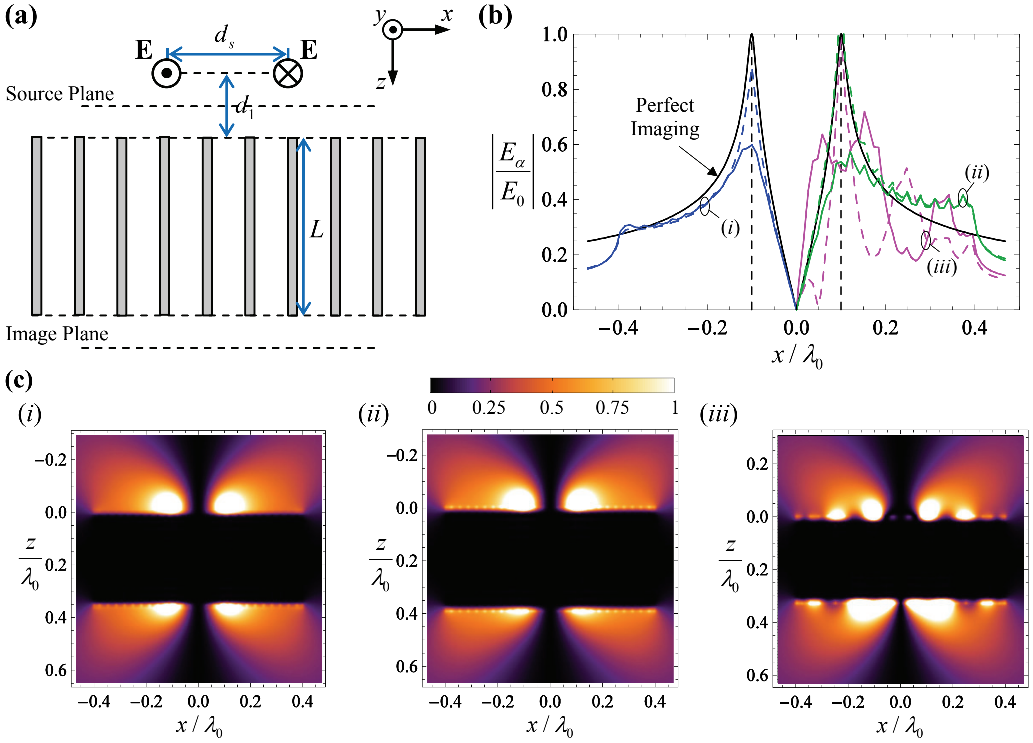

Fig. 2.11. (a) Geometry of the problem: two electric line sources are fed by currents in opposition of phase. The line sources are placed at a distance d_1 above the tilted wire medium slab and are separated by a distance d_s. The source and image planes are located at a distance $d_1/2$ from the front and back interfaces, respectively. The width of the structure in the x direction is W. (b) Amplitude of the normalized electric field component parallel to the wires at the image and source planes; (*i*) $L_w = \lambda_0/2$, $a = L_w/(10\pi)$, $r_w = 0.05a$, $\varepsilon_h = 1$, $\alpha = 45^\circ$, $d_1 = 0.016\lambda_0$, $d_s = 0.2\lambda_0$ and, $W \approx 0.8\lambda_0$ (50 rows of wires along the x direction); (*ii*) $L_w = 0.54\lambda_0$, $a = L_w/(10.8\pi)$, $r_w = 0.05a$, $\varepsilon_h = 1$, $\alpha = 45^\circ$, $d_1 = 0.016\lambda_0$, $d_s = 0.2\lambda_0$ and, $W \approx 0.8\lambda_0$ (50 rows of wires along the x direction); (*iii*) $L_w = 0.45\lambda_0$, $a = L_w/(9\pi)$, $r_w = 0.05a$, $\varepsilon_h = 1$, $\alpha = 45^\circ$, $d_1 = 0.016\lambda_0$, $d_s = 0.2\lambda_0$ and, $W \approx 0.8\lambda_0$ (50 rows of wires along the x direction). Solid black curve: perfect imaging (i.e. field profile at the source plane when the array of wires is removed); dashed curves: field profile at the source plane; solid colored curves: field profile at the image plane. The vertical black dashed lines represent the position of the sources. (c) $|E_\alpha|^2$ for an array of tilted wires with the same geometry as in (b): (*i*) same parameters as (b*i*), (*ii*) same parameters as (b*ii*), and (*iii*) same parameters as (b*iii*).

Fig. 2.11b(*i*) shows that, despite the distance between the sources being as small as $d_s = 0.2\lambda_0$, at the Fabry-Perot condition ($\omega L_w/c = \pi \Rightarrow L_w = \lambda_0/2$) the field profile at the image plane (solid curve) and at the source plane (dashed curve) are similar except in the close vicinity of the line sources, where the field has a steep variation. Such abrupt variations of the near-field are associated with very high-frequency spatial harmonics. It is expected that if the density of wires is increased the transported field will mimic more closely the field at the source plane [32, 37]. The same result can be seen in the density plot of Fig. 2.11c(*i*), where it is seen that the two sources are clearly resolved at the image plane. Hence, these full-wave results confirm the findings of Sec. II.3.2.2, and further demonstrate that a tilted wires lens can indeed transfer the subwavelength details of the source, restoring the component of the electric field parallel to the wires at the image plane, even when there is no electric field normal to the input interface. It is important to stress that the imaging of the considered object would be impossible using the usual configuration of the wire medium lens [31], since that in the present configuration the sources radiate TE-*z* polarized waves.

At the source plane, it is possible to observe a slight decrease of the amplitude of the electric field E_α in comparison to the situation in which the array of wires is removed (perfect imaging). This is completely consistent with the results of Sec. II.3.2.2 (Fig. 2.6), and is explained by the fact that the amplitude of the effective reflection coefficient (ρ_{eff}) is not negligible at the considered frequency ($\omega L_w / c = \pi \Rightarrow L_w = \lambda_0 / 2$), while its phase is equal to π for the evanescent spatial harmonics, which causes the incident and reflected fields to interact destructively.

When $L_w = 0.54\lambda_0$ (Fig. 2.11b-c(*ii*)) the sources become more difficult to distinguish at the image plane, consistent with the results of Fig. 2.8, which predict a decrease in the amplitude of the transmission coefficient. As discussed before, if the length of the wires is further increased it is expected that the imaging properties are progressively deteriorated and eventually the source may become indistinguishable. At the source plane, the amplitude of E_α is higher than at the Fabry-Perot resonance ($L_w = \lambda_0 / 2$). This is also completely consistent with the reflection characteristics of the system (see Fig. 2.6 and Fig. 2.8), given that the amplitude of ρ_{eff} for $L_w = 0.54\lambda_0$ is lower than for $L_w = \lambda_0 / 2$.

When $L_w = 0.45\lambda_0$ the imaging properties are very poor, and the sources are hardly perceptible even at the source plane (see Fig. 2.11b-c(*iii*)). Clearly, the field profile is completely corrupted by high-frequency noise. As discussed in Sec. II.3.2.2, the reason for this phenomenon is related to the excitation of the guided modes propagating along the *x* direction of the slab, which cause the enhancement of some spatial harmonics (see Fig. 2.11b-c(*iii*)).

II.4. Full Reconstruction of the Near-Field with a Tilted Wires Lens

Following the results of the previous section and the finding that the tilted wire medium lens (Fig. 2.1) enables improving the polarization sensitivity of the standard wire medium lens [31], here we introduce a strategy to fully restore the near-field radiated by an arbitrary source using the proposed metamaterial lens [52]. Indeed, since for a fixed orientation of the metallic wires it is possible to transport and restore the electric near-field component parallel to the wires (i.e. the component $E_\alpha = \mathbf{E}.\hat{\mathbf{u}}_\alpha$), then by rotating the tilted wire medium lens around the direction perpendicular to the interface plane (or around the *z*-axis; see Fig. 2.1) it is possible to change the orientation of the wires ($\hat{\mathbf{u}}_\alpha$), and consequently the projection of the electric field along a different direction of space can be captured. Specifically, if the array of tilted wires is sequentially rotated three times by 120° around the *z*-axis, it is possible to measure the projections of the electric field along three directions of space that are not coplanar. Since the three-dimensional space is completely determined by three linearly independent vectors, this makes possible to reconstruct all the near-field

Cartesian components of the electric field at the image plane by making only these three measurements. The magnetic field may be then easily computed from the electric field using the Stratton-Chu formulas [53], and in this manner fully restore the near-field electromagnetic spectrum.

As an alternative to the previous procedure, we can successively rotate the source by 120° around the direction normal to the lens interface, instead of rotating the tilted wires lens. Clearly, such approach is completely equivalent and also enables the capture of three linearly independent components of the electric field radiated by the source.

At this point, it should be underlined that the proposed approaches to retrieve all near-field Cartesian components of the electric field clearly require that the wires are tilted with respect to the interface, and cannot be implemented using the standard configuration of Ref. [31]. Moreover, such procedures obviously require that the image source is stationary with respect to time.

II.4.1. Experimental Setup and Post-Processing Approach

In order to verify the possibility of retrieving all the electric near-field components radiated by a source using the approach introduced above, we fabricated a prototype of the tilted wire medium lens (Fig. 2.12). The lens consists of an array of 21×21 copper wires scaled to operate at 1 GHz. Thus, the length of the wires is $L_w = 15$ cm so that it corresponds to half-wavelength in the free-space at the design frequency. The wires have radius $r_w = 0.5\,\text{mm}$ and are arranged in a square lattice with lattice period $a = 1\,\text{cm}$. The angle between the wires and the direction perpendicular to the interface planes is $\alpha = 45^{\circ}$, and the wires are supported by thin styrofoam slabs which have relative permittivity close to unity around the design frequency.

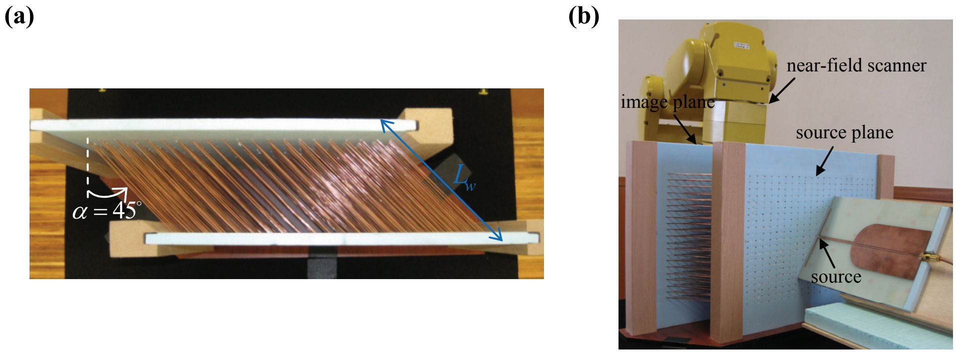

Fig. 2.12. Photos of the prototype of the tilted wire medium lens. (a) Top view of the metamaterial lens. (b) General view of the complete experimental setup. The fabricated prototype together with the printed dipole antenna (fed by a balun) and the near-field scanner based on a robotic arm.

A standard printed dipole antenna was taken as the near-field source. The printed antenna is fed by a coaxial cable through a balun and is placed at a distance $a/2$ from the front interface of the lens. A near-field scanner based on a robotic arm was used to measure the electric field distributions at the source and image planes ($a/2$ from the back interface of the lens).

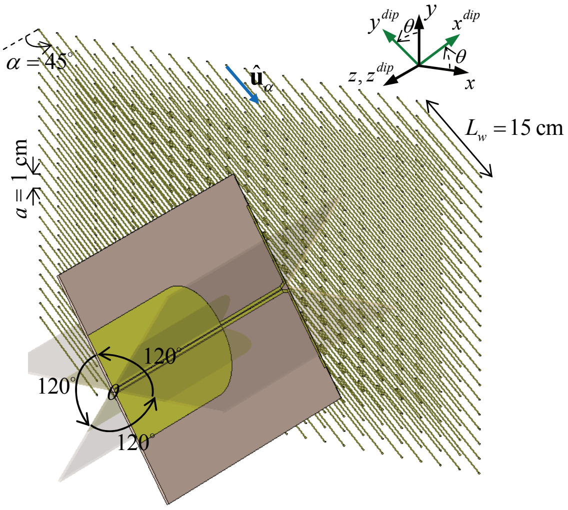

Fig. 2.13. Illustration of the principle used to restore the near-field: the dipole antenna is sequentially rotated by 120° around the z-axis and the E_z component of the electric field is measured for each configuration at the image plane.

Our experimental approach is based on the sequential rotation of the printed dipole by 120° around the *z* direction (direction normal to the lens interface) (Fig. 2.13) rather than on the equivalent rotation of the lens. We found more convenient to rotate the printed dipole because its rotation is in practice more easily performed than the rotation of the lens. For each dipole rotation, the wire medium lens captures the component of the electric field parallel to the wires (E_α) and transports it to the image plane with nearly no distortions of amplitude and phase, provided the length of the wires is a multiple of $\lambda_0 / 2$. In practice, it is possible to measure E_α simply by measuring the electric field component normal to the interface (E_z) at the image plane. This can be easily done using a tiny metallic probe (≈ 1 mm) perpendicular to the lens interface (i.e., directed along *z*). Indeed, even if the probe is not parallel to the wires its response is always proportional to E_α (calculated at the source plane), since as demonstrated above (Sec. II.3.2) E_α is the only component transported by the tilted wires lens.

Next, in order to explain the post-processing of the experimental data, it is convenient to introduce a set of coordinates (x, y, z) attached to the lens and a set of coordinates $(x^{\text{dip}}, y^{\text{dip}}, z)$ attached to the dipole antenna. The coordinates $(x^{\text{dip}}, y^{\text{dip}})$ are such that, whatever the orientation of the dipole in the *xoy* plane, x^{dip} runs always along the direction parallel to the dipole arms, whereas the y^{dip} direction is perpendicular to the dipole arms (see Fig. 2.13). The rotation of the dipole is done in such a way that the center of the dipole is kept fixed with respect to the lens interface, and has coordinates $(x, y, z) = (0, 0, 0)$. Thus, the center of the dipole is imaged into the point $(x, y, z) = (0, 0, -L_w \cos\alpha)$, independent of the orientation of the dipole. The result of each measurement at the output plane, for a specific orientation of the dipole antenna $(i=1,2,3)$, can be represented by a complex valued function $F_0^i(x,y)$. At the design frequency (Fabry-Perot resonance) $F_0^i(x,y)$ is proportional to E_α $(F_0^i(x,y)\propto E_\alpha)$ since, as already discussed, the metamaterial lens transports the component of the electric field parallel to the wires with negligible distortion. Then, using simple trigonometric relations for the two sets of coordinates, (x,y,z) and $(x^{\mathrm{dip}},y^{\mathrm{dip}},z)$, it follows that the electric field components in the reference frame of the dipole satisfy the following 3×3 linear system,

$$\begin{gathered}E_x'\sin\alpha\cos\theta^i+E_y'(-\sin\alpha\sin\theta^i)+E_z'\cos\alpha=\\ F_0^i\Big|_{(x^{\mathrm{dip}}\cos\theta^i-y^{\mathrm{dip}}\sin\theta^i,\,x^{\mathrm{dip}}\sin\theta^i+y^{\mathrm{dip}}\cos\theta^i)}\end{gathered},\tag{2.8}$$

where $\theta^i=0^\circ,120^\circ,240^\circ$ for $i=1,2,3$, respectively, and the prime indicates that the electric components are defined with respect to the dipole coordinate system. By solving this linear system with respect to $\left\{E_x',E_y',E_z'\right\}$, we can retrieve both the amplitude and phase of the electric near-field.

II.4.2. Experimental Results

Following the explanation of the experimental approach and of the data post-processing of the previous subsection, here we present the results of the experimental measurements.

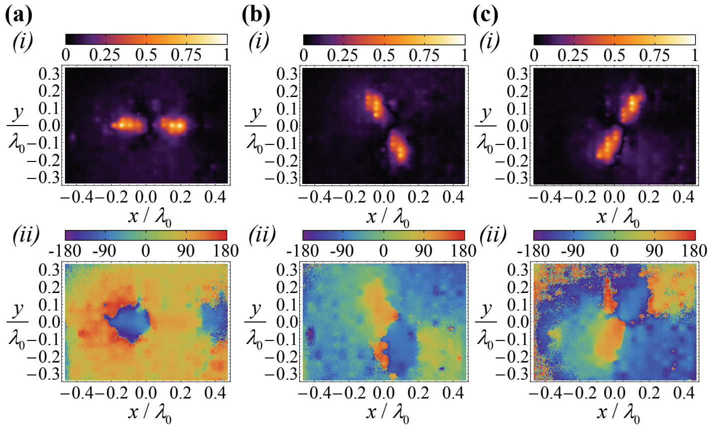

Fig. 2.14. Normalized amplitudes (*i*) and phases (in degrees) (*ii*) of the three near-field scan measurements for the design frequency of 1 GHz at the image plane. (a) The arms of the dipole are along the *x*-axis (parallel to the planes of the wires of the lens). (b) and (c): the dipole is rotated by 120° and 240° relatively to first position, respectively.

In Fig. 2.14 it is depicted the unprocessed data $F_0^i(x,y)$ (amplitude and phase) obtained from the measurements at the image plane for each angle of rotation of the dipole antenna and at the design frequency ($f=1$ GHz). The orientation of the dipole antenna in each measurement is clearly perceptible in the density plots of the amplitude as well as in the representations of the phase. In addition, the subwavelength imaging properties of the wire medium lens are quite evident from Fig. 2.14. The resolution is determined by the spacing between the wires and is roughly $a/\cos\alpha \approx 1.4a$ along the x direction, and a along the y direction.

The near-field of the dipole antenna is obtained from the unprocessed data (Fig. 2.14) by solving Eq. (2.8). Fig. 2.15 depicts the retrieved amplitude and phase of the *x*, *y*, and *z* components of the electric near-field (relative to the coordinate system attached to the dipole) for frequencies in the interval 975 MHz – 1.05 GHz.

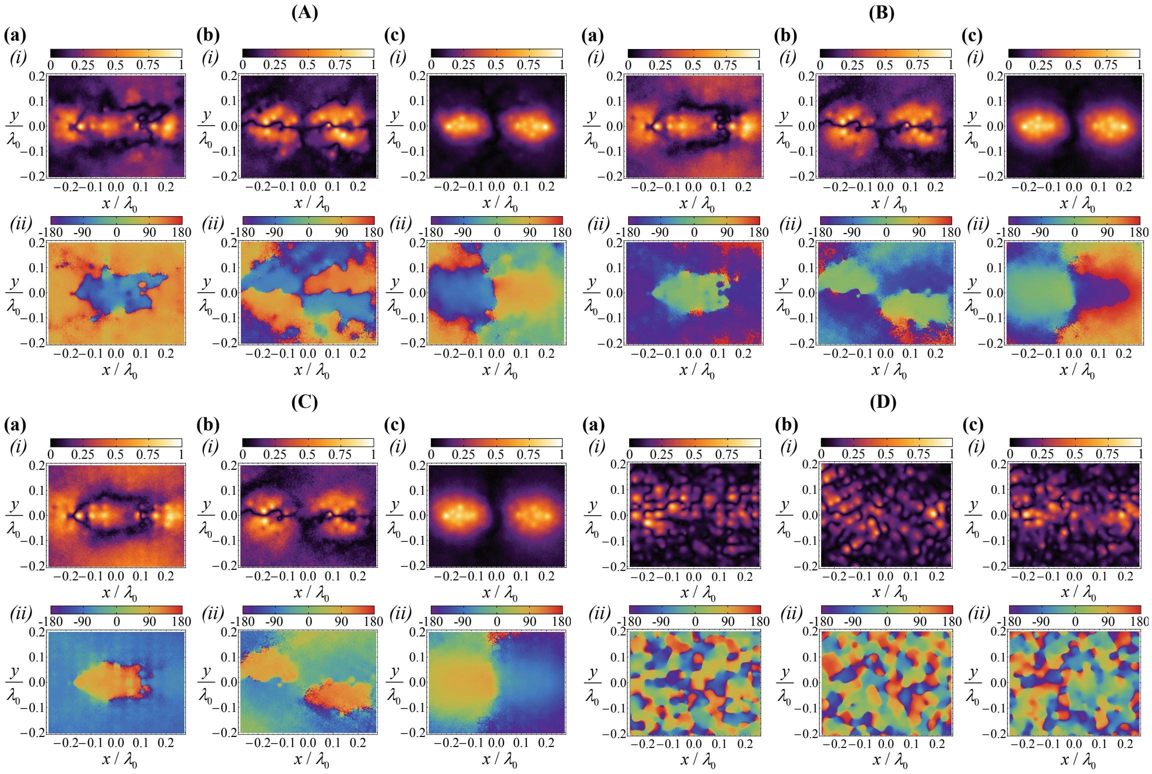

Fig. 2.15. Retrieved normalized amplitude (*i*) and phase (in degrees) (*ii)* of all components of the electric field of the dipole antenna. (A) $f = 1$ GHz; (B) $f = 1.025$ GHz; (C) $f = 1.05$ GHz; (D) $f = 975$ MHz. (a), (b) and (c) represent the *x*, *y*, and *z* components, respectively.

In order to have a benchmark for the post-processed results (Fig. 2.15), we depict in Fig. 2.16 the field distributions of the electric near-field of the printed dipole when it stands alone in free-space, calculated using the electromagnetic simulator [51].

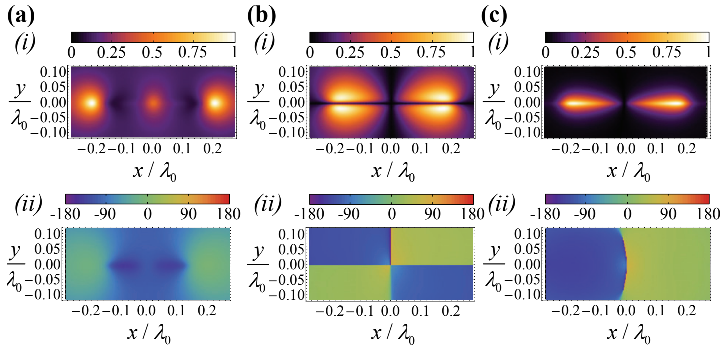

Fig. 2.16. Normalized amplitude (*i*) and phase (in degrees) (*ii*) of the near-field components of the electric field of the printed dipole antenna when it stands alone in free-space, obtained using CST Microwave Studio [51]. The frequency of operation is 1 GHz and the rest of the legend is as in Fig. 2.15.

It is clear from Fig. 2.15A, which corresponds to the Fabry-Perot resonance ($L_w = \lambda_0 / 2$), that the near-field distributions of all Cartesian components of the electric field and obtained from the post-processing approach introduced in Sec. II.4.1, reproduce accurately the theoretical field distributions (Fig. 2.16). In particular, consistent with Fig. 2.16a(*i*), Fig. 2.15Aa(*i*) shows three maxima for $|E_x|$ at both dipole arm ends and at the center of the dipole (i.e., at the feeding point). The phase of E_x also follows closely the theoretical results (Fig. 2.16a(*ii*)), varying approximately by 90° from the center to the arms ends. We note that in the unprocessed data (Fig. 2.14) the position corresponding to the center of the dipole ($(x, y) = (0, 0)$) corresponds invariably to a minimum, and thus it is quite remarkable that the extraction algorithm is, indeed, able to reconstruct the fine features of the near-field. In the same manner, it is seen from Fig. 2.15Ab that the reconstructed E_y is also completely consistent with the simulation results (Fig. 2.16b), being the four lobes and the null in the plane of symmetry $y = 0$ accurately predicted, as well as the behavior of the phase that alternates by 180° between the top and bottom lobes and the left and right lobes. As could be expected, E_z is the component more accurately restored, since besides being the electric field component normal to the lens interface it is the component radiated by the dipole antenna that has highest amplitude. The two lobes associated with the left and right arms of the dipole, as well as the 180° phase-shift, are clearly visible in Fig. 2.15Ac.

At higher frequencies, e.g., 1.025 GHz and 1.05 GHz (Fig. 2.15B-C), the three components of the electric near-field are still well retrieved. However, it is expected that for frequencies larger than 1.05 GHz the results become progressively less accurate, since as discussed in Secs. II.3.2-3 the wire medium lens introduces amplitude and phase distortions in the transmitted fields. As a consequence, we cannot assume anymore that E_α at the image and source planes are proportional, as we did in the derivation of Eq. (2.8). Nevertheless, in principle it is possible to include the effect of these distortions in the extraction algorithm, and in this manner we may improve even more the bandwidth of the proposed system.

At frequencies a few percent lower than 1 GHz (Fig. 2.15D), it is impossible to reconstruct the near-field because of the excitation of the guided modes that completely corrupt the transmitted image. This result is also completely coherent with the results of Secs. II.3.2-3.

An important point to underline is that the reconstructed fields may reproduce even more closely the theoretical results (Fig. 2.16) if the density of the wires is increased since, as already discussed in the previous sections, the resolution of the wires lens is only limited by the period of the structure. Moreover, by properly scaling the structure, and provided it is possible to measure both the amplitude and phase of the fields, it is in principle feasible to fully reconstruct the near-field up to terahertz frequencies [37]. Finally, it is important to emphasize again that such procedure is out of reach of the standard configuration with wires normal to the interface [31].

II.4.3. Application to Near-Field Measurements

The experimental results of the previous subsection confirm that the tilted wire medium lens can be used to access all the electric near-field Cartesian components of a certain object at a significant distance of its location, independent of the wave polarization.

Following these findings, here we speculate if such property can be advantageously exploited in near-field measurement.

A high-quality near-field measurement system must capture and measure the field details with subwavelength spatial resolution. This means that, in standard conditions, the measurement has to be performed in the near-field region, i.e., the scanning probe must be placed in the immediate vicinity of the source. However, such requirement of proximity of the probe to the object source may introduce significant and unpredictable perturbations to the near-field radiation and, consequently, the accuracy of the measurement may be completely corrupted.

In contrast, operating a tilted wire medium lens close to the Fabry-Perot resonance ($L_w = \lambda_0 / 2$) we are able to transport the near-field with nearly no distortions from the input interface to the output interface of the lens. As a result, the near-field can now be measured at a significant electrical distance from the object source, and in this way the disturbing effect caused by the near-field probe in the radiation of the source may be drastically reduced. Naturally, it is obvious that under such circumstances it is also important to take into account the perturbation perhaps induced by the metamaterial lens. However, such perturbation may be roughly negligible because the reflected field at the interface of a wire medium lens tuned to the Fabry-Perot resonance is relatively weak (see Sec. II.3.2-3).

As a final note, it should be pointed out that the minimization of the disturbing effects caused by the near-field probe may be particularly crucial if we use an extraction algorithm similar to the one reported in Sec. II.4.1 based on three different independent measurements of the near-field, since in order that Eq. (2.8) makes sense it is necessary that the field radiated by the antenna is independent of the measurement.

II.4.4. Experimental Validations

In order to confirm the theoretical considerations of the previous subsection we have measured the near-field of the same dipole antenna directly at the source plane (without the metamaterial lens) and using two different strategies. In the first configuration, similarly to the configuration with the tilted wires lens, the dipole antenna is successively rotated by 120° around the direction perpendicular to the interface (z direction). The scanning probe is tilted so that it makes an angle $\alpha = 45^\circ$ with the z direction and in this way we can, as before, theoretically measure three linearly independent components of the electric near-field. The reconstructed near-field obtained using this approach is depicted in Fig. 2.17.

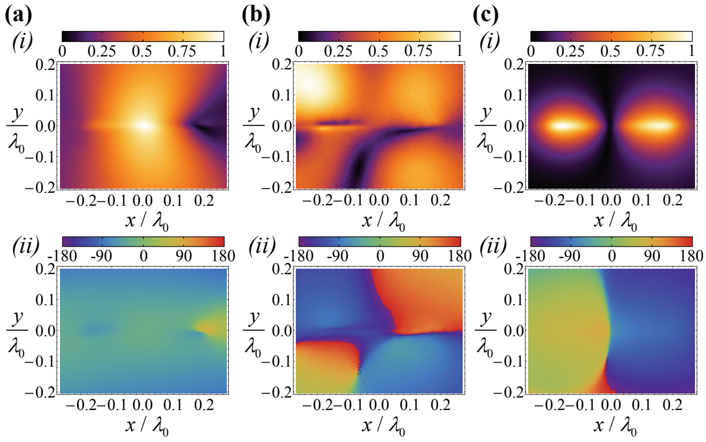

Fig. 2.17. Normalized amplitude (*i*) and phase (in degrees) (*ii*) of the electric near-field of the printed dipole antenna at the source plane and when the near-field scanning is performed directly at the source plane (without the lens). The frequency of operation is $f = 1\,\mathrm{GHz}$, and the rest of the legend is as in Fig. 2.15A.

Notwithstanding the fact that in this scenario the resolution of the images is only limited by the step of the near-field scanner (1 mm) and thus is nearly ten times higher than in the previous setup with the tilted wires lens, Fig. 2.17 undoubtedly shows a much coarser agreement with the theoretical results (Fig. 2.16) than the results obtained with tilted wires lens (Fig. 2.15A), particularly for the E_x and E_y field components. In order to verify that such result is indeed due to an increased perturbation of the antenna by the measurement system, we measured the S_{11} as a function of the position of the sensor in the two following scenarios: (i) near-field measurements in the presence of the lens; (ii) the same without the lens. The experimental results show that the standard deviation of the S_{11} in scenario (ii) is larger than in scenario (i) by a factor of 10%. Thus, our theoretical speculation that the tilted wires lens can minimize the disturbing effect introduced by the near-field probe in the measurements was experimentally validated.

In the second configuration, we obtained the near-field of the dipole antenna by directly measuring each Cartesian electric field component at the source plane, i.e., without using the approach based on the mechanical rotations of the source around the *z* direction. In order to measure the *x* and *y* components we had to bend the tip of the electric probe by 90°. In contrast, the *z* component is measured by simply placed the electric probe parallel to the *z* direction.

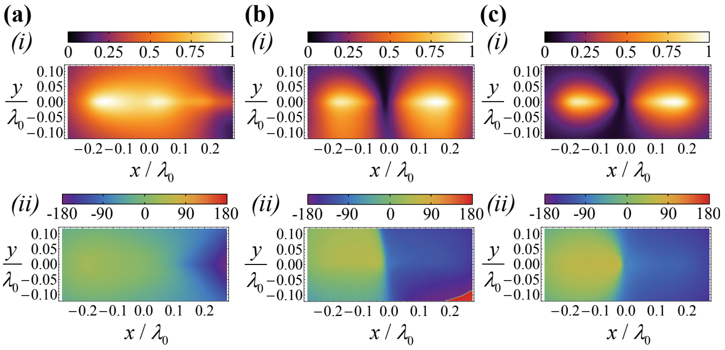

Fig. 2.18. Normalized amplitude (*i*) and phase (in degrees) (*ii*) of the electric near-field of the printed dipole antenna at the source plane when each of the Cartesian components of the electric field is directly measured (without using the experimental procedure introduced in Sec. II.4.1).

Similarly to Fig. 2.17, Fig. 2.18 reproduces much more inaccurately the theoretical electric near-field distributions (Fig. 2.16) than the results obtained with tilted wires lens (Fig. 2.15A). Particularly, the fine details of the *x* and *y* components, both the amplitude and phase, are completely lost from the image. It is possible that using a more sophisticated near-field probe the retrieved near-field would be more accurate. However, it is very interesting that when the near-field measurement is performed using the tilted wire medium lens, the retrieved near-field components are quite accurate, even though the same simplistic near-field probe is used.

Once again, the inaccuracy in the near-field reconstruction may be related to the perturbation introduced by the near-field probe in the measurement. In addition, there is another probable reason to the degradation of the near-field results when the scanning is directly performed at the source plane without using the metamaterial lens. In particular, when we bend the probe tip to measure the tangential components of the electric field (x and y components), an edge is formed, which unfortunately makes possible that the currents induced in the sensor may suffer a significant contribution of the normal component of the electric field (z component). This can be seen in the near-field results of E_y (Fig. 2.18b), which clearly show a great similarity with the near-field distribution of the z component (Fig. 2.18c). Instead of the four lobes and the null in the plane of symmetry $y = 0$, and the 180° phase-shift between the top and bottom lobes and the left and right lobes (see Fig. 2.16b), one can see only two lobes and a 180° phase-shift between the left and right lobes that are characteristic of the z component.

On the other hand, when using the tilted wires lens the component of the electric field required for the reconstruction process is effectively isolated by the lens before the actual measurement is done, and hence, the contribution of other electric field components to the currents induced in the near-field probe is completely prevented.

II.5. Summary

In this chapter, we have investigated the potentials of near-field transport of an array of tilted metallic wires. It was shown that, consistent with the standard wire medium configuration with wires normal to the interface [31-34], the considered setup also enables the transport of the subwavelength details associated with the electric field component parallel to the wires. The improvement achieved with this novel setup is that it allows restoring the electric near-field component parallel to the wires at the image plane, even when there is no electric field normal to the input interface, or in other words, it enables subwavelength imaging of not only TM-z polarized waves (or p-polarized waves) but also of TE-z polarized waves (or s-polarized waves). This is an important advance since the standard wire medium lens configuration [31-34] does not interact with s-polarized waves.

Based on these findings, we have suggested a simple approach to retrieve all the electric field Cartesian components of an arbitrary near-field source [52]. The underlying idea is to mechanically rotate the metamaterial lens (or equivalently rotate the near-field source) around the direction perpendicular to the interface so that three linearly independent components of the electric field can be measured. In order to experimentally verify such possibility, a prototype of the tilted wire medium lens scaled to operate at 1GHz was fabricated. Then, using a printed dipole antenna as the near-field source, we have experimentally demonstrated the total reconstruction of the electric near-field. In addition, it was experimentally verified that the retrieved near-field may be more accurate if obtained using the tilted wire medium lens than by direct measurement at the source plane. Such fact, as theoretically argued, besides being result of the reduction of the perturbation induced by the near-field probe when the measurement is done at a significant distance from the source using the metamaterial lens, it may be also a consequence of the ability of the lens of isolating the near-field component of interest.

In conclusion, the simplicity of the measurement system, the relative robust bandwidth of the lens, as well as the discussed minimal disturbing effect introduced in the measurement by the lens may open exciting avenues for the tilted wire medium lens in near-field measurement in a broad spectral range that includes microwaves and terahertz frequencies.

References

[1] Lord Rayleigh, *Philos. Mag.*, vol. 8, p. 261, 1879.

[2] E. Abbe, “Beiträge zur Theorie des Mikroskops und der mikroskopischen Wahrnehmung”, *Arch. Mikroskop. Anat.*, vol. 9, p. 413, 1873.

[3] J. B. Pendry, “Negative Refraction Makes a Perfect Lens”, *Phys. Rev. Lett.*, vol. 85, p. 3966, 2000.

[4] V. G. Veselago, “The Electrodynamics of Substances with Simultaneously Negative Values of ε and μ”, *Sov. Phys. Usp.*, vol. 10, p. 509, 1968.

[5] R. A. Shelby, D. R. Smith, S. Schultz, “Experimental Verification of a Negative Index of Refraction”, *Science*, vol. 292, p. 77, 2001.

[6] J. Valentine, S. Zhang, T. Zentgraf, E. Ulin-Avila, D. A. Genov, G. Bartal, X. Zhang, “Three-dimensional optical metamaterials with a negative refractive index”, *Nature*, vol. 455, p. 376, 2008.

[7] N. Garcia, M. Nieto-Vesperinas, “Left-Handed Materials Do Not Make a Perfect Lens”, *Phys. Rev. Lett.,* vol. 88, p. 207403, 2002.

[8] D. R. Smith, W. J. Padilla, D. C. Vier, S. C. Nemat-Nasser, S. Schultz, “Limitations on subdiffraction imaging with a negative refractive index slab”, *Appl. Phys. Lett.*, vol. 82, p. 1506, 2003.

[9] S. Maslovski, S. Tretyakov, “Phase conjugation and perfect lensing”, *J. Appl. Phys.*, vol. 94, p. 4241, 2003.

[10] J. B. Pendry, “Time reversal and negative refraction”, *Science*, vol. 322, p. 71, 2008.

[11] N. Fang, H. Lee, C. Sun, X. Zhang, “Sub-Diffraction-Limited Optical Imaging with a Silver Superlens”, *Science*, vol. 308, p. 534, 2003.

[12] M. C. K. Wiltshire, J. V. Hajnal, J. B. Pendry, D. J. Edwards, C. J. Stevens, “Metamaterial endoscope for magnetic field transfer: near field imaging with magnetic wires”, *Opt. Express,* vol. 11, p. 709, 2003.

[13] M. J. Freire and R. Marqués, “Planar magnetoinductive lens for three-dimensional subwavelength imaging”, *Appl. Phys. Lett.*, vol. 86, p. 182505, 2005.

[14] S. Maslovski, S. Tretyakov, P. Alitalo, “Near-field enhancement and imaging in double planar polaritons-resonant structures”, *J. Appl. Phys.*, vol. 96, p. 1293, 2004.

[15] M. G. Silveirinha, C. A. Fernandes, and J. R. Costa, “Superlens made of a metamaterial with extreme effective parameters”, *Phys. Rev. B*, vol. 78, p. 195121, 2008.

[16] M. G. Silveirinha, and C. A. Fernandes, “Nonresonant structured material with extreme parameters”, *Phys. Rev. B*, vol. 78, p. 033108, 2008.

[17] M. G. Silveirinha, C. R. Medeiros, C. A. Fernandes, and J. R. Costa, “Experimental verification of broadband superlensing using a metamaterial with an extreme index of refraction”, *Phys. Rev. B*, vol. 81, p. 033101, 2010.

[18] C. Luo, S. G. Johnson, J. D. Joannopoulos, and J. B. Pendry, “All-Angle negative refraction without negative effective index”, *Phys. Rev. B*, vol. 65, p. 201104, 2002.

[19] C. Luo, S. G. Johnson, J. D. Joannopoulos, “All-Angle negative refraction in a three-dimensionally periodic photonic crystal”, *Appl. Phys. Lett.*, vol. 81, p. 2352 2002.

[20] C. Luo, S. G. Johnson, J. D. Joannopoulos, and J. B. Pendry, “Subwavelength Imaging in Photonic Crystals”, *Phys. Rev. B*, vol. 68, p. 045115, 2003.

[21] E. Cubukcu, K. Aydin, E. Ozbay, S. Foteinopoulou, and C. M. Soukoulis, “Subwavelength Resolution in a Two-Dimensional Photonic-Crystal-Based Superlens”, *Phys. Rev. Lett.*, vol. 91, p. 207401, 2003.

[22] P. V. Parimi, W. T. Lu, P. Vodo, and S. Sridhar, “Imaging by flat lens using negative refraction”, *Nature*, vol. 426, p. 404, 2003.

[23] X. Zhang, “Absolute negative refraction and imaging of unpolarized electromagnetic waves by two-dimensional photonic crystals”, *Phys. Rev. B*, vol. 70, p. 205102, 2004.

[24] X. Zhang, “Image resolution depending on slab thickness and object distance in a two-dimensional photonic-crystal-based superlens”, *Phys. Rev. B*, vol. 70, p. 195110, 2004.

[25] A. Berrier, M. Mulot, M. Swillo, M. Qiu, A. Talneau, and S. Anand, “Negative Refraction at Infrared Wavelengths in a Two-Dimensional Photonic Crystal”, *Phys. Rev. Lett.*, vol. 93, p. 073902, 2004.

[26] D. N. Chigrin, S. Enoch, C. M. S. Torres, and G. Tayeb, “Self-guiding in two-dimensional photonic crystals”, *Opt. Express*, vol. 11, p. 1203, 2003.

[27] Z.-Y. Li and L. L. Lin, “Evaluation of lensing in photonic crystal slabs exhibiting negative refraction”, *Phys. Rev. B*, vol. 68, p. 245110, 2003.

[28] C.–H. Kuo and Z. Ye, “Optical transmission of photonic crystal structures formed by dielectric cylinders: Evidence for non-magnetic refraction”, *Phys Rev. E*, vol. 70, p. 056608, 2004.

[29] H.-T. Chien, H.-T. Tang, C.-H. Kuo, C.-C. Chen, Z. Ye, “Directed diffraction without negative refraction”, *Phys. Rev. B*, vol. 70, p. 113101, 2004.

[30] P. A. Belov, C. R. Simovski, and P. Ikonen, “Canalization of subwavelength images by electromagnetic crystals”, *Phys. Rev. B*, vol. 71, p. 193105, 2005.

[31] P. A. Belov, Y. Hao, and S. Sudhakaran, “Subwavelength microwave imaging using an array of parallel conducting wires”, *Phys. Rev. B*, vol. 73, p. 033108, 2006.

[32] P. A. Belov and M. G. Silveirinha, “Resolution of subwavelength imaging devices formed by a wire medium”, *Phys. Rev. E*, vol. 73, p. 056607, 2006.

[33] P. A. Belov, Y. Zhao, S. Sudhakaran, A. Alomainy, Y. Hao, “Experimental study of subwavelength imaging by a wire medium slab”, *Appl. Phys. Lett.*, vol. 89, p. 262109, 2006.

[34] P. A. Belov, Y. Zhao, S. Tse, M. G. Silveirinha, C. R. Simovski, S. Tretyakov, Y. Hao, and C. Parini, “Transmission of images with subwavelength resolution to distances of several wavelengths in the microwave range”, *Phys. Rev. B*, vol. 77, p. 193108, 2008.

[35] P. Ikonen, C. Simovski, S. Tretyakov, P. Belov, and Y. Hao, “Magnification of subwavelength field distributions at microwave frequencies using a wire medium slab operating in the canalization regime”, *Appl. Phys. Lett.*, vol. 91, p. 104102, 2007.

[36] M. G. Silveirinha, P. A. Belov, and C. R. Simovski, “Subwavelength imaging at infrared frequencies using an array of metallic nanorods”, *Phys. Rev. B*, vol. 75, p. 035108, 2007.

[37] M. G. Silveirinha, P. A. Belov, and C. R. Simovski, “Ultimate limit of resolution of subwavelength devices formed by metallic rods”, *Opt. Lett.*, vol. 33, p. 1726, 2008.

[38] P. A. Belov, Y. Hao, “Subwavelength imaging at optical frequencies using a transmission device formed by a periodic layered metal-dielectric structure operating in the canalization regime”, *Phys. Rev. B*, vol. 73, p. 113110, 2006.

[39] Z. Jacob, L. V. Alekseyev, E. Narimanov, “Optical Hyperlens: Far-field imaging beyond the diffraction limit”, *Opt. Express*, vol. 14, p. 8247, 2006.

[40] A. Salandrino, N. Engheta, “Far-field subdiffraction optical microscopy using metamaterials crystals: Theory and simulations”, *Phys. Rev. B*, vol. 74, p. 075103, 2006.

[41] I. I. Smolyaninov, Y.-J. Hung, and C. C. Davis, “Magnifying superlens in the visible frequency range”, *Science*, vol. 315, p. 1699, 2007.

[42] Z. Liu, H. Lee, Y. Xiong, C. Sun, and X. Zhang, “Far-field optical hyperlens magnifying sub-difraction-limited objects”, *Science*, vol. 315, p. 1686, 2007.

[43] R. Merlin, “Radiationless Electromagnetic Interference: Evanescent-Field Lenses and Perfect Focusing”, *Science*, vol. 317, p. 927, 2007.

[44] A. Grbic, L. Jiang, R. Merlin, “Near-Field Plates: Subdiffraction focusing with patterned surfaces”, *Science*, vol. 320, p. 511, 2008.

[45] P. A. Belov, R. Marqués, S. I. Maslovski, I. S. Nefedov, M. G. Silveirinha, C. R. Simovski, and S. A. Tretyakov, “Strong spatial dispersion in wire media in the very large wavelength”, *Phys. Rev. B*, vol. 67, p. 113103, 2003.

[46] M. G. Silveirinha, “Nonlocal homogenization model for a periodic array of ε-negative rods”, *Phys. Rev. E*, vol. 73, p. 046612, 2006.

[47] A. Yariv, P. Yeh, *Optical Waves in Crystals: Propagation and Control of Laser Radiation*, New York: Wiley, 1984.

[48] I. Morris, K. Kline, *Electromagnetic Theory and Geometrical Optics*, New York: Interscience, 1965.

[49] M. G. Silveirinha, “Additional Boundary Condition for the Wire Medium”, *IEEE Trans. Antennas Propag.*, vol. 54, p. 1766, 2006.

[50] M. G. Silveirinha, C. A. Fernandes, J. R. Costa, “Additional boundary condition for a wire medium connected to a metallic surface”, *New J. Phys.*, vol. 10, p. 053011, 2008.

[51] CST Microwave Studio 2008 (http://www.cst.com).

[52] Private Communication with Dr. P. A. Belov.

[53] J. D. Jackson, *Classical Electrodynamics*, 3rd Edition, New York: Wiley, 1998.

III. NEGATIVE REFRACTION AND PARTIAL FOCUSING WITH WIRE MEDIA

III.1. Introduction

Refraction is one of the most fundamental phenomena in optics and forms the basis of imaging devices (e.g. lenses). Such phenomenon describes the change of direction that a light beam undergoes when it passes from a medium to another. The laws of refraction are long-established and were formulated in the seventeenth century by Willebrord Snellius and then published by René Descartes in its present form $n_1 \sin\theta_1 = n_2 \sin\theta_2$, where n_1 and n_2 are the indices of refraction of the media and θ_1 and θ_2 are the angle of incidence and refraction (or transmission), respectively. Since then, it has been widely accepted that when a beam of light passes from one transparent medium to another it is always bent in such a way that the beam emerges from the interface on the opposite side of the surface normal. However, in 1968 Veselago published a study [1] that contradicted such empirical understanding of refraction laws and would have key implications in the image formation and in the manner how it is perceived by the human brain. Specifically, as already briefly mentioned in Chapter II, Veselago theoretically demonstrated that the light refracted in a material with simultaneously negative permittivity and permeability (negative isotropic index of refraction) obeys a reversed Snell's law, so that the refracted wave emerges on the same side of the surface normal. As a consequence, it was theoretically predicted in his manuscript that – if available – a planar slab of a double negative material would permit the focusing of a divergent beam of light rays. Subsequently, as already discussed in the introduction to Chapter II, this idea was further developed many years later by Pendry [2], who showed that besides focusing light rays such double negative medium also enables the restoration of the near-field spectrum. In this chapter, however, we are only interested in the propagating waves associated with the far-field spectrum of the source.

Because there are no naturally available materials with a negative isotropic index of refraction, Veselago's prediction did not receive much attention until recently, when such exotic material was experimental realized in the form of an artificial composite medium (metamaterial) based on thin metallic wires combined with split-ring resonators [3]. Shortly after this finding, the phenomenon of negative refraction was experimentally demonstrated at microwave frequencies using the same metamaterial structure [4]. However, since structuring materials in the nanoscale is truly challenging, the realization of a microstructured material exhibiting a negative isotropic index of refraction at higher frequencies revealed to be extremely complicated. As a result, the phenomenon of negative refraction was only very recently demonstrated at optical frequencies using a three-dimensional metamaterial made of cascaded "fishnet" structures [5].

An alternative possibility to obtain negative refraction is to engineer the dispersion characteristic of photonic crystals [6-7]. However, this solution has also several practical constraints, as pointed out in Chapter II. Another robust solution to achieve negative refraction is through the use of anisotropic media in which not all of the principal components of the permittivity and/or permeability tensors have the same sign [8-14]. This kind of media is designated as indefinite media and enables negative refraction for specific polarizations and directions of propagation. These structures allow negative refraction and consequently a potential focusing effect with the advantage of being much easier to manufacture and very likely less sensitive to losses than materials with negative isotropic index of refraction. Yet another alternative route to obtain all-angle broadband negative refraction was recently introduced in Ref. [15] and is based on a spatially dispersive material formed by a crossed wire mesh.

In this chapter we investigate two different configurations to obtain negative refraction and subsequently, we analyze the prospects of partial focusing of electromagnetic radiation with a flat lens. In Sec. III.2, we propose a new way to realize an indefinite anisotropic material in the microwave regime. We discuss the potential negative refraction effect at the interfaces between the proposed material and air (or dielectric), as well as the partial focusing of electromagnetic radiation by a planar lens of such material. In Sec. III.3, we analyze and extend the negative refraction effect in the nonlocal material formed by nonconnected crossed metallic wires introduced in Ref. [15]. Subsequently, we investigate the possibility of taking advantage of this effect to obtain partial focusing with a planar crossed wires lens.

III.2. Negative Refraction and Partial Focusing with a Local Uniaxial ENG Material formed by Helical Shaped Wires

III.2.1. Introduction

As already mentioned, one of the most effective ways to achieve negative refraction is through the use of indefinite media. In particular, the negative refraction effect using an indefinite anisotropic material was recently demonstrated in the optical domain using an array of metallic nanorods [13-14]. In fact, in the long wavelength limit this structure behaves as an indefinite medium, whose effective permittivity along the direction parallel to the wires is negative, whereas the perpendicular components to the wires of the permittivity tensor are positive. Hence, such configuration provides broadband all-angle negative refraction and partial focusing of *p*-polarized waves[1]. However, such configuration is only effective at optical frequencies where the metals exhibit a plasmonic-type response. At lower frequencies (microwave and low infrared frequencies), owing to the large conductivity of the metals, the array of nanowires has a strongly spatially dispersive response, as already discussed in the previous chapter (see Sec. II.3.1). Consequently, the array of metallic wires behaves quite differently from a material with indefinite parameters and thus the negative refraction is hindered in such range of frequencies.

Despite these difficulties, it has been shown recently [16], that the spatial dispersion effects can be tamed either by increasing the capacitance of the wires or the inductance. It was suggested in Ref. [16] that the capacitance of the wires may be increased by attaching plates to the wires, whereas the inductance may be increased by coating the wires with a magnetic material. The first possibility was further developed in several works [17-21], and a strong negative refraction effect using a wire medium with metallic patches attached was finally demonstrated in [22-23]. Even though very effective, this approach has a drawback: attaching plates to the wires increases dramatically the transverse permittivity of the medium which is obviously undesirable because it deteriorates the matching with the external medium and, consequently, reduces the available bandwidth. On other hand, the second approach based on coated wires with a magnetic material is not practical.

In Ref. [17] it was briefly mentioned an alternative way to increase the inductance of the wires, and thereby may suppress the spatial dispersion effects, that consists in using helical shaped wires instead of straight wires. Such solution may provide a smaller value of the

---

[1] As an aside, it should be noted that negative refraction of *s*-polarized waves can be conversely achieved using anisotropic media for which the permeability component along the direction of propagation is negative, whereas all other permeability components are positive [9].

transverse effective permittivity than the approach based on attached plates and consequently a likely broader bandwidth of operation.

Here, we investigate such an idea to realize an indefinite uniaxial material with a local response at microwave and low infrared frequencies using an array of helical shaped wires. We study the possibility of using such material to obtain a broadband negative refraction effect. In addition, we will also investigate the possibility of focusing *p*-polarized electromagnetic radiation using a planar lens of the proposed metamaterial.

III.2.2. Non-Bianisotropic Helices Medium – Homogenization Model

In this subsection, based on the homogenization model of the artificial medium formed by an array of perfectly electrical conducting (PEC) helical shaped wires (helices) introduced in Ref. [24], we present a brief overview of the nonlocal homogenization model of an alternative configuration of such structured medium (Fig. 3.1).

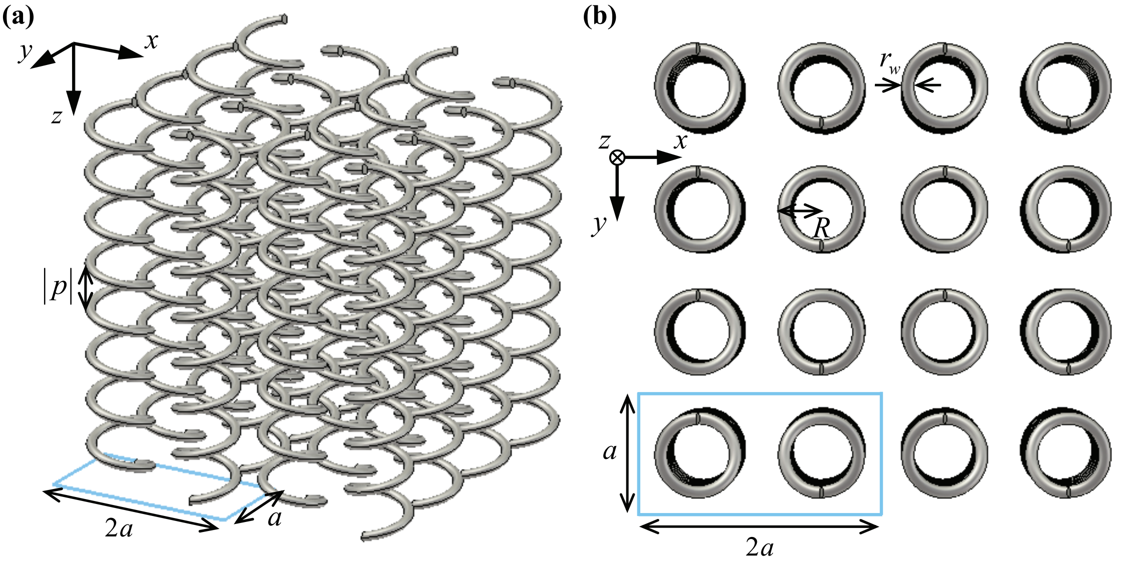

Fig. 3.1. Geometry of the non-bianisotropic helices medium: a periodic array of perfectly electrical conducting helical shaped wires arranged in a rectangular lattice ($2a$ along the x direction and a along the y direction). Each unit cell includes two helices with opposite handedness, specifically one helix right-handed ($p > 0$) and another helix left-handed ($p < 0$). (a) Perspective view; (b) Top view. R represents the radius of the helices, whereas r_w is the wires radius. The helices stand in free-space.

Instead of an array of helices with fixed handedness (right-handed or left-handed helices) arranged in a square lattice with lattice constant a as in [24], we consider a configuration wherein the unit cell is rectangular ($2a$ along the x direction and a along the y direction) and includes two helices with opposite handedness in the same unit cell, i.e., one helix right-handed and another helix left-handed (see Fig. 3.1). The metamaterial structure is then obtained by periodic repetition of the unit cell defined by the primitive vectors $\mathbf{a}_1 = 2a\hat{\mathbf{u}}_x$, $\mathbf{a}_2 = a\hat{\mathbf{u}}_y$, and $\mathbf{a}_3 = |p|\hat{\mathbf{u}}_z$, where p represents the pitch of the helix and is positive ($p > 0$) when the helix is right-handed and negative ($p < 0$) when the helix is left-handed.

The homogenization approach proposed in Ref. [24] is based on a nonlocal dielectric function $\overline{\overline{\varepsilon}}(\omega,\mathbf{k})$, where ω is the frequency and $\mathbf{k}$ is the wave vector, that thoroughly describes the electromagnetic properties of the metamaterial structure [25]. In the same work [24], analytical expressions for the conventional material parameters (effective permittivity, effective permeability, and magnetoelectric coupling parameters) were derived using the following constitutive relation [24-25]:

$$\frac{\overline{\overline{\varepsilon}}}{\varepsilon_0}(\omega,\mathbf{k}) = \overline{\overline{\varepsilon_r}} - \overline{\overline{\xi}}.\overline{\overline{\mu_r}}^{-1}.\overline{\overline{\zeta}} + \left(\overline{\overline{\xi}}.\overline{\overline{\mu_r}}^{-1} \times \frac{\mathbf{k}}{k_0} - \frac{\mathbf{k}}{k_0} \times \overline{\overline{\mu_r}}^{-1}.\overline{\overline{\zeta}} \right) + \frac{\mathbf{k}}{k_0} \times \left(\overline{\overline{\mu_r}}^{-1} - \overline{\overline{\mathbf{I}}} \right) \times \frac{\mathbf{k}}{k_0}, \quad (3.1)$$

where $\overline{\overline{\varepsilon_r}}$ is the relative permittivity tensor, $\overline{\overline{\mu_r}}$ is the relative permeability tensor, $\overline{\overline{\xi}}$ and $\overline{\overline{\zeta}}$ are dimensionless parameters that characterize the magnetoelectric coupling, $k_0 = \omega\sqrt{\varepsilon_0\mu_0}$ is the free-space wave number, and $\overline{\overline{\mathbf{I}}}$ is the identity dyadic.

Since the magnetoelectric coupling (gyrotropy) can only be observed in media that possess no center of symmetry [26], it is expected that using the non-bianisotropic helices medium formed by unit cells that contain a pair of helices with opposite handedness (Fig.

3.1), the bianisotropic effects that are inherent to the standard helices medium configuration [24] are eliminated ($\overline{\overline{\xi}} = \overline{\overline{\zeta}} = 0$). Hence, from Eq. (3.1) the dielectric function of the non-bianisotropic helices medium (Fig. 3.1) should verify the following constitutive relation:

$$\frac{\overline{\overline{\varepsilon}}}{\varepsilon_0}(\omega,\mathbf{k}) = \overline{\overline{\varepsilon}}_r + \frac{\mathbf{k}}{k_0}\times\left(\overline{\overline{\mu}}_r^{\,-1} - \overline{\overline{\mathbf{I}}}\right)\times\frac{\mathbf{k}}{k_0}. \tag{3.2}$$

On the other hand, it is straightforward verify that Eq. (3.2) is equivalent to the following relation:

$$\left.\frac{\overline{\overline{\varepsilon}}}{\varepsilon_0}\right|_{\mathrm{Eq.(3.2)}} = \left.\frac{\overline{\overline{\varepsilon}}}{\varepsilon_0}\right|_{\mathrm{Eq.(3.1)}} + \overline{\overline{\xi}}.\overline{\overline{\mu}}_r^{\,-1}.\overline{\overline{\zeta}} - \left(\overline{\overline{\xi}}.\overline{\overline{\mu}}_r^{\,-1}\times\frac{\mathbf{k}}{k_0} - \frac{\mathbf{k}}{k_0}\times\overline{\overline{\mu}}_r^{\,-1}.\overline{\overline{\zeta}}\right), \tag{3.3}$$

where $\left.\overline{\overline{\varepsilon}}/\varepsilon_0\right|_{\mathrm{Eq.(3.2)}}$ represents the dielectric function of the non-bianisotropic helices medium (Fig. 3.1), whereas $\left.\overline{\overline{\varepsilon}}/\varepsilon_0\right|_{\mathrm{Eq.(3.1)}}$ represents the dielectric function of the standard helices medium that is given by Eq. (15) of Ref. [24]. The constitutive parameters $\overline{\overline{\mu}}_r$, $\overline{\overline{\xi}}$, and $\overline{\overline{\zeta}}$ are obtained from Eqs. (20) of Ref. [24]. Thus, using Eq. (3.3) we obtain the desired dielectric function of the non-bianisotropic helices medium:

$$\frac{\overline{\overline{\varepsilon}}}{\varepsilon_0} = \begin{pmatrix} \varepsilon_t - \dfrac{A^2 k_y^2}{\dfrac{k_0^2}{\beta_{p1}^2} - \dfrac{k_z^2}{\beta_{p2}^2}} & \dfrac{A^2 k_x k_y}{\dfrac{k_0^2}{\beta_{p1}^2} - \dfrac{k_z^2}{\beta_{p2}^2}} & 0 \\ \dfrac{A^2 k_x k_y}{\dfrac{k_0^2}{\beta_{p1}^2} - \dfrac{k_z^2}{\beta_{p2}^2}} & \varepsilon_t - \dfrac{A^2 k_x^2}{\dfrac{k_0^2}{\beta_{p1}^2} - \dfrac{k_z^2}{\beta_{p2}^2}} & 0 \\ 0 & 0 & 1 - \dfrac{1}{\dfrac{k_0^2}{\beta_{p1}^2} - \dfrac{k_z^2}{\beta_{p2}^2}} + \dfrac{A^2 k_0^2}{\left(\dfrac{k_0^2}{\beta_{p1}^2} - \dfrac{k_z^2}{\beta_{p2}^2}\right)^2 + A^2 k_0^2\left(\dfrac{k_0^2}{\beta_{p1}^2} - \dfrac{k_z^2}{\beta_{p2}^2}\right)} \end{pmatrix}, \tag{3.4}$$

where $A = \pi R^2 / p$ and

$$\varepsilon_t = 1 + \frac{(\pi R)^2}{V_{\text{cell}}} \frac{1}{C_1}, \tag{3.5}$$

$$\beta_{p1} = \sqrt{\frac{(2\pi p)^2}{C_0 p^2 V_{\text{cell}} + 8 C_1 \pi^2 R^2 V_{\text{cell}}}}, \tag{3.6}$$

$$\beta_{p2} = \sqrt{\frac{(2\pi)^2}{C_0 V_{\text{cell}}}}. \tag{3.7}$$

$V_{\text{cell}} = a^2 \left|p\right|$ is the volume of the unit cell, and C_0 and C_1 are parameters that only depend on the geometry of the artificial material and are evaluated numerically in Ref. [24].

Now, using Eq. (3.2), it is found after straightforward substitutions that the constitutive parameters that characterize the non-bianisotropic helices medium are given by the following analytical expressions:

$$\overline{\overline{\varepsilon_r}} = \varepsilon_t \left(\hat{\mathbf{u}}_x \hat{\mathbf{u}}_x + \hat{\mathbf{u}}_y \hat{\mathbf{u}}_y\right) + \varepsilon_{zz} \hat{\mathbf{u}}_z \hat{\mathbf{u}}_z,$$

$$\varepsilon_{zz} = 1 - \frac{1}{\dfrac{k_0^2}{\beta_{p1}^2} - \dfrac{k_z^2}{\beta_{p2}^2}} + \frac{A^2 k_0^2}{\left(1 + \dfrac{A^2 k_0^2}{\dfrac{k_0^2}{\beta_{p1}^2} - \dfrac{k_z^2}{\beta_{p2}^2}}\right)\left(\dfrac{k_0^2}{\beta_{p1}^2} - \dfrac{k_z^2}{\beta_{p2}^2}\right)^2}, \tag{3.8}$$

$$\overline{\overline{\mu_r}} = \hat{\mathbf{u}}_x \hat{\mathbf{u}}_x + \hat{\mathbf{u}}_y \hat{\mathbf{u}}_y + \mu_{zz} \hat{\mathbf{u}}_z \hat{\mathbf{u}}_z,$$

$$\mu_{zz} = \frac{1}{1 + \dfrac{A^2 k_0^2}{\dfrac{k_0^2}{\beta_{p1}^2} - \dfrac{k_z^2}{\beta_{p2}^2}}}. \tag{3.9}$$

As one can see, similar to the constitutive parameters of the standard helices medium studied in Ref. [24], the relative permittivity and permeability tensors of the helices medium with suppressed bianisotropic effects are not local parameters, since Eqs. (3.8-3.9) depend explicitly on k_z (z component of the wave vector). Nevertheless, it is worth noting that if β_{p2} is much greater than k_z ($\beta_{p2} >> k_z$), then the term k_z^2 / β_{p2}^2 can be discarded and hence $\overline{\overline{\varepsilon_r}}$ and $\overline{\overline{\mu_r}}$ become exclusively frequency dependent, which means that the electromagnetic response of the metamaterial is local. In particular, the dielectric tensor is anisotropic and indefinite. This topic will be further discussed in the next subsection.

III.2.3. Properties of the Structured Medium: Quasi-Local Response

The goal of this subsection is to characterize the electromagnetic response of the non-bianisotropic helices medium (Fig. 3.1) under plane wave excitation. For this purpose, we want to calculate the dispersion characteristic of the plane waves supported by the structured material. This can be done by solving the following equation [26]:

$$\det\left(\frac{\overline{\overline{\varepsilon}}}{\varepsilon_0}+\frac{1}{k_0}\mathbf{kk}-\frac{k^2}{k_0^2}\overline{\overline{\mathbf{I}}}\right)=0, \tag{3.10}$$

where $\overline{\overline{\varepsilon}} / \varepsilon_0$ is the dielectric function given by Eq. (3.4), $\mathbf{kk} = \mathbf{k} \otimes \mathbf{k}$, and $k^2 = k_x^2 + k_y^2 + k_z^2$. It can be shown that the characteristic equation (3.10) reduces to a fourth degree polynomial in the variable k_0^2 (or equivalently in the variable k_z^2). Thus, the homogenization model described in the previous subsection predicts that the non-bianisotropic helices medium supports four independent plane wave modes. It can be verified that these solutions are associated with two distinct types of excitations: two of them are associated with TM-*z* polarized incident waves (or *p*-polarized waves), whereas the other pair of solutions is associated with TE-*z* polarized incident waves (or *s*-polarized waves). In fact, this polarization separation was expected since in the proposed configuration of the helices medium the bianisotropic effects are eliminated, and hence, there is no excitation of cross-polarized fields, contrarily to what happens in the standard helices medium [24].

In this study, however, we are only interested in the case of propagation in the *xoz*-plane ($k_y = 0$) with the magnetic field along the y direction. In such circumstances, the dispersion characteristic of the plane waves supported by the non-bianisotropic helices medium can be easily calculated using the following relation [28]:

$$k_0^2 \varepsilon_t - \frac{\varepsilon_t}{\varepsilon_{zz}} k_x^2 - k_z^2 = 0, \tag{3.11}$$

where ε_t is given by Eq. (3.5) and ε_{zz} is given by Eq. (3.8). This equation may be reduced to a polynomial equation of second degree in the variable k_0^2

$$\begin{aligned} &-\left(A^2 \beta_{p1}^2 \beta_{p2}^2 \varepsilon_t + \beta_{p2}^2 \varepsilon_t\right) k_0^4 + \left(A^2 k_x^2 \beta_{p1}^2 \beta_{p2}^2 \varepsilon_t + A^2 k_z^2 \beta_{p1}^2 \beta_{p2}^2 + k_x^2 \beta_{p2}^2 \varepsilon_t\right. \\ &\left. + k_z^2 \beta_{p1}^2 \varepsilon_t + k_z^2 \beta_{p2}^2 + \beta_{p1}^2 \beta_{p2}^2 \varepsilon_t\right) k_0^2 - k_z^2 \beta_{p1}^2 \beta_{p2}^2 - k_x^2 k_z^2 \beta_{p1}^2 \varepsilon_t - k_z^4 \beta_{p1}^2 = 0 \end{aligned}. \tag{3.12}$$

Hence, in agreement with Eq. (3.10), Eq. (3.11) also predicts that the non-bianisotropic helices medium supports two independent plane wave modes with magnetic field along the y direction. The emergence of an additional eigenwave is a consequence of the spatially dispersive response of the metamaterial, since as already referred to in the previous chapter (see Sec. II.3.1), in conventional local materials each fixed polarization is associated with a single plane wave mode. Nevertheless, it is expected that the contribution of the high-frequency mode may be discarded when $\beta_{p2} >> k_z$, i.e., under such condition the spatial dispersion effects may be negligible. So, the important question is, "how to get large values for β_{p2}?" The answer is intrinsically related with the geometry of the structure. In fact, as one can see from Eq. (3.7), the parameter β_{p2} is inversely proportional to C_0 and V_{cell}. Thus, in order to get large values for β_{p2} we are interested in geometries in which C_0 and V_{cell} are as small as possible. For a fixed lattice constant a, one can get small values for V_{cell} by considering helices with short pitch p. On the other hand, as one can see from

Fig.2 of Ref. [24], the helices geometry with a small value for the constant C_0 corresponds to a configuration of helices with radius $R = 0.4a$ and wires radius $r_w = 0.05a$.

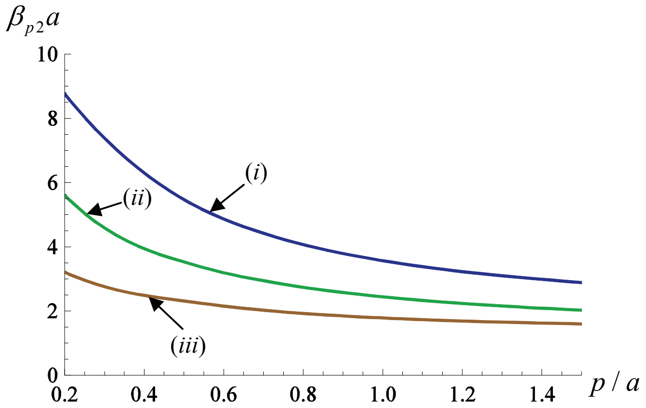

Fig. 3.2. β_{p2} as a function of the normalized helix pitch p for different geometries, calculated using Eq. (3.7). (*i*) $R = 0.4a$ and $r_w = 0.05a$; (*ii*) $R = 0.4a$ and $r_w = 0.01a$; (*iii*) $R = 0.2a$ and $r_w = 0.01a$.

To clarify the discussed dependence of the parameter β_{p2} on the metamaterial geometries, we depict β_{p2} as a function of the helix pitch p in Fig. 3.2. From this figure, and consistent with our previous prediction, one can clearly see that, in fact, by decreasing the helix pitch p the parameter β_{p2} increases. This is particularly true for the configuration of helices with radius $R = 0.4a$ and wires radius $r_w = 0.05a$, such as also anticipated from the behavior of the geometrical constant C_0 illustrated in Fig.2 of Ref. [24]. Hence, it is expected that using a configuration of helices with short pitch p, the spatial dispersion term k_z^2 / β_{p2}^2 in the analytical expression of ε_{zz} may be discarded, and therefore the electromagnetic response of the structured material becomes solely frequency dependent.

In fact, the suppression of the spatial dispersion effects in wire media formed by helical shaped wires with short helix pitch p can be also predicted from a physical point of view. As already explained in Chapter II (see Sec. II.3.1), the spatial dispersion effects emerge in the standard wire medium formed by straight metallic wires mainly due to two physical reasons: firstly, because the metallic wires are good conductors, and secondly, because the wires are spanned over several unit cells. As a consequence of these properties, a localized fluctuation of the electric field may be propagated along a significant number of lattice periods, causing the strongly spatially dispersive response of the medium. However, if we consider helical shaped wires instead of straight wires, the path length along the wires is evidently increased and, consequently, the distance that a perturbation can travel in terms of lattice periods decreases considerably. Therefore, it is also expected from a physical point of view that an array of metallic helices (or helical shaped wires) with short helix pitch p may behave as a local material.

In order to demonstrate in a conclusive manner the possible suppression of the spatial dispersion effects in the proposed medium formed by helical shaped wires (Fig. 3.1), we have calculated the dispersion diagrams for propagation along z direction. Specifically, we illustrate in Fig. 3.3a-b the dispersion characteristics of the non-bianisotropic helices medium (Fig. 3.1) with helices with radius $R = 0.4a$ and wires radius $r_w = 0.05a$ for two configurations with distinct values of helix pitch p: (a) $p = 0.3a$; (b) $p = 0.9a$. In addition, so that we have a benchmark for these results, we have also computed the dispersion characteristic of the standard wire medium formed by straight wires (Fig. 3.3c). The dispersion curves predicted by the homogenization model (solid lines) are compared with the full wave hybrid method results [27] (star symbols). It is clearly seen in Fig. 3.3a-b that the results obtained from both approaches concur well, predicting the existence of two dispersion branches: a transversal mode or quasi-TEM mode (blue curves) and a longitudinal mode or quasi-TM mode (green curves). The agreement between the theoretical and numerical methods is particularly good for relatively low frequencies (roughly, $k_0 a = 0.8$). For higher frequencies, there is a slight lack of agreement that is a consequence of the approximations made in the derivation of the analytical model [24]. On the other hand, the agreement between the nonlocal homogenization results and the full wave hybrid method results for the standard wire medium formed by straight wires is excellent, even for high frequencies (Fig. 3.3c), being the propagation of the TEM mode (blue curves) and the TM mode (green curves) predicted by both models.

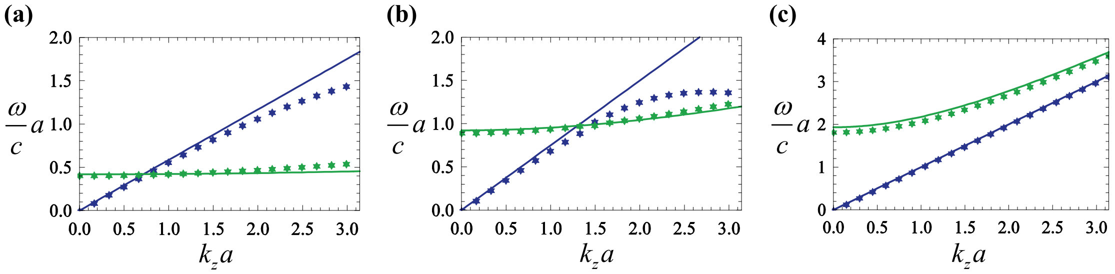

Fig. 3.3. Dispersion diagrams for three different geometries of wire arrays (helical shaped wires and straight wires). (a) Non-bianisotropic helices medium with $R = 0.4a$, $r_w = 0.05a$ and $p = 0.3a$; (b) The same as in (b) but for $p = 0.9a$; (c) Standard wire medium with $r_w = 0.05a$. Solid lines: Homogenization results; Star symbols: full wave numerical results.

The suppression of the spatial dispersion effects is evident if we compare the results of Fig. 3.3a with Fig. 3.3b and Fig. 3.3c. Indeed, it is clear that by decreasing the helix pitch p, or in others words, by increasing the inductance of the wires, the dispersion of the quasi-TM mode (green curves) is dramatically reduced since the slope of the curve tends to become almost flat for small values of p (Fig. 3.3a). Hence, the frequency of the quasi-TM mode becomes almost independent of k_z and, since the group velocity is $v_g = d\omega / dk_z \approx 0$, the mode is unable to propagate in the medium. As a result, in such circumstances the non-bianisotropic helices medium of Fig. 3.1 may be regarded as a local uniaxial Epsilon-Negative (ENG) material.

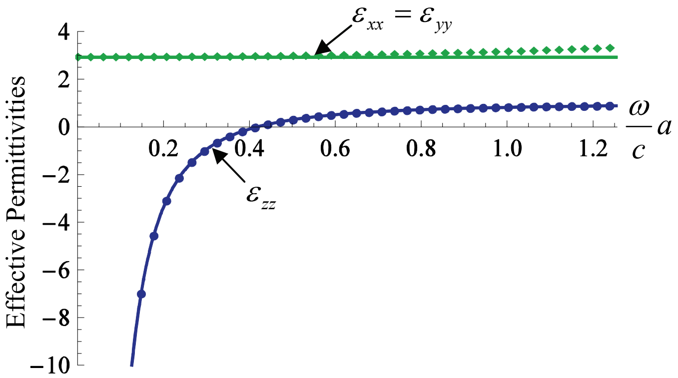

Fig. 3.4. Effective permittivity components as a function of the normalized frequency for an array of helical shaped wires (Fig. 3.1) with $R = 0.4a$, $r_w = 0.05a$, and $p = 0.3a$. The solid lines correspond to the analytical results and are obtained using Eqs. (3.5) and (3.8) discarding the term k_z^2 / β_{p2}^2 (or considering $k_z = 0$), whereas the discrete symbols are numerical results obtained from an homogenization approach based on the Method of Moments (MoM).

In order to demonstrate such fact, are depicted the effective permittivity components in Fig. 3.4 as a function of the frequency, assuming that $k_z^2 / \beta_{p2}^2 = 0$. The accuracy of the analytical results calculated from Eqs. (3.5) and (3.8) is checked against the numerical results obtained from an approach based on the Method of Moments (MoM) [25]. As clearly seen in Fig. 3.4, the agreement between the two distinct approaches is very good. Moreover, it is evident that at low frequencies, specifically for $\omega a / c < 0.4$, the structured material actually behaves as a local uniaxial ENG material with effective permittivity along the direction parallel to the axes of the helices negative ($\varepsilon_{zz} < 0$) and effective permittivity in the perpendicular directions positive ($\varepsilon_{xx} > 0$).

III.2.4. Negative Refraction in an Array of Helical Shaped Wires

Following the results of the previous subsection, here we investigate the potential negative refraction effect achieved at the interfaces of the proposed structured material. As shown in the previous subsection, for low frequencies the artificial medium exhibit a negative effective permittivity along the direction parallel to the axes of the helices, whereas the permittivity in the perpendicular directions is positive (see Fig. 3.4). Hence, we expect that the considered metamaterial may negatively refract p-polarized waves (or TM-z polarized waves) [8]. This is studied in what follows.

III.2.4.1 Properties of the fundamental electromagnetic mode

In order that the electromagnetic fields scattered by the slab of helical shaped wires under TM-z excitation (Fig. 3.5) can be completely characterized, it is useful to study first the properties of the plane wave modes supported by the structured material with further detail.

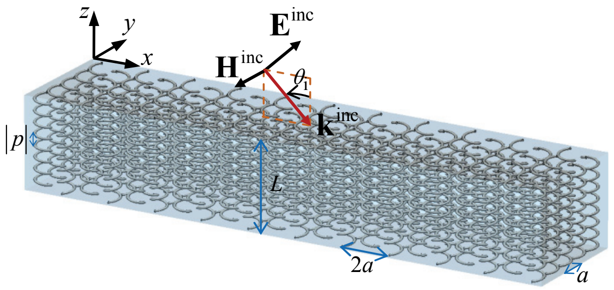

Fig. 3.5. Geometry of the metamaterial slab formed by metallic helical shaped wires. The radius of the helical wires (or helices) is R and the radius of the wires is r_w. The plane of incidence is the *xoz* plane and the wave is TM-z polarized [$\mathbf{k}^{\text{inc}} = (k_x, 0, k_z^{\text{inc}})$, $\mathbf{H}^{\text{inc}} = H^{\text{inc}}\hat{\mathbf{u}}_y$].

In subsection III.2.3 it was shown that, for a fixed frequency, the considered metamaterial slab supports two independent plane waves with magnetic field along the y direction, which means that the structured medium is characterized by a spatially dispersive response. However, it was also proven in subsection III.2.3 that the contribution of the high-frequency mode (quasi-TM mode) may be negligible for metamaterial geometries in which the helix pitch p is short. Hence, in such circumstances the spatial dispersion effects may be suppressed and consequently the wave propagation in the non-bianisotropic helices medium can be described almost exclusively in terms of the fundamental electromagnetic mode. In addition, the longitudinal mode is cut-off for low frequencies, more specifically it only propagates for frequencies $\omega a / c > \beta_{p1} a / \sqrt{1 + A^2 \beta_{p1}^2}$, which corresponds to the frequency in which $\varepsilon_{zz} = 0$. Here, we are only interested in the frequency band wherein $\varepsilon_{zz} < 0$, since it is in this range of frequencies that we expect to achieve a negative refraction effect. Thus, we will only concentrate our attention on the study of the electromagnetic properties of the fundamental mode.

The isofrequency contours of the fundamental plane wave mode, calculated from Eq. (3.12), are depicted in Fig. 3.6 for two different metamaterial configurations.

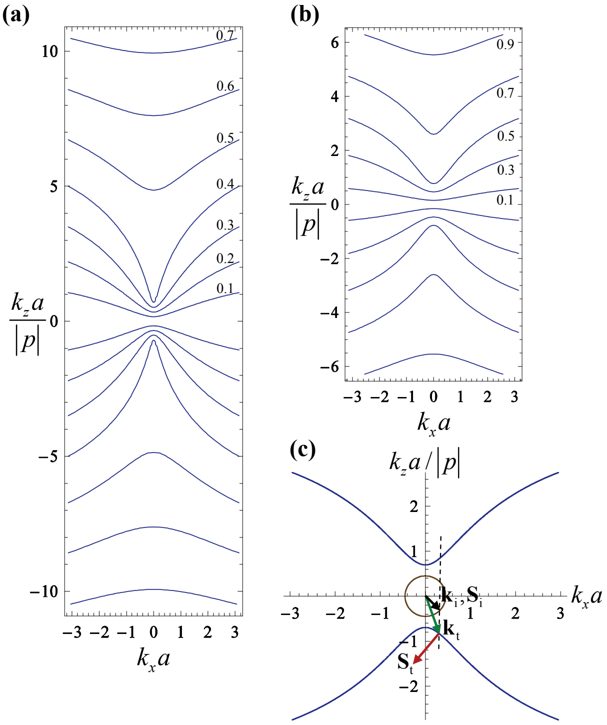

Fig. 3.6. Isofrequency contours of the fundamental plane wave mode supported by the non-bianisotropic helices medium for propagation in the *xoz* plane with magnetic field perpendicular to this plane (Fig. 3.5). (a) $R = 0.4a$, $r_w = 0.05a$, and $p = 0.3a$; (b) $R = 0.4a$, $r_w = 0.05a$, and $p = 0.5a$. In (c) we represent the isofrequency contour of the fundamental mode supported by the metamaterial (blue curves) for the normalized frequency $\omega a / c = 0.45$ and for the same configuration as in (b), as well as the isofrequency contour in the air region (brown circle). The transmitted wave vector $\mathbf{k}_t$ (green arrow) is determined by the conservation of the tangential component of the wave vector k_x, whereas the Poynting vector $\mathbf{S}_t$ (red arrow) is normal to the isofrequency curves and is oriented towards increasing frequencies.

As one can see from Fig. 3.6a-b, the fundamental electromagnetic mode is characterized by hyperbolic shaped isofrequency contours. Hence, as illustrated in Fig. 3.6c, the Poynting vector (energy flow) is always negatively refracted for any angle of incidence (assuming incidence from the air side), since it must be normal to the isofrequency contours. Therefore, this electromagnetic mode undergoes negative refraction at the interface between the non-bianisotropic helices medium and air.

In order to investigate the negative refraction effect at the interfaces between the non-bianisotropic helices medium and air (Fig. 3.5), we consider the geometry shown in the inset of Fig. 3.7, which shows an incoming plane wave with wave vector $\mathbf{k}_\mathrm{i} = \omega / c(\sin\theta_\mathrm{i}, 0, -\cos\theta_\mathrm{i})$ illuminating the considered metamaterial. The angle of refraction θ_t for the energy flow (determined by the Poynting vector of the transmitted wave $\mathbf{S}_\mathrm{t}$) can be calculated using the relation $v_g = \nabla_k \omega(\mathbf{k})$ and taking into account the fact that the projection of the wave vector onto the interface, i.e. the x component of the wave vector k_x, must be preserved [6].

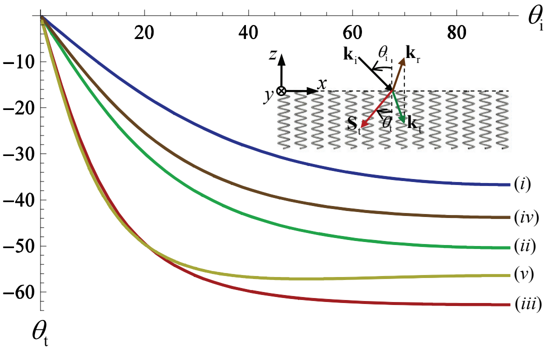

Fig. 3.7. Angle of transmission of the energy flow (Poynting vector) as a function of the angle of incidence for different frequencies of operation and configurations. (*i*) $R = 0.4a$, $r_w = 0.05a$, $p = 0.3a$, and $\omega a / c = 0.25$; (*ii*) $R = 0.4a$, $r_w = 0.05a$, $p = 0.3a$, and $\omega a / c = 0.3$; (*iii*) $R = 0.4a$, $r_w = 0.05a$, $p = 0.3a$, and $\omega a / c = 0.35$; (*iv*) $R = 0.4a$, $r_w = 0.05a$, $p = 0.5a$, and $\omega a / c = 0.45$; (*v*) $R = 0.4a$, $r_w = 0.05a$, $p = 0.5a$, and $\omega a / c = 0.55$. The inset represents the geometry of the problem showing the incident, reflected and refracted waves.

In Fig. 3.7 we depict the angle of transmission θ_{t} as a function of the angle of incidence θ_{i} for different frequencies of operation and two distinct structure configurations. It is clear that for positive angles of incidence, the angle of transmission is negative. Therefore, consistently with the hyperbolic shaped isofrequency contours (Fig. 3.6), the Poynting vector of the transmitted wave $\mathbf{S}_{\mathrm{t}}$ undergoes, indeed, negative refraction at the interface of the non-bianisotropic helices medium with air.

III.2.4.2 Transmission Characteristics

In this subsection, the transmission properties of the metamaterial slab formed by helical shaped wires (Fig. 3.5) are studied under plane wave incidence using the nonlocal homogenization model (Sec. III.2.2) and full wave simulations obtained with an electromagnetic simulator [29]. The negative refraction effect at an interface between the considered metamaterial slab and air (or a dielectric) is then characterized from the obtained transmission properties.

To begin with, we focus our attention on the study of a simple plane wave scattering problem using the nonlocal homogenization model derived in Sec. III.2.2. The metamaterial slab formed by metallic helical shaped wires is assumed infinite and periodic along the x and y directions with lattice period $2a$ and a, respectively, and finite with thickness L along the z direction (Fig. 3.5). The incident wave propagates in the xoz plane ($k_y = 0$) and the incoming magnetic field is polarized along the y direction (see Fig. 3.5). Thus, the magnetic field in the three regions of space can be written as follows (the x dependence and the time variation $e^{j\omega t}$ are suppressed):

$$\begin{aligned} &H_y^{(1)} = H_y^{\text{inc}}(e^{\gamma_0 z} + \rho e^{-\gamma_0 z}), \quad z > 0 \\ &H_y^{(2)} = A_1^+ e^{-jk_z^{(1)} z} + A_1^- e^{+jk_z^{(1)} z} + A_2^+ e^{-jk_z^{(2)} z} + A_2^- e^{+jk_z^{(2)} z}, \quad -L < z < 0 \\ &H_y^{(3)} = H_y^{\text{inc}} t\, e^{\gamma_0 (z+L)}, \quad z < -L \end{aligned} \tag{3.13}$$

where, H_y^{inc} is the incident magnetic field, $\gamma_0 = \sqrt{k_x^2 - \omega^2 \varepsilon_0 \mu_0}$ is the free-space propagation constant, $k_x = \omega\sqrt{\varepsilon_0 \mu_0}\sin\theta_{\text{i}}$, and ρ and t are the reflection and transmission coefficients, respectively. The propagation constants $k_z^{(1,2)}$ [calculated by solving Eq. (3.12) with respect to k_z] and the amplitudes $A_{1,2}^{\pm}$ are associated with the two distinct electromagnetic modes excited inside the metamaterial slab. For each plane wave with magnetic field of the form $\mathbf{H} = H_0 e^{-j\mathbf{k}.\mathbf{r}}\hat{\mathbf{u}}_y$, the corresponding electric field is given by

$$\mathbf{E} = \frac{\eta_0 H_0}{k_0}\left(\frac{k_z}{\varepsilon_t}\hat{\mathbf{u}}_x - \frac{k_x}{\varepsilon_{zz}}\hat{\mathbf{u}}_z\right)e^{-j\mathbf{k}.\mathbf{r}}. \tag{3.14}$$

In order to calculate the reflection and transmission coefficients, we need to impose that the tangential components of the electromagnetic fields (E_x and H_y) are continuous at the interfaces $x = 0$ and $x = -L$. However, as a consequence of the existence of two plane wave modes with the same polarization, these classical boundary conditions are insufficient to solve the scattering problem (Eq. (3.13)). Actually, in order to remove the extra degrees of freedom and thus solve the scattering problem, the classical boundary conditions must be complemented with an additional boundary condition (ABC) at both interfaces. Similar to the scattering problem of an array formed by tilted straight wires solved in the previous chapter (Sec. II.3.1), also here it is necessary to impose that the normal component of the electric field (E_z) is continuous at the interfaces $x = 0$ and $x = -L$ (assuming that the helices stand in air) [30-31]. Such ABC guarantees that the microscopic electric current that flows in each helical shaped wire vanishes at both interfaces, as proved in Ref. [30-31]. Imposing the ABC and the classical boundary conditions, we obtain a 6×6 linear system which can be easily solved numerically with respect to the unknowns.

Now, we are able to calculate analytically the transmission coefficient of the considered system. The negative refraction at the interfaces between the slab of helical shaped wires and air can be investigated using the approach proposed in Ref. [15], which is based on the variation in the phase of $t(\omega,\mathbf{k})=|t|e^{j\phi}$ ($\phi=\arg t$) with k_x. Specifically, it was proven in Ref. [15] that the spatial shift Δ undergone by an incoming beam when it crosses an arbitrary slab (see Fig. 3.8a) is equal to the slope of ϕ, i.e., $\Delta = d\phi/dk_x$. In particular, negative refraction occurs when Δ is negative, or equivalently, when ϕ decreases with k_x. It is worth noting that such criterion is completely general, and the only assumption is that the amplitude of the transmission coefficient varies smoothly with k_x.

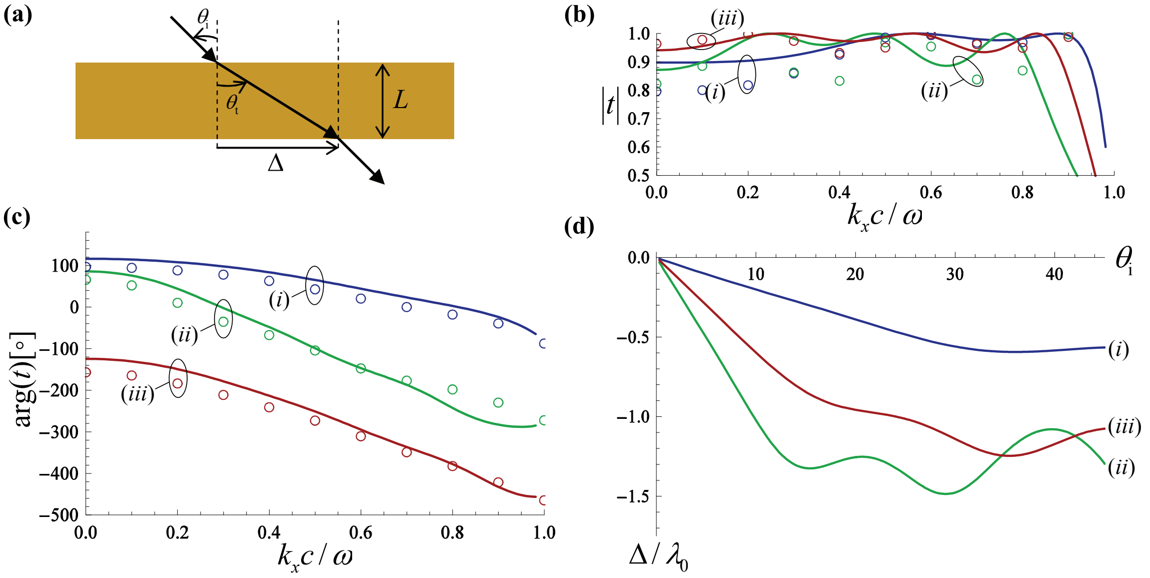

Fig. 3.8. (a) Illustration of the spatial shift Δ undergone by a beam that illuminates an arbitrary slab. (b) Amplitude and (c) phase of the transmission coefficient as a function of the normalized k_x for different structure configurations. Solid lines: nonlocal homogenization model; Discrete symbols: full wave results [29]. (d) Spatial shift Δ as a function of the angle of incidence θ_i for different structure configurations calculated using the analytical model based on the homogenization theory. (*i*) $R=0.4a$, $r_w=0.05a$, $p=0.3a$, $\omega a/c=0.35$, and $L=7a$; (*ii*) $R=0.4a$, $r_w=0.05a$, $p=0.3a$, $\omega a/c=0.4$, and $L=7a$; (*iii*) $R=0.4a$, $r_w=0.05a$, $p=0.5a$, $\omega a/c=0.55$, and $L=10a$.

Following such criterion, we show in Fig. 3.8b-c the dependence of the transmission coefficient (amplitude and phase) on the normalized transverse component of the wave vector k_x, using both the nonlocal homogenization model and full-wave simulations [29]. Firstly, it is important to highlight the good agreement between the nonlocal homogenization results and the full wave simulation results, further demonstrating the accuracy of the homogenization model derived in Sec. III.2.2. On the other hand, Fig. 3.8b shows that the amplitude of the transmission coefficient varies slowly with k_x and is close to unity for all propagating waves, satisfying in this manner the requirement of Ref. [15], besides indicating that the non-bianisotropic helices medium is well matched to free-space. In addition, one can see in Fig. 3.8c that the phase of the transmission coefficient ϕ decreases steadily with k_x, which undoubtedly proves the emergence of negative refraction at the interfaces of the considered metamaterial slab. Such evidence can be confirmed in Fig. 3.8d, wherein it is depicted the spatial shift Δ as a function of θ_i obtained using the analytical model based on the homogenization theory. It can be seen that Δ is indeed always negative for any positive angle of incidence θ_i. In fact, the negative refraction effect in the metamaterial slab formed by helical shaped wires may be quite strong, particularly for frequencies slightly below $\omega a / c = \beta_{p1} a / \sqrt{1 + A^2 \beta_{p1}^2}$ (this corresponds to the frequency in which $\varepsilon_{zz} = 0$). For instance, for $\omega a / c = 0.4$, an incoming beam with $\theta_\mathrm{i} = 33^{\circ}$ undergoes a spatial shift $\Delta = -1.35\lambda_0$ when it crosses a metamaterial slab with a thickness of only $L = 0.45\lambda_0$ (see Fig. 3.8d(*ii*)). As expected, the negative refraction effect becomes progressively weaker away from the frequency corresponding to $\varepsilon_{zz} = 0$. However, for $\omega a / c = 0.35$ an incoming beam with $\theta_\mathrm{i} = 33^{\circ}$ still suffers a considerable spatial shift

$\Delta = -0.59\lambda_0$, even though the thickness of the slab is only $L = 0.39\lambda_0$ (see Fig. 3.8d(*i*)). Although the absolute value of the negative spatial shift decreases by decreasing the frequency of operation, the negative refraction effect can be observed over a wide frequency band within the range corresponding to $\varepsilon_{zz} < 0$. Specifically, it was verified in additional studies (not shown here) that the negative refraction is observed in nearly 60% of the frequency band below the plasma frequency $\omega a / c = \beta_{p1} a / \sqrt{1 + A^2 \beta_{p1}^2}$. Of course, for frequencies corresponding to $\varepsilon_{zz} > 0$ an incoming beam is positively refracted.

Next, we consider a modified configuration of the non-bianisotropic helices medium that is formed by "segmented" helices instead of cylindrical ones (see inset of Fig. 3.9). The motivation for considering such alternative structure is that it may be much easier to fabricate using printed circuit technology. Specifically, this alternative configuration may be fabricated using a planar design, i.e., several layers of boards with printed metallic strips and connected by vias, similar to the mushroom structures [20-21].

In order that this modified structure (C2 in inset of Fig. 3.9) may mimic closely the electromagnetic response of the original structure (C1 in inset of Fig. 3.9), the area of the transverse cross section of the metallic wires as well as the fraction of volume of metal in the unit cell are chosen the same as in the cylindrical helices. As a result, we define the following geometrical parameters to describe the modified geometry: $w_1 = \sqrt{\pi} r_w$ and $w_2 = w_1 + (l_p - |p|)/3$ (see inset of Fig. 3.9), where $l_p = \sqrt{(2\pi R)^2 + |p|^2}$ represents the length of a cylindrical helix pitch.

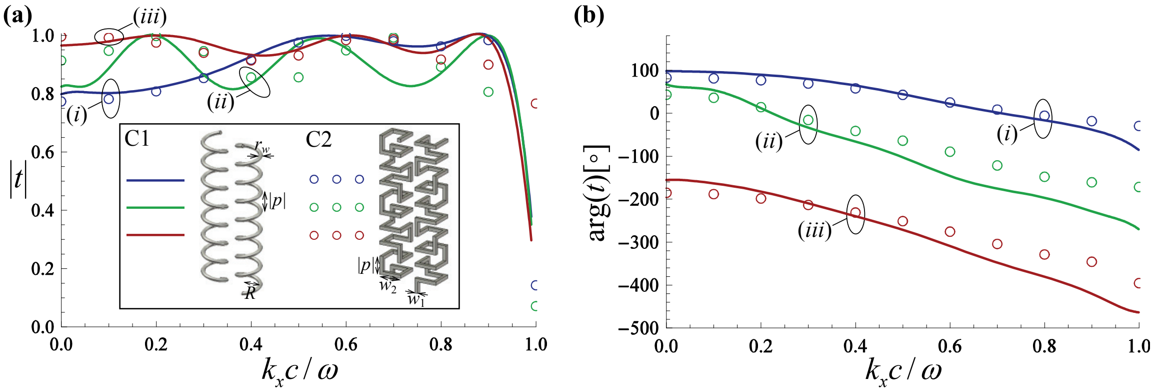

Fig. 3.9. Full-wave results [29] of the amplitude (a) and phase (b) of the transmission coefficient as a function of the normalized k_x for the non-bianisotropic helices medium formed by cylindrical helices (solid lines) and for a modified structure formed by segmented helices (discrete symbols). (*i*) $R = 0.4a$, $r_w = 0.05a$, $p = 0.3a$, $\omega a/c = 0.35$, and $L = 7a$; (*ii*) $R = 0.4a$, $r_w = 0.05a$, $p = 0.3a$, $\omega a/c = 0.4$, and $L = 7a$; (*iii*) $R = 0.4a$, $r_w = 0.05a$, $p = 0.5a$, $\omega a/c = 0.55$, and $L = 10a$. Note that in the modified configuration (C2 in the inset of (a)) R and r_w are replaced by $w_1 = \sqrt{\pi} r_w$ and $w_2 = w_1 + (l_p - |p|)/3$, where $l_p = \sqrt{(2\pi R)^2 + |p|^2}$ represents the length of a cylindrical helix pitch.

To verify the accuracy of the segmented helices approximation, the transmission coefficients of both original and approximated configurations are compared in Fig. 3.9. Specifically, the figure shows the amplitude and phase of the transmission coefficients of the two configurations as a function of the normalized transverse component of the wave vector k_x, calculated using the electromagnetic simulator [29]. One can see that the general agreement between the amplitudes and phases of the two transmission coefficients is quite good. Consistently with the transmission coefficient for the metamaterial slab formed by cylindrical helices, it is seen that the amplitude of the transmission coefficient for the metamaterial slab formed by segmented helices is close to unity for all propagating waves, whereas the phase of t is a decreasing function of k_x with slope very similar to the slope of the phase of the original geometry. Hence, it is expected that the modified configuration mimics closely the electromagnetic response of the original configuration formed by cylindrical helices and similarly enables a strong negative refraction effect.

III.2.4.3 Gaussian beam excitation

To further confirm the findings of Secs. III.2.4.1-2 and demonstrate in a conclusive manner the appearance of negative refraction at the interfaces between a slab of helical shaped wires (Fig. 3.5) and air, here we consider the scenario wherein the metamaterial slab is illuminated by an incoming Gaussian beam with transverse magnetic polarization (TM-z polarized). Firstly, we use the derived nonlocal homogenization model (Sec. III.2.2) to analyze the refraction of a Gaussian beam at the interfaces of an infinite width metamaterial slab. In a later stage, and so that the homogenization results are validated, the electromagnetic response of a finite width metamaterial slab illuminated by a beam with Gaussian profile is simulated using CST Microwave Studio [29].

To begin with, we will consider a Gaussian beam excitation with beam waist w_0, angle of incidence θ_{i}, and placed at $z = z_0$ in front of the metamaterial slab (Fig. 3.5). The magnetic field created by the considered source can be expanded in a Fourier integral of plane waves (spatial Fourier harmonics),

$$H_y^{\mathrm{GB}}(x,z) = \int_{-\infty}^{\infty} H_y^{\mathrm{GB}}(\omega,k_x) e^{\gamma_0(z-z_0)} e^{-jk_x x} dk_x \text{, where } H_y^{\mathrm{GB}}(\omega,k_x) = \frac{e^{-\frac{1}{4}\left(k_x-\frac{\omega}{c}\sin\theta_i\right) w_0^2} w_0}{2\sqrt{\pi}} \quad (3.17)$$

The response of the system to this excitation can be obtained by analyzing the scattering of each plane wave of (3.17), and then adding up for all scattered waves. Thus, the magnetic field in the three regions of space can be written as follows:

$$\begin{aligned}
H_y^{(1)}(x,z) &= \int_{-\infty}^{\infty} H_y^{\mathrm{GB}}(\omega,k_x)\left(e^{\gamma_0(z-z_0)} + \rho(\omega,k_x) e^{-\gamma_0(z+z_0)}\right) e^{-jk_x x} dk_x, \quad z > 0 \\
H_y^{(2)}(x,z) &= \int_{-\infty}^{\infty} H_y^{\mathrm{GB}}(\omega,k_x) H_y^{(2)}(k_x,z) e^{-\gamma_0 z_0} e^{-jk_x x} dk_x dk_x, \quad -L < z < 0 \quad , \qquad (3.18) \\
H_y^{(3)}(x,z) &= \int_{-\infty}^{\infty} H_y^{\mathrm{GB}}(\omega,k_x) t(\omega,k_x) e^{\gamma_0(z+L-z_0)} e^{-jk_x x} dk_x dk_x, \quad z < -L
\end{aligned}$$

where $H_y^{\mathrm{GB}}(\omega, k_x)$ is given by Eq. (3.17), $H_y^{(2)}(k_x, z)$ is the magnetic field inside the slab $(-L < z < 0)$ and defined in Eq. (3.13), and $\rho(\omega, k_x)$ and $t(\omega, k_x)$ are the reflection and transmission coefficients obtained by solving the plane wave scattering problem (Eq. (3.13)). Using the above equations we are able to calculate the magnetic field profile in all regions of space.

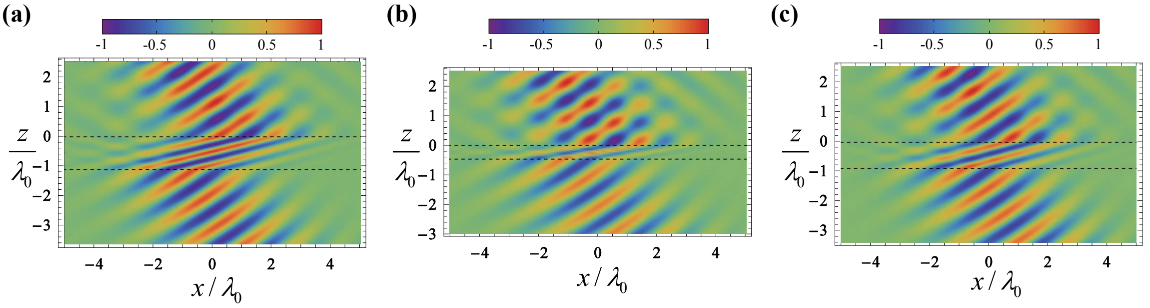

Fig. 3.10. Time snapshot of the normalized magnetic field $H_y(t=0)$ calculated using Eq. (3.18). A Gaussian beam with transverse magnetic polarization characterized by $2w_0 = 4\lambda_0$ and an incident angle of $\theta_{\mathrm{i}} = 33^{\circ}$ illuminates a structured slab formed by helical shaped wires. The metamaterial slab is periodic along the x and y directions. The black dashed lines represent the interfaces of the slab. (a) $R = 0.4a$, $r_w = 0.05a$, $p = 0.3a$, $\omega a / c = 0.35$, and $L = 20a$; (b) $R = 0.4a$, $r_w = 0.05a$, $p = 0.3a$, $\omega a / c = 0.4$, and $L = 7a$; (c) $R = 0.4a$, $r_w = 0.05a$, $p = 0.5a$, $\omega a / c = 0.55$, and $L = 10a$.

In Fig. 3.10 we represent time snapshots $(t = 0)$ of the magnetic field associated with a Gaussian beam characterized by an angle of incidence $\theta_{\mathrm{i}} = 33^{\circ}$ and a beam waist $2w_0 = 4\lambda_0$ for different structure configurations, calculated from Eq. (3.18). In all figures it is manifest that the beam undergoes a significant negative spatial shift Δ, demonstrating the emergence of strong negative refraction. Specifically, the spatial shift suffered by the Gaussian beam, calculated by looking to the maximum amplitude of the magnetic field profiles at the input and output interfaces, is: (a) $\Delta \approx -1.65\lambda_0$; (b) $\Delta \approx -1.38\lambda_0$; (c) $\Delta \approx -1.205\lambda_0$. These values are strongly consistent with the results for the spatial shift Δ shown in Fig. 3.8d, and calculated from the slope of the phase of the transmission coefficient. It is also evident from the results of Fig. 3.10 that the considered metamaterial slab is well-matched to free-space, since it is almost imperceptible any field reflection at both interfaces. This is completely consistent with the magnitude of the transmission coefficient shown in (Fig. 3.8b).

In order to confirm the previous results based on homogenization theory, we have simulated the electromagnetic response of the metamaterial slab illuminated by a beam with Gaussian profile using the electromagnetic simulator [29]. However, due to the difficulty in modeling the homogenized metamaterial structure formed by cylindrical helices (C1 in inset of Fig. 3.9) in CST Microwave Studio, we have simulated instead the electromagnetic response of the modified configuration formed by segmented helices (C2 in inset of Fig. 3.9). The structured metamaterial slab is assumed to be periodic along y direction with period a, and finite along the x direction with width $W_x = 122a$. In all the simulated structures, the lattice constant was taken equal to $a = 5\,\mathrm{mm}$. The incoming beam with Gaussian profile is also considered periodic along y direction and along the x direction is characterized by a beam waist $2w_0 = 3\lambda_0$ at the frequency of operation. Since a Gaussian beam excitation is not directly available in CST Microwave Studio 2010, the desired beam is created using an approach based on the simultaneous excitation of 11 adjacent waveguide ports. The electrical width of each port is about $0.27\lambda_0$ at each frequency of operation, and its amplitude and phase are chosen so that the wave radiated by the port array mimics closely the field profile of a Gaussian beam propagating along a direction $\theta_i = 33^{\circ}$ in the *xoz* plane. In all the simulations, the host dielectric is assumed to be air and the effects of metallic losses are taken into account by assuming that the constituent metallic elements are made of copper ($\sigma = 5.8\times 10^{7}\ \mathrm{S/m}$).

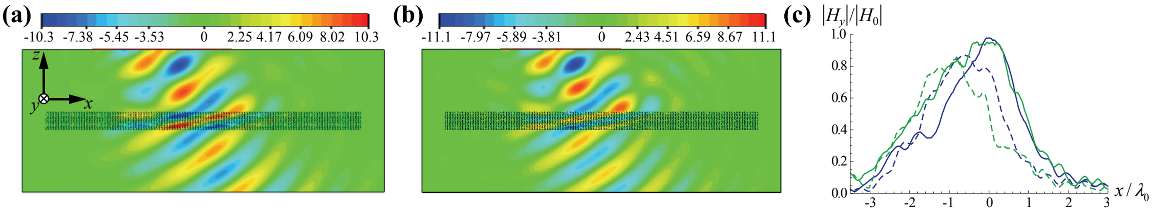

Fig. 3.11. Time snapshot of the magnetic field $H_y(t=0)$ [A/m] obtained from full-wave simulations done in the electromagnetic simulator [29]. A Gaussian beam with transverse magnetic polarization characterized by $2w_0 = 3\lambda_0$ and an incident angle $\theta_i = 33^\circ$ illuminates a finite width metamaterial slab formed by segmented helices (see inset of Fig. 3.9). The metamaterial slab is finite with width W_x along x direction and periodic along y direction with lattice period $a = 5\text{ mm}$. The remaining geometrical parameters of the structure are: $w_1 = 0.05\sqrt{\pi}a$, $w_2 \simeq 0.832a$, $p = 0.3a$, and $L = 7a$; (a) $\omega a / c = 0.35$, (b) $\omega a / c = 0.4$; (c) Normalized magnetic field profile of the Gaussian beam at the input interface (solid lines) and at the output interface (dashed lines) for the cases (a) (blue lines) and (b) (green lines).

The time snapshots $(t=0)$ of the normal y component of the magnetic field obtained with CST Microwave Studio for two different frequencies of operation are depicted in Fig. 3.11a-b. These results clearly show that the Gaussian beam is bent in an unusual way at both interfaces, confirming the prediction made in the previous subsection based on the negative slope of the phase of the transmission coefficient (see Fig. 3.9). Moreover, the simulation results appear to be qualitatively consistent with the homogenization results shown in Fig. 3.10 for the original metamaterial structure formed by cylindrical helices. In order to check such fact, the magnetic field profiles at the input (solid lines) and output (dashed lines) interfaces of the structured slab are depicted in Fig. 3.11c. They undoubtedly show that the Gaussian beam is negatively refracted by the metamaterial slab and that the spatial shift Δ undergone by the beam is quantitatively similar to the values of the spatial shift for the homogenized configuration formed by cylindrical helices (Fig. 3.5). Specifically, the values for the spatial shift inferred from Fig. 3.11c for the cases associated with panel (a) and (b) are, respectively, $\Delta \approx -0.6\lambda_0$ and $\Delta \approx -1.2\lambda_0$, which are reasonably consistent with the values of Δ obtained from the homogenization model of the structure configuration formed by cylindrical helices (see Fig. 3.8d and discussion of the results of Fig. 3.10). Hence, these results further demonstrate that the modified metamaterial configuration formed by segmented helices mimics, indeed, the electromagnetic response of the homogenized structure formed by cylindrical helices, and thus such structure also enables a strong negative refraction. It is also worth noting from the results of Fig. 3.11 that, similar to the homogenized structure (Fig. 3.10), in this modified configuration formed by segmented helices the level of reflections is also very weak, indicating in this manner that the metamaterial structure is well-matched to free-space.

III.2.5. Partial Focusing by a Planar Lens formed by Helical Shaped Wires

As already mentioned in the introduction to this chapter, the concept of negative refraction has led to novel fundamental approaches and potential applications in optics, being the partial focusing of rays emerging from a point source and impinging on a flat slab perhaps the most interesting possibility. Hence, given the successful observation of negative refraction at the interfaces between the metamaterial slab formed by helical shaped wires and air, here we investigate the possibility of taking advantage of this phenomenon to obtain partial focusing with a planar lens.

III.2.5.1 Guidelines for the design of the flat lens

In order to study the possibility of partial focusing, we suppose that a line source is placed at a distance d_1 from the front interface of the metamaterial slab (inset of Fig.3.12a), and we investigate what is the required thickness L for the slab so that the radiation of the source is refocused to a point located at a distance $d_1 = d_2$ from the back interface. In general, this thickness depends on the angle of incidence θ_i.

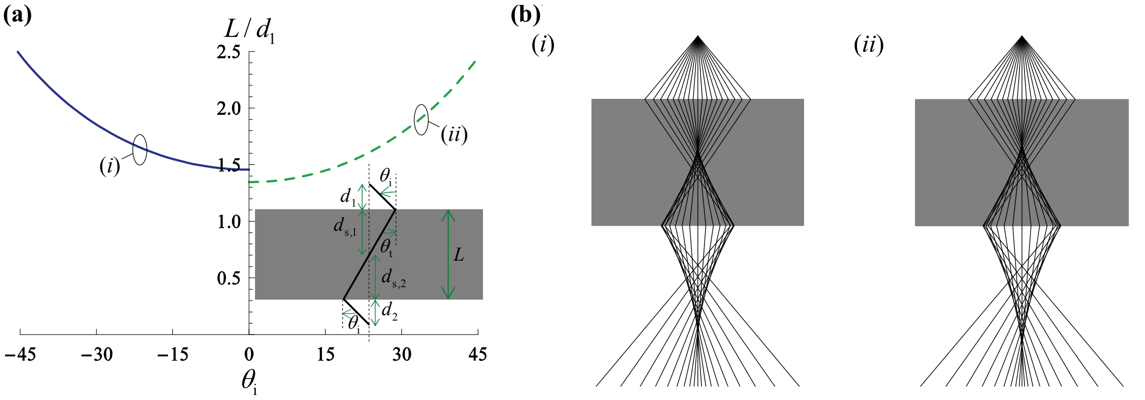

Fig.3.12. (a) Normalized thickness of the metamaterial slab as a function of the angle of incidence calculated in order that $d_1 = d_2$. (*i*) $R = 0.4a$, $r_w = 0.05a$, $p = 0.3a$, and $\omega a / c = 0.28$; (*ii*) $R = 0.4a$, $r_w = 0.05a$, $p = 0.5a$, and $\omega a / c = 0.45$. The inset represents the geometry of the problem. (b) Ray-tracing diagrams showing that the structured material refocuses the rays coming from a magnetic line source both inside and outside the slab. The rays represent the direction of the Poynting vector (energy flow). The source is placed at a distance $d_1 = 0.5L$ from the front interface, the thickness of the slab is $L = 20a$, and the remaining parameters are the same as in (a): (*i*) same parameters as (a*i*), and (*ii*) same parameters as (a*ii*).

From the inset of Fig.3.12a and using simple geometrical arguments, it is straightforward to obtain the following equations:

$$d_1 \left|\tan\theta_i\right| = d_{s,1} \left|\tan\theta_t\right|, \tag{3.19}$$

$$d_2 \left|\tan\theta_i\right| = (L - d_{s,1}) \left|\tan\theta_t\right|, \tag{3.20}$$

The angle θ_t represents the angle of refraction of the energy flow (determined by Poynting vector of the transmitted wave) and is calculated using the relation $v_g = \nabla_k \omega(\mathbf{k})$ in the same manner as in Sec. III.2.4.1 (see Fig. 3.7). Then, substituting Eq. (3.19) in Eq. (3.20) and considering that $d_1 = d_2$ we easily obtain the following formula for the normalized thickness of the slab L

$$\frac{L}{d_1} = 2\left|\frac{\tan\theta_{\mathrm{i}}}{\tan\theta_{\mathrm{t}}}\right|. \tag{3.21}$$

In Fig.3.12a we depict the required normalized thickness for the slab as function of the angle of incidence for two different configurations, characterized using Eq. (3.21). We only show the curve associated with each configuration for positive or negative angles of incidence, since it is evident that by symmetry $L(\theta_{\mathrm{i}})$ is an even function of θ_{i}. As seen from Fig.3.12a, the required thickness for the slab is not constant and depends on the angle of incidence. This was expected, since as shown in Fig. 3.7, the angle of transmission θ_{t} is a nonlinear function of θ_{i}. Hence, unlike what happens in Veselago's lens where $\theta_{\mathrm{t}} = -\theta_{\mathrm{i}}$ and consequently the thickness $L = 2d_1$ provides perfect focusing[2], this structured slab does not possess pairs of pure aplanatic points [32]. Nevertheless, despite this non-ideal characteristic, the proposed lens may enable a partial focusing of the radiation. To illustrate this possibility, we depict in Fig.3.12b the ray-tracing diagrams showing the path of the rays inside and outside the slab for $d_1 = 0.5L$. Clearly, the rays coming from the line source (located above the slab) are partially refocused inside the slab, and also after crossing the metamaterial lens at a partial focus located at a distance $d_1 \approx d_2$.

III.2.5.2 Imaging a magnetic line source

To verify the ray-tracing diagrams and characterize the effects of diffraction, here we consider the scenario where a magnetic line source (infinitely extended along the y direction) is placed at a distance d_1 above the helical shaped wires slab (Fig. 3.13a). The

---

[2] In order to avoid misunderstanding, it should be underlined that in this context perfect focusing has nothing to do with the restoration of the near-field and consequent super-resolution, but only with the fact that all the light rays (far-field) converge into the same exact geometrical point.

magnetic field radiated by the line source is of the form $H_y = (A/4j)H_0^{(2)}\left((\omega/c)\rho\right)$, where A is some constant that depends on the line current, ρ is the radial distance to the source, and $H_0^{(2)} = J_0 - jY_0$ is the Hankel function of second kind and order zero. Theoretically, the line source can be decomposed into a spectrum of plane waves, i.e., the Hankel function can be represent as a Fourier integral of plane waves. Hence, considering that the magnetic line source is located at $z = d_1$, its magnetic field is of the form:

$$H_y(x,z) = \frac{A}{\pi}\int_0^{\infty}\frac{1}{2\gamma_0}e^{-\gamma_0|z-d_1|}\cos(k_x x)dk_x. \tag{3.22}$$

Now, similarly to what was done in the derivation of Eq. (3.18), the magnetic field in the free regions of space can be written in terms of Sommerfeld-type integrals:

$$\begin{aligned}
H_y^{(1)}(x,z) &= \frac{A}{\pi}\int_0^{\infty}\frac{1}{2\gamma_0}\left(e^{-\gamma_0|z-d_1|} + \rho(\omega,k_x)e^{-\gamma_0(z+d_1)}\right)\cos(k_x x)dk_x, \quad z>0\\
H_y^{(2)}(x,z) &= \frac{A}{\pi}\int_0^{\infty}\frac{1}{2\gamma_0}H_y^{(2)}(k_x,z)e^{-\gamma_0 d_1}\cos(k_x x)dk_x, \quad -L<z<0 \qquad ,\\
H_y^{(3)}(x,z) &= \frac{A}{\pi}\int_0^{\infty}\frac{1}{2\gamma_0}t(\omega,k_x)e^{\gamma_0(z+L-d_1)}\cos(k_x x)dk_x, \quad z<-L
\end{aligned} \tag{3.23}$$

where $H_y^{(2)}(k_x, z)$ is the magnetic field inside the slab ($-L < z < 0$) and defined in Eq. (3.13), and $\rho(\omega,k_x)$ and $t(\omega,k_x)$ are the reflection and transmission coefficients obtained by solving the plane wave scattering problem (Eq. (3.13)). Using the above equations we have calculated the magnetic field profile in all regions of space.

In Fig. 3.13b the density plots of the normalized squared amplitude of the magnetic field $|\mathbf{H}|^2$ are depicted in the xoz plane for the same metamaterial configurations of the ray-tracing diagrams of Fig.3.12b.

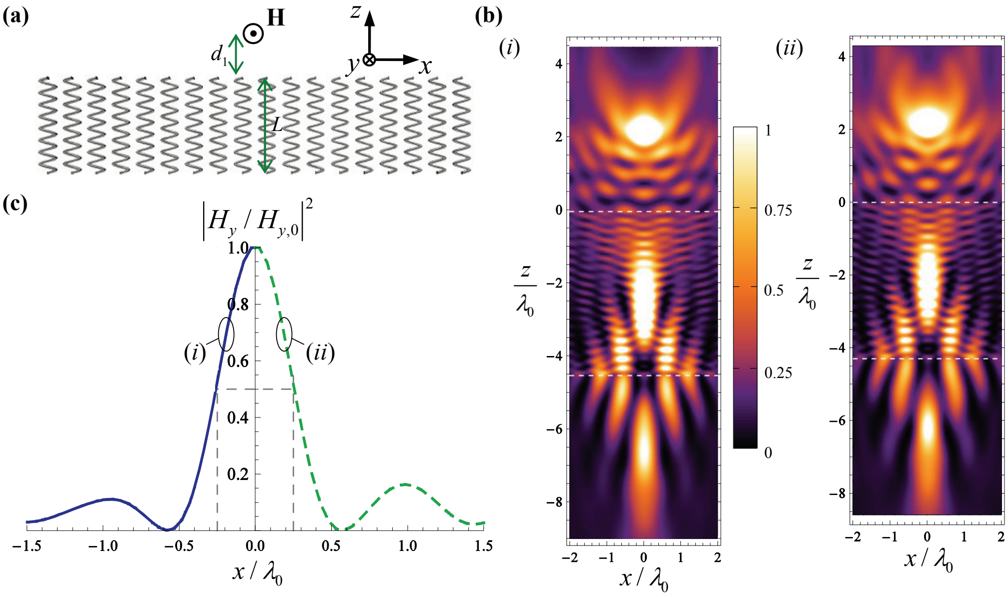

Fig. 3.13. Geometry of the problem: a magnetic line source is placed at a distance d_1 above the helical shaped wires lens. (b) Squared (normalized) amplitude of the magnetic field $|\mathbf{H}|^2$. (*i*) $R = 0.4a$, $r_w = 0.05a$, $p = 0.3a$, $\omega a / c = 0.28$, and $L = 100a$; (*ii*) $R = 0.4a$, $r_w = 0.05a$, $p = 0.5a$, $\omega a / c = 0.45$, and $L = 60a$. The white dashed lines represent the interfaces of the slab. (c) Amplitude of the normalized $|\mathbf{H}|^2$ at the focal plane ($z = -(L + d_1)$). The parameters are the same as in (b): (*i*) same parameters as (b*i*), and (*ii*) same parameters as (b*ii*). We only show the magnetic field profiles for $x < 0$ or $x > 0$, since it is obvious that $|\mathbf{H}|^2$ is an even function with respect to the x direction.

In both figures it is evident an intense and elongated focal point of the magnetic field inside the helical shaped wires lens, and also after the structured lens. The slight aberration along the z direction results from the aforementioned fact that the angle of transmission θ_t inside the lens is a nonlinear function of θ_i. Clearly, these results are completely consistent with the ray-tracing diagrams of Fig.3.12b, and prove that a slab thick enough of helical shaped wires can work, indeed, as a planar focusing device, redirecting the electromagnetic radiation of a p-polarized source to a narrow spot at the focal plane. Moreover, and consistent with the results of Sec. III.2.4.3 for a Gaussian beam excitation (see Fig. 3.10), it is visible from Fig. 3.13b that the helical shaped wires lens is well-matched to free-space, since it is hardly noticeable any field reflections in the region above the lens (where the source is located).

The resolution of the this structured lens is limited by diffraction, since the half-power beamwidth (HPBW) at the focal plane is $\lambda_0 / 2$ (see Fig. 3.13c) as in any conventional optical system. Nevertheless, and despite the referred resolution restriction, the considered metamaterial lens has the important property that the imaging characteristics are independent of the position of the source because of the flat interfaces.

III.2.6. Concluding Remarks

In Sec. III.2, we have shown that a metamaterial structure formed by helical shaped wires (or helices) behaves effectively as a local (with no spatial dispersion) uniaxial ENG material and, as a result, enables a strong negative refraction effect over a wide frequency band. It was demonstrated that as an alternative to the arrays of metallic wires loaded with metallic patches (multilayered mushroom-type metamaterial), the considered structure formed by arrays of helical shaped wires also enables the suppression of the strong spatial dispersion effects that are inherent to wire media at microwave and low infrared frequencies. The proposed configuration may have the advantage of being better matched to the surrounding medium (e.g., free-space) than the mushroom-type metamaterial structure, and hence the level of reflections at their interfaces may be weaker. Finally, and taking advantage of the phenomenon of negative refraction, we have also shown the possibility of using the proposed metamaterial structure to design a planar lens that provides partial focusing. The reported results were obtained using a derived homogenization model and then fully confirmed by full wave simulations [29], showing a remarkable agreement.

III.3. Negative Refraction and Partial Focusing by a Crossed Wire Mesh

III.3.1. Introduction

In the previous section we have shown that the suppression of the spatial dispersion effects that are inherent to wire media at microwave and low infrared frequencies is directly related to the emergence of the phenomenon of negative refraction. Even though in this specific situation the nonlocal response of the arrays of metallic wires may hinder the phenomenon of negative refraction, in other circumstances it may open novel routes to obtain negative refraction. In particular, in a recent publication [15] a distinct approach was proposed to obtain all-angle broadband negative refraction at low frequencies that relies on the spatially dispersive response of a wire metamaterial structure formed by nonconnected crossed metallic wires.

Following these findings, in this section we will give further insights on the negative refraction effect in a crossed wire mesh. Particularly, the full wave numerical results of Ref. [15] that demonstrate unequivocally the emergence of negative refraction at the interfaces of the crossed wire mesh will be complemented with numerical results based on nonlocal homogenization theory. In addition, we investigate partial focusing of electromagnetic waves by a flat lens of nonconnected crossed metallic wires. Specifically, this is firstly analyzed numerically using both homogenization theory and full-wave simulations, and subsequently it will be experimentally verified. Finally, it will be also discussed the phenomenon of negative refraction and partial focusing in modified crossed wire mesh configurations in which the angle between the arrays of parallel wires is different from 90°. The physical motivation behind the study of these modified configurations is the prospect of boost the strength of the negative refraction effect by increasing the angle between the two sets of parallel wires.

III.3.2. The Crossed Wire Mesh - Homogenization Model

The metamaterial considered here consists of a crossed wire mesh of nonconnected metallic wires with radius r_w and arranged in a square lattice with lattice constant a. The two arrays of parallel wires are orthogonal to each other and are placed at a distance of $a/2$ from each other. The orientation of the two wire arrays is determined by the perpendicular unit vectors $\hat{\mathbf{u}}_1=(1,0,1)/\sqrt{2}$ and $\hat{\mathbf{u}}_2=(-1,0,1)/\sqrt{2}$ (Fig. 3.14). The wires are embedded in a dielectric with relative permittivity ε_h and thickness L.

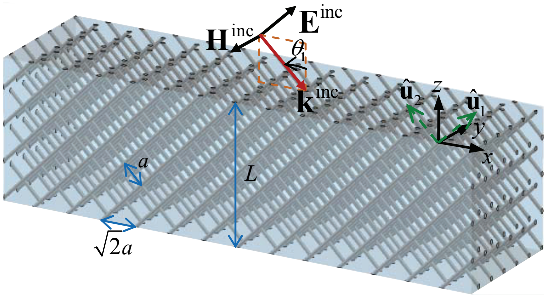

Fig. 3.14. Geometry of the crossed wires metamaterial formed by two orthogonal arrays of nonconnected metallic wires. One set of wires is oriented along the direction defined by $\hat{\mathbf{u}}_1$, whereas the complementary set is oriented along $\hat{\mathbf{u}}_2$. The distance between perpendicular adjacent planes of wires is $a/2$. The plane of incidence is the xoz plane and the incident wave is TM-z polarized [$\mathbf{k}^{\text{inc}}=(k_x,0,k_z^{\text{inc}})$, $\mathbf{H}^{\text{inc}}=H^{\text{inc}}\hat{\mathbf{u}}_y$].

In the long wavelength regime ($\lambda >> a$) the "double wire medium" can be described using homogenization techniques [15, 33-36], being characterized by the following dielectric function

$$\overline{\overline{\varepsilon}}_{eff}=\varepsilon_h\left(\hat{\mathbf{u}}_y\hat{\mathbf{u}}_y+\varepsilon_{11}\hat{\mathbf{u}}_1\hat{\mathbf{u}}_1+\varepsilon_{22}\hat{\mathbf{u}}_2\hat{\mathbf{u}}_2\right) \quad . \tag{3.24}$$

Assuming that the wires are perfectly electrical conducting (PEC), the permittivity components ε_{11} and ε_{22} are given by,

$$\varepsilon_{ii}\left(\omega,k_i\right)=1-\frac{\beta_p^2}{\varepsilon_h\left(\omega/c\right)^2-k_i^2},\quad i=1,2 \tag{3.25}$$

where c is the speed of light in vacuum, $\mathbf{k}=(k_x,k_y,k_z)$ is the wave vector, $k_i=\mathbf{k}.\hat{\mathbf{u}}_i$, and $\beta_p=[2\pi/(\ln(a/2\pi r_w)+0.5275)]^{1/2}/a$ is the plasma wave number.

Before considering the more complicated problem of radiation of a source above the metamaterial lens, let us concentrate first on the analysis of a simple plane-wave scattering problem such that the incident wave vector is in the xoz plane ($k_y=0$) and the incoming magnetic field is polarized along the y direction, as illustrated in Fig. 3.14. Under this excitation, the dispersion characteristic of the plane wave modes supported by the considered structured material are given by the following dispersion characteristic

$$\frac{k_1^2}{k^2-\varepsilon_h\left(\omega/c\right)^2\varepsilon_{11}}+\frac{k_2^2}{k^2-\varepsilon_h\left(\omega/c\right)^2\varepsilon_{22}}=1, \tag{3.26}$$

which, as shown in Ref. [15], is equivalent to a polynomial equation of third degree in the variable k_z^2. Thus, the homogenization model predicts that the crossed wire mesh supports three independent plane wave modes with the magnetic field along the y direction, an effect which is only possible because of the strongly nonlocal response of the metamaterial [33-36], since for conventional local materials each fixed polarization is associated with a single plane wave. Here, we write the magnetic field in the three regions of space as follows (the x dependence and the time variation $e^{j\omega t}$ of the fields are suppressed),

$$\begin{aligned}
H_y^{(1)} &= H_y^{\text{inc}}(e^{\gamma_0 z}+\rho e^{-\gamma_0 z}),\quad z>0\\
H_y^{(2)} &= A_1^+e^{-jk_z^{(1)}z}+A_1^-e^{+jk_z^{(1)}z}+A_2^+e^{-jk_z^{(2)}z}+A_2^-e^{+jk_z^{(2)}z}+\\
&\qquad A_3^+e^{-jk_z^{(3)}z}+A_3^-e^{+jk_z^{(3)}z},\quad -L<z<0\\
H_y^{(3)} &= H_y^{\text{inc}}t\,e^{\gamma_0(z+L)},\quad z<-L
\end{aligned} \tag{3.27}$$

In the above, H_y^{inc} is the incident field, $\gamma_0 = \sqrt{k_x^2 - \omega^2 \varepsilon_0 \mu_0}$ is the free space propagation constant, $k_x = \omega \sqrt{\varepsilon_0 \mu_0} \sin\theta_{\text{i}}$, being θ_{i} the angle of incidence, and ρ and t are the reflection and transmission coefficients, respectively. The propagation constants $k_z^{(1,2,3)}$ [calculated by solving Eq. (3.26) with respect to k_z] and the amplitudes $A_{1,2,3}^{\pm}$ are associated with the electromagnetic modes excited inside the metamaterial slab. For each plane wave with magnetic field of the form $\mathbf{H} = H_0 e^{-j\mathbf{k}.\mathbf{r}} \hat{\mathbf{u}}_y$, the corresponding electric field is given by

$$\mathbf{E} = \frac{H_0}{\omega \varepsilon_0 \varepsilon_h} \left(\frac{k_2}{\varepsilon_{11}} \hat{\mathbf{u}}_1 - \frac{k_1}{\varepsilon_{22}} \hat{\mathbf{u}}_2 \right) e^{-j\mathbf{k}.\mathbf{r}}. \tag{3.28}$$

In order to calculate the reflection and transmission coefficients, it is necessary to impose the following boundary conditions:

$$E_x \text{ and } H_y \text{ are continuous at } z = -L \text{ and } z = 0, \tag{3.29a}$$

$$\mathbf{J}_{d,\text{av}}.\hat{\mathbf{u}}_1 = 0,\ \mathbf{J}_{d,\text{av}}.\hat{\mathbf{u}}_2 = 0 \text{ at } z = -L^+ \text{ and } z = 0^- \tag{3.29b}$$

The first set of boundary conditions corresponds to the classical boundary conditions which impose that the tangential electric and magnetic fields are continuous at the interfaces. The second set corresponds to the so-called additional boundary conditions (ABCs) introduced in Refs. [31, 37], and guarantee that the electric current that flows along each individual metallic wire vanishes at both interfaces [for the definition of the averaged current $\mathbf{J}_{d,\text{av}}$ in Eq. (3.29b) the reader is referred to Refs. [31, 37]]. It is worth noting that in this case where there is more than one wire inside the unit cell the continuity of the normal component of the electric field multiplied by the host permittivity cannot be regarded as equivalent to all the ABCs [37], in contrast to, for example, the tilted wire medium considered in Chapter II.

Once again, these additional boundary conditions are necessary to remove the degrees of freedom characteristic of nonlocal materials, which are manifested through the existence of "additional waves". In this manner, the scattering problem is reduced to an 8×8 linear system, which can be easily numerically solved (see Ref. [37] for further details).

III.3.3. Negative Refraction by the Crossed Wire Mesh

Here, we shed more light on the phenomenon of negative refraction in the crossed wire mesh introduced in Ref. [15], giving further physical insights and presenting new numerical results based on nonlocal homogenization theory.

As described in Ref. [15], the key ingredient for the emergence of negative refraction is the fact that the crossed wire mesh supports, for propagation in the *xoz* plane (Fig. 3.14) and long wavelengths, an electromagnetic mode with hyperbolic shaped isofrequency contours (Fig. 3.15).

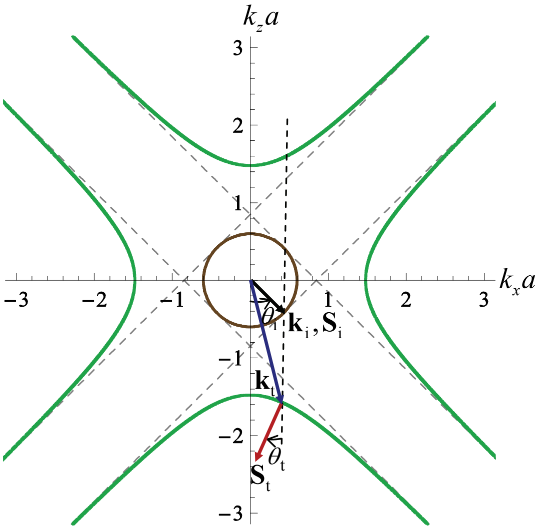

Fig. 3.15. Isofrequency contour of the fundamental plane wave mode supported by the crossed wire mesh (Fig. 3.14) for the normalized frequency $\omega a / c = 0.6$, $\varepsilon_h = 1$ and $r_w = 0.05a$ (green lines), as well as the isofrequency contour in the air region (brown circle). The gray dashed lines represent the asymptotes of the two hyperbolas. The transmitted wave vector $\mathbf{k}_t$ (blue arrow) is determined by the conservation of the tangential component of the wave vector k_x at the interface, whereas the Poynting vector $\mathbf{S}_t$ (red arrow) is normal to the isofrequency curves and is oriented towards increasing frequencies.

As illustrated in Fig. 3.15, this electromagnetic mode undergoes negative refraction at the interfaces with air. One can easily see that the Poynting vector (energy flow) is always negatively refracted for any incident wave vector (or angle of incidence) since it must be normal to the isofrequency contours. On the other hand, the transmitted wave vector is positively refracted, making an acute angle with the Poynting vector as in indefinite media.

Despite some similarities between these isofrequency contours and those of indefinite materials as, for example, the isofrequency contours of the structured medium formed by helical shaped wires studied in the previous subsection (Fig. 3.6), there is an evident and significant difference between them. The isofrequency contours of a conventional indefinite anisotropic material consist of a single hyperbola and hence only yield negative refraction when the interface is normal to the principal axis along which the permittivity is negative (see Fig. 3.6). On the other hand, the isofrequency contour of the considered spatially dispersive material consists of two hyperbolas with asymptotes running along the directions $\hat{\mathbf{u}}_1$ and $\hat{\mathbf{u}}_2$ (see Fig. 3.15), and consequently enables negative refraction if the interface is normal either to the x or to the z direction. In fact, the physical mechanism behind the negative refraction in the crossed wire mesh is fundamentally different from the mechanism exploited in indefinite materials. While in indefinite anisotropic media the hyperbolic isofrequency contours and, consequently, the negative refraction effect are related to the sign of the principal elements of the permittivity and permeability tensors, in the crossed wire mesh they are simply rooted in the geometry of the structure, as is explained in detail below.

In order to give an intuitive physical picture of the mechanism that yields negative refraction in the crossed wire mesh, let us consider each array of parallel tilted wires that make up the crossed wires metamaterial separately (Fig. 3.16a).

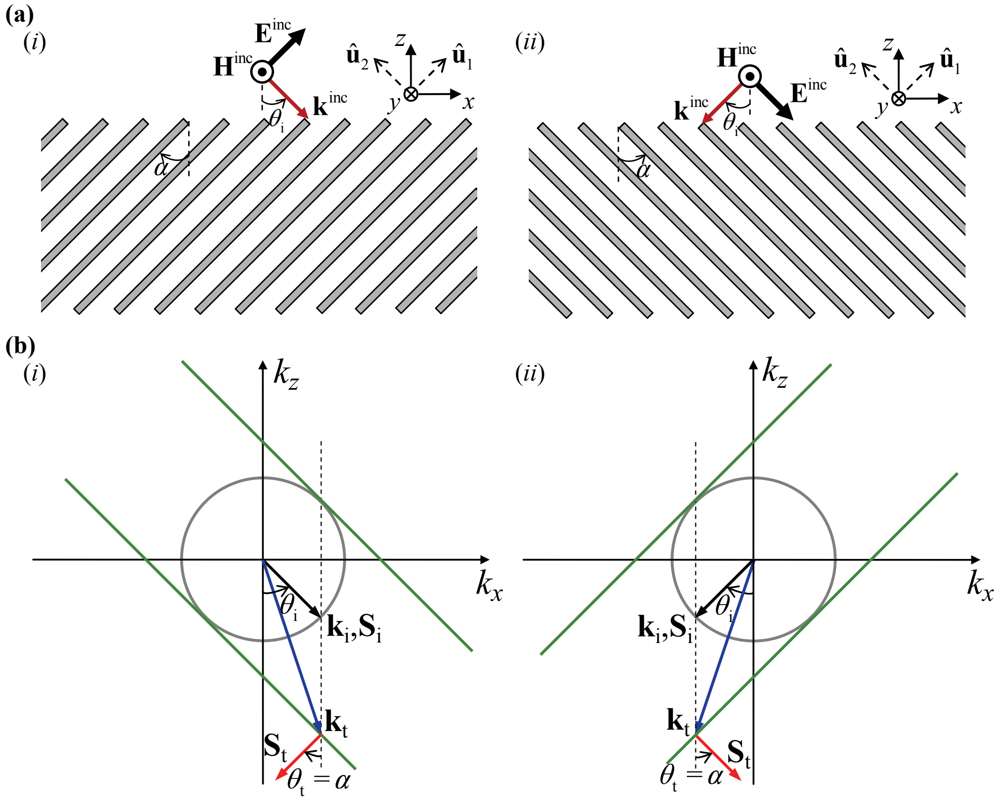

Fig. 3.16. (a) The two arrays of tilted wires that form the crossed wire mesh (Fig. 3.14). (*i*) Array of parallel wires with wires tilted by an angle $\alpha = -45^{\circ}$ (wires directed along $\hat{\mathbf{u}}_1$); (*ii*) Array of parallel wires with wires tilted by an angle $\alpha = 45^{\circ}$ (wires directed along $\hat{\mathbf{u}}_2$). (b) The isofrequency contours of the TEM mode supported by the tilted wire medium configurations of (a) (green lines), as well the isofrequency contour in the air region (gray circle). (*i*) $\alpha = -45^{\circ}$; (*ii*) $\alpha = 45^{\circ}$; The remaining parameters are $\varepsilon_h = 1$ and $r_w = 0.05a$. The transmitted wave vector $\mathbf{k}_{\mathrm{t}}$ (blue arrow) is determined by the conservation of the tangential component of the wave vector k_x, whereas the Poynting vector $\mathbf{S}_{\mathrm{t}}$ (red solid arrow) is normal to the isofrequency curves and oriented along the increasing frequencies.

The electromagnetic response of the arrays of tilted wires was already studied in Chapter II. It was demonstrated that such arrays of wires perform pixel-to-pixel imaging, working in such a way that for any angle of incidence θ_{i} the angle of transmission inside the metamaterial slab is invariant and equal to $\theta_{\mathrm{t}} = \alpha$. This property clearly implies that for a certain range of incident angles, the group velocity (which is parallel to the Poynting vector) will suffer negative refraction.

To demonstrate this property, we analyze the isofrequency contours of the TEM mode supported by the tilted wire medium. As already discussed in Sec. II.3.1, the TEM mode becomes the dominant propagating mode in the wire medium when the wires are densely packed ($a / L_w \to 0$), being its dispersion characteristic given by $\mathbf{k}.\hat{\mathbf{u}}_i = \pm(\omega / c)\sqrt{\varepsilon_h}$ [31, J.5], where $\hat{\mathbf{u}}_i = \hat{\mathbf{u}}_1$ for the configuration of Fig. 3.16a(*i*) and $\hat{\mathbf{u}}_i = \hat{\mathbf{u}}_2$ for the configuration of Fig. 3.16a(*ii*). This equation is equivalent to $-k_x \sin\alpha + k_z \cos\alpha = \pm(\omega / c)\sqrt{\varepsilon_h}$, where α is the angle between the wires direction and the *z*-axis (see Fig. 3.16a). Thus, the isofrequency contours of the TEM mode for the tilted wire medium configuration of Fig. 3.16a(*i*) correspond to two planar surfaces normal to the direction of the wires $\hat{\mathbf{u}}_1$, as represented in Fig. 3.16b(*i*). Conversely, the isofrequency contours of the TEM mode for the configuration illustrated in Fig. 3.16a(*ii*) correspond to two planar surfaces normal to the $\hat{\mathbf{u}}_2$ direction, as shown in Fig. 3.16b(*ii*). Therefore, since the Poynting vector is normal to the isofrequency contours, it follows that the transmission angle is necessarily such that $\theta_{\mathrm{t}} = \alpha$, as already anticipated. Moreover, as a consequence of this property that $\theta_{\mathrm{t}} = \alpha$ for any angle of incidence, the isofrequency contours predict that the tilted wire medium may enable negative refraction when the angle of incidence verify $\theta_{\mathrm{i}}\alpha < 0$. This means that for the tilted wire medium configuration illustrated in Fig. 3.16a(*i*) negative refraction occurs for positive angles of incidence, and conversely, negative refraction arises in the configuration of Fig. 3.16a(*ii*) for all the range of negative angles of incidence. For more details about the negative refraction effect in the tilted wire medium the reader is referred to Ref. [J.5].

What is really interesting to note from Fig. 3.16b(*i*)-(*ii*) is that the isofrequency contours of the TEM mode supported by both tilted wire medium configurations correspond to the asymptotes of the hyperbolic isofrequency contours of the crossed wire mesh (Fig. 3.15). Therefore, this suggests that the phenomenon of negative refraction in the crossed wire mesh is, indeed, rooted in the geometry of the structure. Specifically, the emergence of negative refraction in the crossed wires metamaterial (Fig. 3.14) can be intuitively understood by noting that each array of parallel wires provides a different channel of propagation for the incoming wave, and that the dominant channel, i.e. the channel that is better coupled to the incoming wave, is such that the angle of refraction of the energy flow is negative. Thus, a wave that illuminates the metamaterial with a positive angle of incidence $\theta_{\mathrm{i}} > 0$ interacts mainly with the set of wires directed along $\hat{\mathbf{u}}_1$, and conversely an incident wave with negative angle of incidence $\theta_{\mathrm{i}} < 0$ will be transmitted essentially by the array of wires oriented along $\hat{\mathbf{u}}_2$.

Next, in order to complement the MoM results presented in Ref. [15] and graphically demonstrate the emergence of negative refraction in the crossed wire mesh, we use the nonlocal homogenization model (Sec. III.3.2) to investigate the refraction of a Gaussian beam at the interfaces of an infinite width metamaterial slab. As in Sec. III.2.4.3, we use Fourier theory to write the incoming beam as a superposition of planes waves, in the form of a Sommerfeld-type integral. Following this approach, we can calculate the magnetic field distribution in all space using again Eq. (3.18).

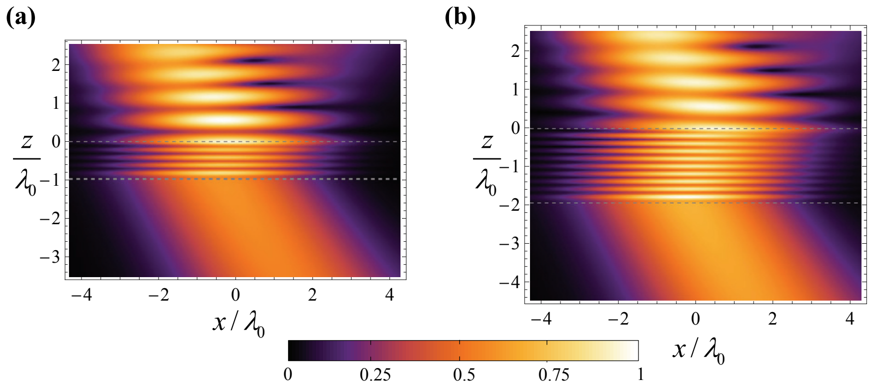

Fig. 3.17. Normalized amplitude of the magnetic field $|H_y|$ inside and outside the crossed wire mesh calculated using the nonlocal homogenization approach. The incoming wave (illuminating the slab from above) has a Gaussian beam profile and is characterized by $2w_0 = 4\lambda_0$ and an incident angle of $\theta_i = 33^\circ$. The metamaterial slab is periodic along the x and y directions. The gray dashed lines represent the interfaces of the slab. The frequency of operation is $\omega a / c = 0.6$, the radius of the wires is $r_w = 0.05a$, and the permittivity of the host is $\varepsilon_h = 1$. (a) $L = 10a$; (b) $L = 20a$.

In Fig. 3.17 we present the calculated normalized amplitude of the magnetic field inside and outside the crossed wire mesh for different thicknesses of the slab. The results clearly show that the Gaussian beam is negatively refracted at both interfaces of the slab. Moreover, these results reveal to be qualitatively very similar to the MoM results presented in Fig. 4 of Ref. [15], confirming in this manner the accuracy of the nonlocal homogenization model. Particularly, the spatial shift suffered by the beam in the two examples is of the same order of the numerical results reported in Ref. [15]. In addition, the level of reflections perceptible in both results of Fig. 3.17 is also very similar to the numerical results of Ref. [15]. As explained in Ref. [15], this reflection is a consequence of the slight impedance mismatch between the structured material and free-space, owing to the fact that the effective impedance of the metamaterial is relatively low.

III.3.4. Partial Focusing by a Planar Lens formed by Crossed Metallic Wires

Following the results of the previous subsection, which confirm the emergence of negative refraction at the interfaces of a crossed wire mesh, and originally introduced in Ref. [15], here we investigate partial focusing by a flat slab of this structured material, similar to the focusing effect achieved with the helical shaped wires lens analyzed in Sec. III.2.5.

Firstly, we provide the guidelines for the design of a planar crossed lens. Next, we numerically study the imaging of a magnetic line source by the proposed lens. In addition, we also analyze the imaging of a more realistic electric current source by the lens. Finally, we report our experimental results that confirm the partial focusing of electromagnetic radiation, based on a fabricated crossed wires lens prototype.

III.3.4.1 Guidelines for the design of the flat lens

Here, using the same geometrical argumentation as in Sec. III.2.5.1, we investigate what should be the thickness L of the crossed wires lens so that the electromagnetic radiation of a point source placed at a distance d_1 from the front interface is partial focused at a distance $d_1 = d_2$ from the back interface.

The required normalized thickness for the slab as a function of the angle of incidence is depicted in Fig. 3.18a. Similar to the helical shaped wires lens (see Fig.3.12a), also here the required thickness is angle-dependent, as a consequence of the nonlinear relation between the angle of incidence θ_i and the angle of transmission θ_t (see Fig. 2 in Ref. [15]). This angle-dependency implies that the light rays will not converge into a single perfect point, as already mentioned in Sec. III.2.5.1. However, the proposed structured lens should enable a partial focusing of the radiation somewhat similar to what was demonstrated in Sec. III.2.5 using a uniaxial ENG material formed by helical shaped wires.

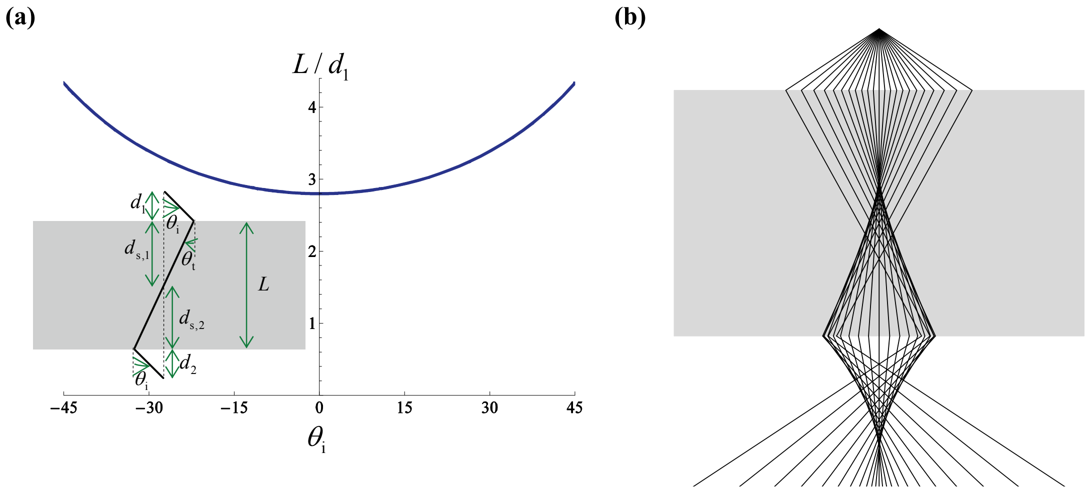

Fig. 3.18. (a) Normalized thickness of the metamaterial slab as a function of the angle of incidence calculated in order that $d_1 = d_2$. The frequency of operation is $\omega a / c = 0.6$, the radius of the wires is $r_w = 0.05a$, and the permittivity of the host is $\varepsilon_h = 1$. The inset represents the geometry of the problem. (b) Ray-tracing diagram showing that the structured material refocuses the rays coming from a line source both inside and outside the slab. The rays represent the direction of the Poynting vector (energy flow). The source is placed at distance $d_1 = 0.25L$ from the front interface and the thickness of the slab is $L = 20a$.

From Fig. 3.18a, it is clear that the thickness of the slab should be chosen so that $L > 2.8d_1$ to ensure that $d_1 \approx d_2$. Taking this into account, we represent in Fig. 3.18b the ray-tracing-diagram showing the path of the rays inside and outside the slab for $d_1 = 0.25L$. It is seen that the rays coming from the line source (located above the slab) are partially refocused inside the slab, and also after passing through the metamaterial lens at a partial focus located at a distance $d_1 \approx d_2$. Other numerical tests that we have performed suggest that $d_1 = 0.25L$ is a good compromise solution, which despite the non-ideality of the lens yields a well-defined focus at the image plane.

III.3.4.2 Imaging a magnetic line source

In order to verify the results of the previous subsection and to characterize the imaging properties of the considered structure, in the following we study the canonical problem where a magnetic line source (infinitely extended along y direction) is placed at a distance d_1 above the crossed wires slab (Fig. 3.19a). Using the same approach as in Sec. III.2.5.2 (Eqs. 3.22-3.23) based on the decomposition of the electromagnetic fields radiated by the line source into a spectrum of plane waves, we have calculated the magnetic field profile in all regions of space.

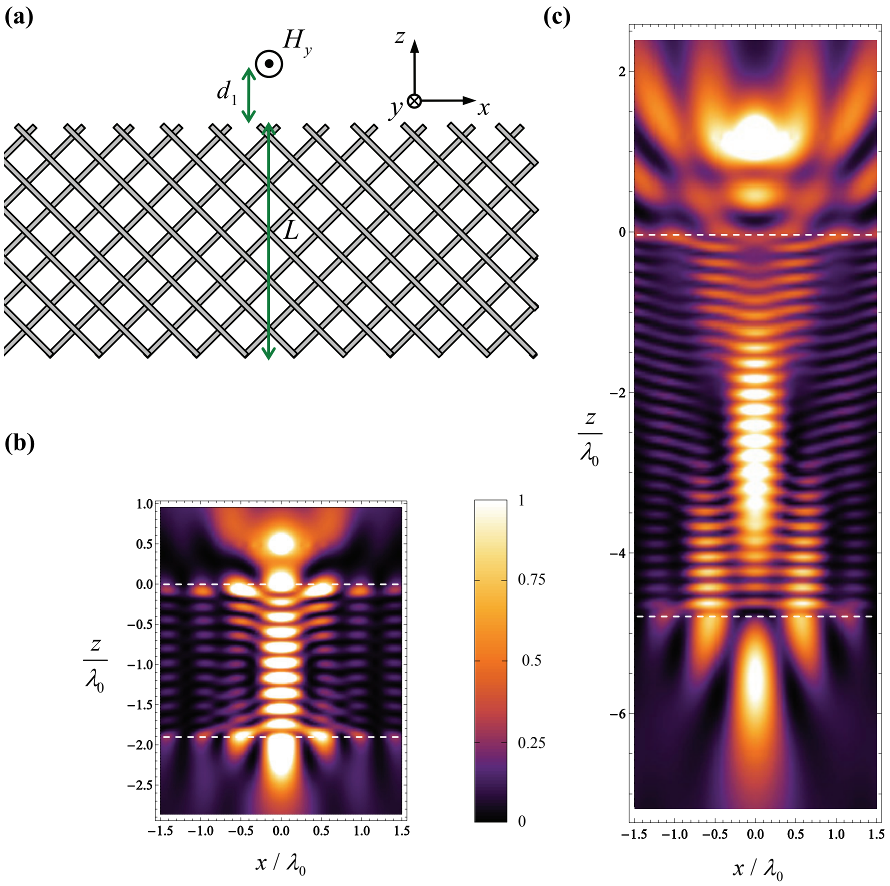

Fig. 3.19. (a): Geometry of the problem: a magnetic line source is placed at a distance d_1 above the crossed wires lens. (b) and (c): Squared (normalized) amplitude of the magnetic field $|\mathbf{H}|^2$. The frequency of operation is $\omega a/c = 0.6$, the radius of the wires is $r_w = 0.05a$, the permittivity of the host is $\varepsilon_h = 1$, and the source is located at a distance $d_1 = 0.25L$ from the front interface of the slab. The white dashed lines represent the interfaces of the slab. (b) $L = 20a$; (c) $L = 50a$.

In Fig. 3.19b-c the density plots of $|\mathbf{H}|^2$ are depicted in the *xoz* plane for the configuration illustrated in Fig. 3.19a with $d_1 = 0.25L$. In both figures it is clearly seen an intense partial focus of the magnetic field inside the crossed wires lens, and also behind the lens. Hence, these results confirm the findings of Sec. III.3.4.1, and prove that a flat slab of nonconnected crossed wires can indeed redirect the electromagnetic radiation of a *p*-polarized line source (such that the electric field is in the plane of the wires) to a narrow spot at the focal plane.

It is seen in Fig. 3.19b that for a slab with thickness $L = 20a$ the focal point behind the lens spreads somewhat along the *z* direction, and partially overlaps the back interface of the slab. In order to achieve a focal point clearly detached from the interface, we can use a slab with larger thickness L, as shown in Fig. 3.19c, for a lens with $L = 50a$. This can be understood by noting that for a fixed frequency of operation, the characteristic dimension of the system as compared to the wavelength increases with L, and thus the laws of geometrical optics and the ray-tracing analysis become more accurate (or in other words, the effects of wave diffraction are mitigated). Furthermore, it is noticeable in Fig. 3.19c that the focal region is somewhat elongated, consistent with the ray-tracing analysis of Fig. 3.18b, as a consequence of the fact that the angle of refraction θ_t inside the lens is angle-dependent, as already discussed in Sec. III.3.4.1.

In the region above the slab of crossed wires (where the source is located) some effects of reflections can be detected. Indeed, as already mentioned in Sec. III.3.3, there is some mismatch between the impedances of the structured material and free space, because the effective impedance of the metamaterial is relatively low [15].

The half-power beamwidth (HPBW) measured at the focal plane for the example reported in Fig. 3.19c is $0.4\lambda_0$, similar to the conventional diffraction limit value ($\lambda_0 / 2$) that is obtained with planar lens formed by anisotropic indefinite materials such as the proposed in the previous section formed by helical shaped wires.

The results described above were obtained using the analytical model [Eq. (3.23)], and assume that the metamaterial slab is infinitely extended along the *x* and *y* directions. In order to confirm these homogenization results and also the ray-tracing diagram (Fig. 3.18b), we used a homemade Method of Moments (MoM) code to numerically simulate the focusing properties of a finite width metamaterial slab illuminated by a magnetic line source. The MoM code takes into account all the fine details of the microstructure of the artificial material. In the MoM simulation the structured material slab is periodic along the *y* direction, and finite along the *x* direction with width *W*. It is assumed that each plane of wires (parallel to *xoz* plane) is formed by 100 wires, so that the width of the slab is approximately $W = 100a\sqrt{2}$.

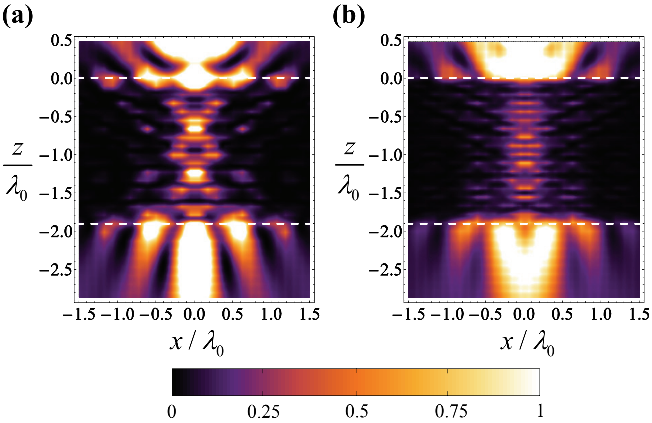

Fig. 3.20. Normalized $|\mathbf{H}|^2$ (a) and $|\mathbf{E}|^2$ (b) for an array of crossed wires with thickness $L = 20a$, radius of the wires $r_w = 0.05a$, and permittivity of the host $\varepsilon_h = 1$. The magnetic line source is placed at distance $d_1 = 0.25L$ from the front interface of the slab. The frequency of operation is $\omega a / c = 0.6$.

The spatial maps of the normalized squared amplitude of the magnetic and electric fields calculated with the MoM are shown in Fig. 3.20. An intense partial focus of the magnetic field (Fig. 3.20a) on the far side of the slab relative to the line source is clearly seen, confirming the homogenization results and further demonstrating that this structure works, indeed, as a planar focusing device. Contrary to what happens with the intensity of the magnetic field, the intensity of the electric field (Fig. 3.20b) inside the metamaterial slab is significantly weaker than in the free-space regions [15]. Indeed, as mentioned before, the crossed wire mesh is a low impedance material. Due to this property, which implies some impedance mismatch with free-space, some reflections can be detected in the region above the first interface, consistent with the results of the homogenization model.

III.3.4.3 Imaging a realistic electric current source – numerical and experimental results

In the previous subsection, we have numerically demonstrated the focusing of the electromagnetic radiation by the crossed wires metamaterial, using both an analytical model based on homogenization theory as well as using a homemade method of Moments (MoM) code, assuming that the metamaterial lens is illuminated by a magnetic line source (infinitely extended along *y*-direction). Following this, it would be very interesting to verify such results through an experiment. However, an obstacle arises at this point. Specifically, a truly magnetic line source is an unrealistic excitation. Hence, here we study the possibility of using a more realistic electric current source as the excitation of the structured lens. Such possibility is numerically investigated using CST Microwave Studio [29], and then experimentally verified using a fabricated prototype of the crossed wires lens.

To begin with, we used the commercial software [29] to simulate the electromagnetic response of a finite width crossed wires slab illuminated by an array of dipole-type antennas with length $l \simeq \lambda_0 / 4$. The dipoles are modeled in CST Microwave Studio through the excitation of two $\lambda_0 / 8$ metallic wires by a discrete port. The antennas are parallel to the *xoz* plane and the array period along y is equal to the lattice constant of the material a. Such excitation creates an electric field distribution that is mainly confined to the *xoz* plane, which is the condition required for the proper operation of the lens. The structured material is periodic along the y direction, and finite along the x direction with width $W \simeq 80\sqrt{2}a$. The cylindrical metallic wires of the original structure (Fig. 3.14) are replaced by metallic strips with width $w_s = \pi r_w$, and the metallic components (wires and dipole-type antennas) are assumed to be made of copper ($\sigma = 5.8 \times 10^7$ S/m).

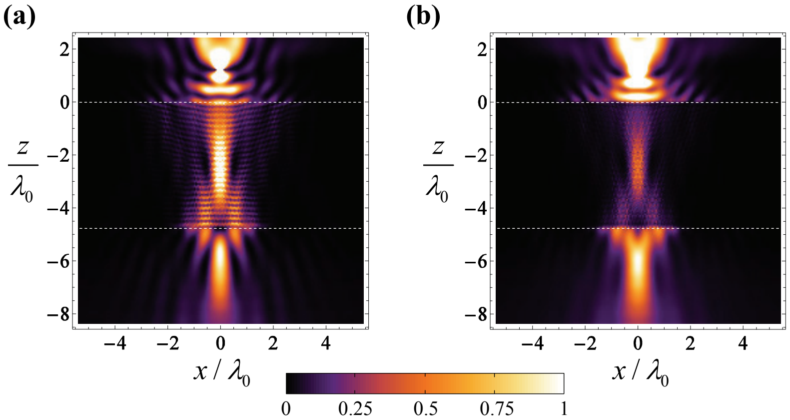

Fig. 3.21. (a) Normalized squared amplitude of the normal y component of the magnetic field, and (b) normalized squared amplitude of the in-plane component of the electric field, obtained with CST Microwave Studio [29]. The frequency of operation is $\omega a / c = 0.6$, the width of the metallic strips is $w_s = \pi a / 20$, the permittivity of the host is $\varepsilon_h = 1$, and the thickness of the slab is $L = 50a$. The source (array of dipole-type antennas) is located at a distance $d_1 = 0.25L$ above the lens, and each dipole has a length $l \simeq \lambda_0 / 4$. The white dashed lines represent the interfaces of the slab.

The simulation results, shown in Fig. 3.21, confirm that the crossed wires slab enables the focusing of the electromagnetic radiation created by the array of electric sources, extending the results of Sec. III.3.4.2. It is clearly seen, both in the distribution of the normal component of the magnetic field (Fig. 3.21a) as well as in the in-plane (*xoz*) component of the electric field (Fig. 3.21b), an intense partial focus both behind the lens and also inside the lens. Moreover, in agreement with the results of Sec. III.3.4.2, it is also noticeable in Fig. 3.21 that the crossed wire mesh is a low impedance material [15, J.4], since the intensity of the electric field inside the structured lens is weaker than outside, whereas the intensity of the magnetic field is of the same order. As a result, there is a slight impedance mismatch with free-space, perceptible in the reflections observed in the region above the first interface of the lens.

So, we have shown that, similar to what happens with a magnetic line source excitation, the crossed wires lens also works as a planar focusing device for an array of dipoles parallel to the planes of wires. Thus, the main obstacle to the fabrication of the prototype of the crossed wires lens that was directly related to the excitation source is surpassed, since now we can use a realistic electric current source to demonstrate the partial focusing of the electromagnetic radiation by the proposed lens. However, at this point there is still a detail hindering the fabrication of the prototype and that concerns to the infinite size of the structure along the y direction. Obviously, this is an undesired characteristic in practical terms. Hence, in order to circumvent this drawback, next we analyze the electromagnetic response of a simplified setup (Fig. 3.22a). Specifically, instead of infinitely periodic along the y direction, the crossed wire lens is formed by only four planes of wires along such direction of space. In order to ensure that the electromagnetic fields radiated by the dipole are strongly attached to the structure and thus interact with the crossed wires lens, we use a dielectric substrate with high permittivity ($\varepsilon_h = 10.2$). Moreover, in this case the excitation is a single balanced dipole-type antenna rather than an array of ideal dipoles as before. It is important to underline that now the geometry of the dipole-type antenna and of the feeding point are modelled exactly (see Fig. 3.22a), unlike previously where the simulated dipoles consisted simply in two very small metallic wires excited by a discrete port.

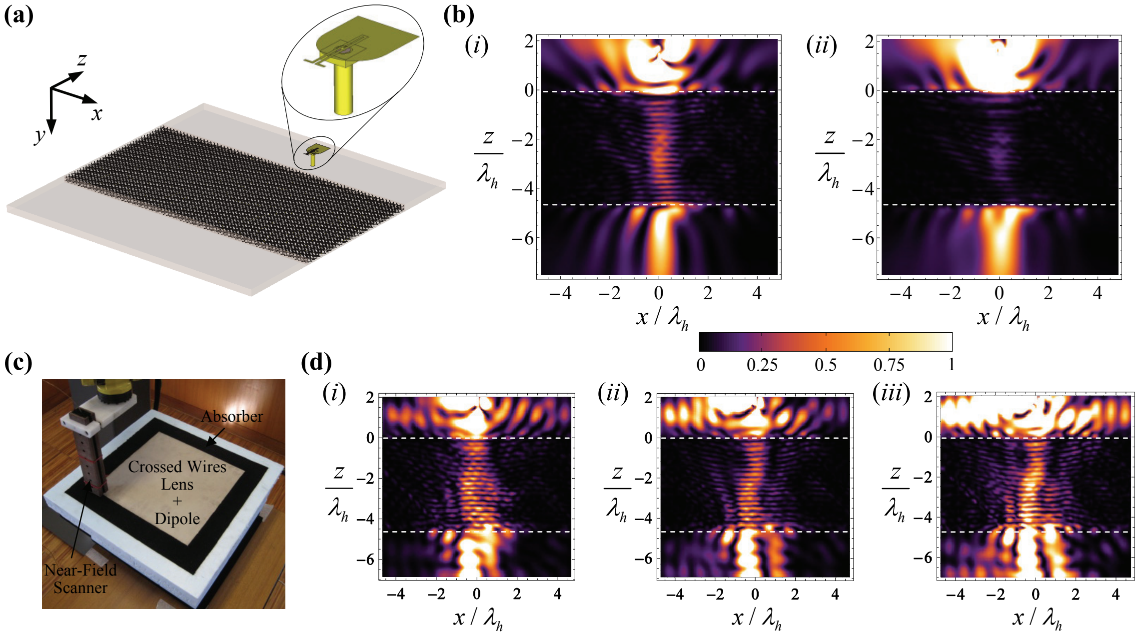

Fig. 3.22. (a) Crossed wires lens as simulated in CST Microwave Studio [29]. The metamaterial lens is formed by only four planes of wires along the y direction, and is excited by a balanced dipole-type antenna illustrated in detail in the zoom-in view. (b) (*i*) Normalized squared amplitude of the normal y component of the magnetic field and (*ii*) normalized squared amplitude of the in-plane component of the electric field, obtained with CST Microwave Studio [29] (λ_h is the wavelength in the dielectric host). The scanning is performed 2 mm above the lens. The frequency of operation is $f = 3.53$ GHz, the width of the metallic strips is $w_s = \pi a / 20 \simeq 0.4$ mm, the permittivity of the host is $\varepsilon_h = 10.2$, and the thickness of the slab is $L = 50a = 127$ mm. The source is located at a distance $d_1 = 0.25L = 31.75$ mm above the lens, and the dipole has a length $l \simeq 7.08$ mm. The white dashed lines represent the interfaces of the slab. (c) Photo of the crossed wires lens prototype. (d) Experimental results of the normalized squared amplitude of the normal y component of the magnetic field for (*i*) $f = 3.47$ GHz; (*ii*) $f = 3.51$ GHz; (*iii*) $f = 3.53$ GHz. The remaining parameters are the same as in (b) as well as the plane of scanning.

The squared amplitude of the normal y component of the magnetic field and of the in-plane component of the electric field obtained from the commercial electromagnetic simulator [29] are represented in Fig. 3.22b. It is manifest from Fig. 3.22b that, despite the imperfect radiation profile of the dipole-type antenna and consistent with the results of Fig. 3.21, the electromagnetic fields are partially focused inside and outside the structured lens. It is worth noting that in this case the electromagnetic field distributions are not symmetric along the *x* direction. Of course, the non-ideal radiation of the source contributes in part to this lack of symmetry. However, the asymmetry visible inside the structured lens is essentially a consequence of the finite number of planes of wires, since can be verified (not shown here) that even using an ideal dipole source to excite this finite-height lens the asymmetry is revealed. In particular, the inner partial focus appears slightly tilted to the right in Fig. 3.22b as a consequence of the metallic wires of the upper plane being tilted by 45° relatively to *z* axis (see Fig. 3.16a(*ii*)).

Following the results of Fig. 3.22b, we have fabricated a prototype of the crossed wires lens using a layer by layer design and printed circuit techniques (Fig. 3.22c). The geometry of the fabricated structure is exactly the same as that modeled and simulated in CST Microwave Studio. The lens is formed by a stack of four printed circuit boards of thickness 1.27 mm and two printed circuit boards of thickness 0.635 mm of RT/DUROID 6010LM with dielectric constant $\varepsilon_h = 10.2$ and loss tangent $\tan\delta = 0.0023$. The metallic strips tilted by $\pm 45^\circ$ with respect to the *z* direction are printed in the four thicker boards. The metallic strips in adjacent boards are mutually orthogonal. The width of the metallic strips is $w_s = 0.4$ mm, the lattice constant is $a = 2 \times 1.27 = 2.54$ mm, and the thickness of the lens is $L = 50a = 127$ mm. On the other hand, the balanced dipole-type antenna is printed in the two thinner boards. These two boards are placed between each pair of thicker boards with perpendicular printed strips so that the printed dipole is located exactly at the center of the structure. In addition, microwave absorbers (Eccosorb LS 26) were positioned at the sides of the boards to avoid diffraction from the edges. Finally, the y component of the magnetic field was measured using a near-field scanner with a round shielded loop probe and a vector analyzer (R&S ZVB20).

The measured amplitude of $|\mathbf{H}|^2$ is depicted in Fig. 3.22d for three different frequencies around 3.5 GHz. One can see that, notwithstanding the non-ideal radiation of the balanced printed dipole, the crossed wires lens prototype enables the partial focusing of the electromagnetic radiation both inside and outside the lens. In particular, the experimental results are in reasonable agreement with the full-wave simulations results (Fig. 3.22b(*i*)). Similar to Fig. 3.22b(*i*), it is noticeable in the experimental results (Fig. 3.22d) an asymmetry of the magnetic field distributions inside the lens along the x direction. This fact is mainly a consequence of the finite number of boards of wires, as already explained above. Despite the obvious similarities, there are also some slight discrepancies between the experimental and numerical results. Such disagreements are related to fabrication imperfections, especially in the printed dipole antenna used as the source excitation. In fact, owing to its subwavelength dimensions and fabrication complexity, the printed dipole is extremely sensitive to perturbations, and hence, is likely to be the main responsible in the slight mismatch between the experimental and numerical results. This extreme sensitivity of the printed subwavelength dipole and its inherent narrow-band preclude the estimation of the bandwidth of operation of the fabricated lens. It should be underlined, however, that it is expected that the fabricated lens may operate over a wide frequency band, such as theoretically predicted in Refs. [15, J.4].

III.3.5. Boosting the Strength of Negative Refraction in the Crossed Wire Mesh

As explained in Sec. III.3.3, the emergence of negative refraction in the crossed wire mesh can be intuitively understood by noticing that the two sets of parallel wires behave as two different waveguides for the incoming wave, and that the transmission occurs mainly along the set of wires that is better coupled to the incoming electric field. Based on this simple physical interpretation of the mechanism behind the negative refraction in the crossed wire mesh, the following question arises naturally: "What happens to the negative refraction effect if the angle between the two sets of parallel wires is increased?" From our understanding of the physical mechanism, it is expected that the negative refraction effect is enhanced. In order to answer the question and check the correctness of our prediction, here we study in detail the electromagnetic response of configurations where the angle between the two arrays of parallel wires θ_0 is different from 90° (Fig. 3.23), namely $\theta_0 > 90^\circ$.

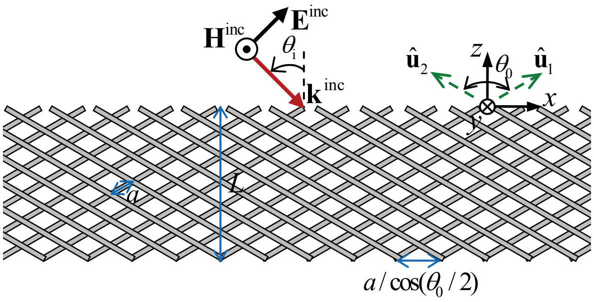

Fig. 3.23. Geometry of the crossed wires metamaterial with arbitrary angle between the two arrays of wires. One array of wires is oriented along the direction $\hat{\mathbf{u}}_1 = \sin(\theta_0/2)\hat{\mathbf{u}}_x + \cos(\theta_0/2)\hat{\mathbf{u}}_z$, whereas the other array is oriented along $\hat{\mathbf{u}}_2 = -\sin(\theta_0/2)\hat{\mathbf{u}}_x + \cos(\theta_0/2)\hat{\mathbf{u}}_z$. The distance between each of the adjacent sets of wires is $a/2$. The plane of incidence is the *xoz* plane and the incident wave is TM-*z* polarized.

Similar to the standard nonconnected crossed wire medium (Fig. 3.14), the dielectric function of the crossed wires configuration with arbitrary angle between the two sets of wires can be obtained using the nonlocal homogenization approach introduced in Ref. [25].

Following this approach, one can prove that, consistent with the conventional crossed wire mesh (Fig. 3.14), the dielectric function that characterizes the alternative crossed wire medium (Fig. 3.23) is given by Eq. (3.24), with $\hat{\mathbf{u}}_1 = \sin(\theta_0/2)\hat{\mathbf{u}}_x + \cos(\theta_0/2)\hat{\mathbf{u}}_z$ and $\hat{\mathbf{u}}_2 = -\sin(\theta_0/2)\hat{\mathbf{u}}_x + \cos(\theta_0/2)\hat{\mathbf{u}}_z$ in this case. The permittivity components ε_{11} and ε_{22} are given again by Eq. (3.25).

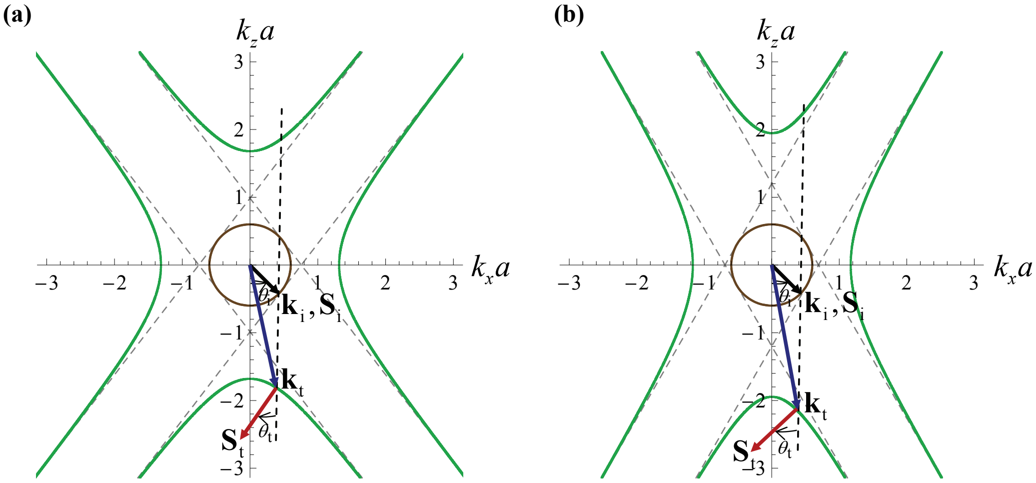

Fig. 3.24. Isofrequency contour of the fundamental plane wave mode supported by the crossed wire mesh (Fig. 3.23) for the normalized frequency $\omega a / c = 0.6$, $\varepsilon_h = 1$, $r_w = 0.05a$, and (a) $\theta_0 = 105^\circ$ (b) $\theta_0 = 120^\circ$ (green lines), as well as the isofrequency contour in the air region (brown circle). The gray dashed lines represent the asymptotes of the two hyperbolas. The transmitted wave vector $\mathbf{k}_t$ (blue arrow) is determined by the conservation of the tangential component of the wave vector k_x at the interface, whereas the Poynting vector $\mathbf{S}_t$ (red arrow) is normal to the isofrequency curves and is oriented towards increasing frequencies.

Consistent with the standard crossed wire medium formed by two orthogonal arrays of parallel wires, it can be shown that the dispersion characteristic of crossed wire configurations with $\theta_0 \neq 90^\circ$ (Fig. 3.23) for propagation in the *xoz* plane is equivalent to a third degree polynomial in the variable k_z^2. Moreover, the isofrequency contours of the fundamental plane wave mode correspond again to two perpendicular hyperbolas (Fig. 3.24). However, as one can see by comparing Fig. 3.15 and Fig. 3.24, the shape of the two hyperbolas is progressively modified by gradually increasing the angle θ_0 between the two sets of parallel wires. This reshaping of the hyperbolic isofrequency contours is forced by the asymptotes of the hyperbolas that, as already discussed in Sec. III.3.3, are perpendicular to the direction of the wires of both arrays, i.e., normal to $\hat{\mathbf{u}}_1$ and $\hat{\mathbf{u}}_2$. In particular, it is seen from Fig. 3.24 that by increasing the angle θ_0 between the two sets of wires, the aperture of the two branches of the hyperbola related with the desired propagation direction (*z* direction; see Fig. 3.23) progressively decreases, which means that the Poynting vector is more negatively refracted since it has to be normal to the hyperbolic curve (see Fig. 3.24). Hence, these results predict that the strength of the negative refraction may be, indeed, boosted by increasing the angle θ_0 between the two arrays of wires.

In order to clarify such possibility, we have calculated the angle of transmission (or refraction) θ_{t} for the energy flow (determined by the Poynting vector) as a function of the angle of incidence θ_{i} of plane waves incident onto crossed wires slabs with different values of θ_0 (see inset of Fig. 3.25a), using the relation $v_g = \nabla_k \omega(\mathbf{k})$. One can see from Fig. 3.25a that the angle of transmission θ_{t} for the energy flow becomes increasingly negative as the angle θ_0 between the two sets of wires is increased. Hence, these results are in agreement with the isofrequency contours of Fig. 3.24, and confirm that by increasing θ_0 it is possible to boost the strength of the negative refraction in the crossed wire mesh.

To further confirm these homogenization results, we used the full wave electromagnetic simulator CST Microwave Studio [29] to calculate the transmission coefficient *t* of crossed wire mesh configurations with different angles θ_0 under plane wave incidence (see Fig. 3.23). In addition, we have also calculated the transmission coefficient *t* using the nonlocal homogenization theory, i.e., solving a system of equations similar to Eq. (3.27). The results obtained using the two different methods are shown in Fig. 3.25b.

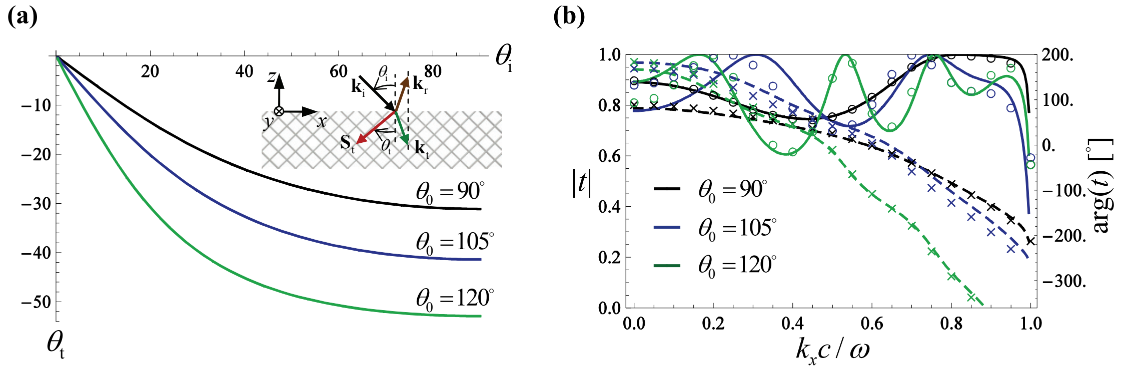

Fig. 3.25. (a) Angle of transmission of the energy flow (Poynting vector) as a function of the angle of incidence for different angles θ_0 between the two arrays of wires. The frequency of operation is $\omega a / c = 0.6$, the radius of the wires is $r_w = 0.05a$, and the host permittivity is $\varepsilon_h = 1$. The inset illustrates the geometry of the problem showing the incident, reflected and transmitted (or refracted) waves. (b) Amplitude and phase of the transmission coefficient as a function of the normalized k_x component of the wave vector for different angles θ_0 between the two arrays of wires. The frequency of operation is $\omega a / c = 0.6$, the radius of the wires is $r_w = 0.05a$, the host permittivity is $\varepsilon_h = 1$, and the thickness of the slab is $L = 25a$. The solid curves (solid curves: amplitude, solid dashed curves: phase) correspond to the nonlocal homogenization results, whereas the discrete symbols (circles: amplitude, crosses: phase) correspond to full wave results [29].

Firstly, it should be stressed the very good agreement between the nonlocal homogenization results and the full wave results, demonstrating the accuracy of the nonlocal homogenization model. Moreover, Fig. 3.25b shows that the phase of the transmission coefficient decreases with k_x, which based on the criterion introduced in Ref. [15] indicates unequivocally the emergence of negative refraction. In particular, one can see that the absolute value of the slope of the curves of the phase of t increases by increasing the angle θ_0 between the two arrays of parallel wires, which is a clear proof that, in fact, by increasing θ_0 the negative refraction effect is enhanced. On the other hand, it is seen from Fig. 3.25b that the amplitude of the transmission coefficient deteriorates slightly for some spatial harmonics (or angles of incidence) with the increase of the angle θ_0 between the two arrays of parallel wires. Despite that inconvenience, its amplitude remains at an acceptable level.

In order to provide a conclusive evidence for the enhanced negative refraction in the crossed wire mesh with $\theta_0 > 90^\circ$, we used the nonlocal homogenization theory to analyze the refraction of a beam with a Gaussian profile at the interfaces of infinite width metamaterial configurations with $\theta_0 > 90^\circ$. The approach used is the same of Sec. III.2.4.3 and Sec. III.3.3 that relies on Fourier theory.

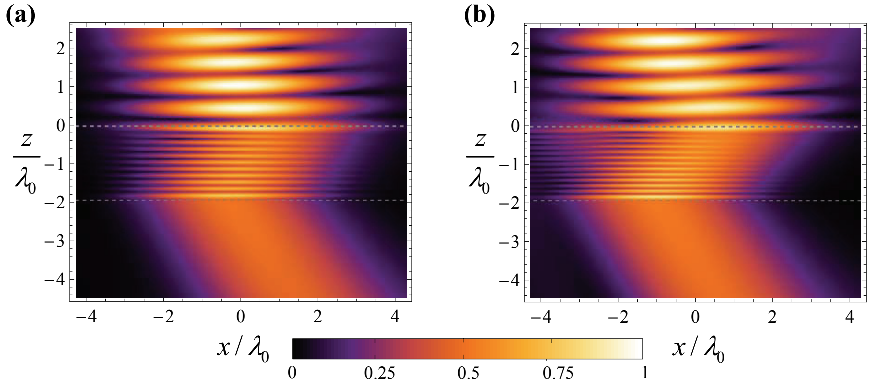

Fig. 3.26. Normalized amplitude of the magnetic field $|H_y|$ inside and outside two crossed wire mesh configurations with $\theta_0 > 90^\circ$ calculated using the nonlocal homogenization approach. (a) $\theta_0 = 105^\circ$; (b) $\theta_0 = 120^\circ$. The excitation is a Gaussian beam with transverse magnetic polarization characterized by $2w_0 = 4\lambda_0$ and an incident angle of $\theta_i = 33^\circ$. The metamaterial slab is periodic along the x and y directions. The gray dashed lines represent the interfaces of the slab. The frequency of operation is $\omega a / c = 0.6$, the radius of the wires is $r_w = 0.05a$, the permittivity of the host is $\varepsilon_h = 1$, and the thickness of the slab is $L = 20a$.

Comparing Fig. 3.26 and Fig. 3.17b, it can be seen that the absolute value of the spatial lateral shift Δ suffered by the Gaussian beam at the interfaces of the slab is progressively increased by increasing θ_0. Hence, based on these results we come to the conclusion that, in fact, it is possible to boost the strength of the negative refraction by increasing the angle θ_0 between the two arrays of parallel wires. On the other hand, and also consistent with the transmission profiles of Fig. 3.25b, one can notice that the level of reflections at the first interface of the slab increases slightly for larger values of θ_0.

Following this achievement, next we investigate the focusing properties of the crossed wires lens configurations with angles between the two arrays of parallel wires $\theta_0 > 90^\circ$. Taking advantage of the enhanced negative refraction effect, it is expected that these alternative configurations may provide further degrees of freedom in the design of the lenses. In order to analyze the focusing possibilities, we consider again that the structured lens is illuminated by a magnetic line source infinitely extended along the *y* direction (Fig. 3.27a). Then, using the nonlocal homogenization theory together with Fourier theory (see Sec. III.2.5.2), we have calculated the magnetic field distribution inside and outside a lens infinitely periodic along the *x* and *y* direction. In addition, in order to verify the analytical results we have also used a homemade MoM code to compute the magnetic field reflected and refracted by a finite-width lens ($W = 80a / \cos(\theta_0 / 2)$).

The spatial maps of the squared normalized amplitude of the magnetic fields calculated using both methods are shown in Fig. 3.27b-c. In all figures it is seen an intense elongated (or partial) focus of the magnetic field inside and outside the lens, demonstrating in this manner that the modified crossed wire lenses with $\theta_0 > 90^\circ$ enable the partial focusing of *p*-polarized electromagnetic radiation. At the same time, it is important to stress the good agreement between the analytical results (Fig. 3.27b(*i*)) and the numerical results (Fig. 3.27b(*ii*)), further confirming the good accuracy of the nonlocal homogenization model.

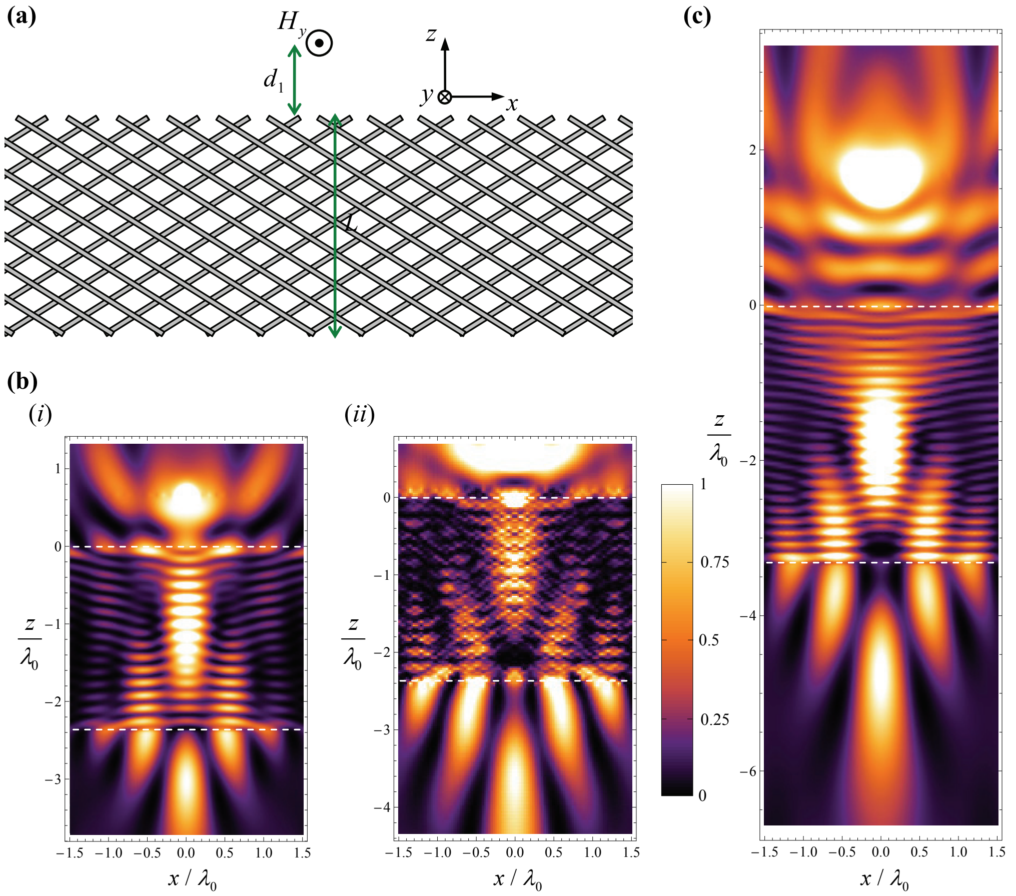

Fig. 3.27. Geometry of the problem: a magnetic line source is placed at a distance d_1 above crossed wires lens configurations with angles between the two arrays of wires $\theta_0 > 90^\circ$. (b) and (c) Squared (normalized) amplitude of the magnetic field $|\mathbf{H}|^2$. The frequency of operation is $\omega a / c = 0.6$, the radius of the wires is $r_w = 0.05a$, and the permittivity of the host is $\varepsilon_h = 1$. (b) Nonlocal homogenization result (*i*) and MoM result (*ii*) for a configuration with $L = 25a$, $d_1 = 0.275L$ and $\theta_0 = 105^\circ$. (c) Nonlocal homogenization result for a configuration with $L = 35a$, $d_1 = 0.5L$ and $\theta_0 = 115^\circ$.

Moreover, by comparing Fig. 3.27b(*i*) and Fig. 3.19b-c, one can recognize one of the possibilities opened by these alternative lens configurations with obtuse angles θ_0. Specifically, it may be possible to reduce considerably the thickness of the metamaterial lens and still obtain partial focusing of the electromagnetic radiation. Indeed, whereas using a configuration with orthogonal arrays of wires the lens has to have a thickness of the order of $L \simeq 5\lambda_0$ to achieve a focal point detached from the interface (Fig. 3.19b-c) of a source located at a distance of about $d_1 = L/4$, the thickness of the lens can be reduced to approximately half using a configuration with an angle between the two arrays of wires of $\theta_0 = 105^\circ$ (Fig. 3.27b). Conversely, it can be seen by comparison of Fig. 3.27c with Fig. 3.19c that it is also possible to move farther away the source from the input interface and still obtain partial focusing of the radiation using a lens with $\theta_0 > 90^\circ$ rather than $\theta_0 = 90^\circ$. Particularly, a structured lens with $\theta_0 = 115^\circ$ and thickness $L \simeq 3.3\lambda_0$ permits the partial focusing of the electromagnetic radiation of a source located at a distance $d_1 = L/2$ of its input interface.

In summary, we have demonstrated that by increasing the angle between the two sets of parallel wires it is possible to boost the strength of the negative refraction effect, and in this manner obtain partial focusing with a significantly thinner metamaterial slab and/or increase the focal depth of the lens.

III.3.6. Concluding Remarks

In Sec. III.3, we have numerically as well as experimentally demonstrated partial focusing of electromagnetic radiation taking advantage of the all-angle broadband negative refraction effect that emerges at the interfaces of a spatially dispersive material formed by nonconnected crossed wires. Despite some similarities of the reported focusing effect and the results achievable using an indefinite anisotropic material (e.g., the uniaxial ENG material formed by helical shaped wires studied in Sec. III.2), its physical origin is completely distinct. In the crossed wire mesh the hyperbolic isofrequency contours are rooted in the existence of two propagation channels, whereas in indefinite media it is related to the sign of the principal elements of the permittivity and/or permeability tensors.

In addition, it was shown that the negative refraction in the crossed wires lens may be considerable enhanced by simply increasing the angle between the two arrays of wires (i.e., the two propagation channels) and, as a result, it may be possible to obtain partial focusing of the electromagnetic radiation using significantly thinner structured lenses and/or increase the focal depth of the lens.

References

[1] V. G. Veselago, "The Electrodynamics of Substances with Simultaneously Negative Values of ε and μ", *Sov. Phys. Usp.*, vol. 10, p. 509, 1968.

[2] J. B. Pendry, "Negative Refraction Makes a Perfect Lens", *Phys. Rev. Lett.*, vol. 85, p. 3966, 2000.

[3] D. R. Smith, W. J. Padilla, D. C. Vier, S. C. Nemat-Nasser, S. Schultz, "Composite Medium with Simultaneously Negative Permeability and Permittivity", *Phys. Rev. Lett.*, vol. 84, p. 4184, 2000.

[4] R. A. Shelby, D. R. Smith, S. Schultz, "Experimental Verification of a Negative Index of Refraction", *Science*, vol. 292, p. 77, 2001.

[5] J. Valentine, S. Zhang, T. Zentgraf, E. Ulin-Avila, D. A. Genov, G. Bartal, X. Zhang, "Three-dimensional optical metamaterials with a negative refractive index", *Nature*, vol. 455, p. 376, 2008.

[6] M. Notomi, "Theory of light propagation in strongly modulated photonic crystals: Refractionlike behavior in the vicinity of the photonic band gap", *Phys. Rev. B*, vol. 62, p. 10696, 2000.

[7] E. Cubukcu, K. Aydin, E. Ozbay, S. Foteinopoulou, and C. M. Soukoulis, "Electromagnetic waves: Negative refraction by photonic crystals", *Nature (London)*, vol. 423, p. 604, 2003.

[8] D. R. Smith and D. Schurig, "Electromagnetic Wave Propagation in Media with Indefinite Permitivitty and Permeability Tensors", *Phys. Rev. Lett.*, vol. 90, p. 077405, 2003.

[9] D. R. Smith, D. Schurig, J. J. Mock, P. Kolinko, and P. Rye, “Partial focusing of radiation by a slab of indefinite media”, *Appl. Phys. Lett.*, vol. 84, p. 2244, 2004.

[10] X. Fan, G. P. Wang, J. C. W. Lee, C. T. Chan, “All-Angle Broadband Negative Refraction of Metal Waveguide Arrays in the Visible Range: Theoretical Analysis and Numerical Demonstration”, *Phys. Rev. Lett.*, vol. 97, p. 073901, 2006.

[11] A. J. Hoffman, L. Alekseyev, S. S. Howard, K. J. Franz, D. Wasserman, V. A. Podolskiy, E. E. Narimanov, D. L. Sivco, G. Gmachl, “Negative refraction in semiconductor metamaterials”, *Nature Mater.*, vol. 6, p. 946, 2007.

[12] A. Fang, T. Koschny, C. M. Soukoulis, “Optical anisotropic metamaterials: Negative refraction and focusing”, *Phys. Rev. B*, vol. 79, p. 245127, 2009.

[13] Y. Liu, G. Bartal, X. Zhang, “All-angle negative refraction and imaging in a bulk medium made of metallic nanowires in the visible region”, *Opt. Express*, vol. 16, p. 15439, 2008.

[14] J. Yao, Z. Liu, Y. Liu, Y. Wang, C. Sun, G. Bartal, A. M. Stacy, X. Zhang, “Optical Negative Refraction in Bulk Metamaterials of Nanowires”, *Science*, vol. 321, p. 930, 2008.

[15] M. G. Silveirinha, “Broadband negative refraction with a crossed wire mesh”, *Phys. Rev. B*,vol. 79, p. 153109, 2009.

[16] J. Demetriadou and J. B. Pendry, “Taming spatial dispersion in wire metamaterial”, *J. Phys.: Condens. Matter*, vol. 20, p. 295222, 2008.

[17] S. I. Maslovski and M. G. Silveirinha, “Nonlocal permittivity from a quasistatic model for a class of wire media”, *Phys. Rev. B*, vol. 80, p. 245101, 2009.

[18] O. Luukkonen, M. G. Silveirinha, A. B. Yakovlev, C. R. Simovski, I. S. Nefedov, and S. A. Tretyakov, “Effects of Spatial Dispersion on Reflection From Mushroom-Type Artificial Impedance Surfaces”, *IEEE Trans. Microwave Theory Tech.*, vol. 57, p. 2692, 2009.

[19] O. Luukkonen, M. G. Silveirinha, A. B. Yakovlev, C. R. Simovski, I. S. Nefedov, and S. A. Tretyakov, “Characterization of Surface-Wave and Leaky-Wave Propagation on Wire-Medium Slabs and Mushroom Structures Based on Local and Nonlocal Homogenization Models”, *IEEE Trans. Microwave Theory Tech.*, vol. 57, p. 2700, 2009.

[20] O. Luukkonen, P. Alitalo, F. Costa, C. Simovski, A. Monorchio, and S. Tretyakov, “Experimental verification of the suppression of spatial dispersion in artificial plasma”, *Appl. Phys. Lett.*, vol. 96, p. 081501, 2010.

[21] M. J. Lockyear, A. P. Hibbins, and J. R. Sambles, “Microwave Surface-Plasmon-Like Modes on Thin Metamaterials”, *Phys. Rev. Lett.*, vol. 102, p. 073901, 2009.

[22] M. G. Silveirinha, A. B. Yakovlev, “Negative refraction by a uniaxial wire medium with suppressed spatial dispersion”, *Phys. Rev. B*, vol. 81, p. 233105, 2010.

[23] C. S. R. Kaipa, A. B. Yakovlev, M. G. Silveirinha, “Characterization of negative refraction with multilayered mushroom-type metamaterials at microwaves”, *J. Appl. Phys.*, vol. 109, p. 044901, 2011.

[24] M. G. Silveirinha, “Design of Linear-to-Circular Polarization Transformers Made of Long Densely Packed Metallic Helices”, *IEEE Trans. Antennas Propag.*, vol. 56, p. 390, 2008.

[25] M. G. Silveirinha, “Metamaterial homogenization approach with application to the characterization of microstructured composites with negative parameters”, *Phys. Rev. B*, vol. 75, p. 115104, 2007.

[26] V. Agranovich and V. Ginzburg, *Spatial Dispersion in Crystal Optics and the Theory of Excitons*, Wiley-Interscience, New York, 1966.

[27] M. G. Silveirinha, C. A. Fernandes, “A Hybrid Method for the Efficient Calculation of the Band Structure of 3-D Metallic Crystals”, *IEEE Trans. Microwave Theory Tech.*, vol. 52, p. 889, 2004.

[28] S. Tretyakov, *Analytical Modeling in Applied Electromagnetics*, Norwood, MA: Artech House, 2003.

[29] CST Microwave Studio 2010 (http://www.cst.com).

[30] M. G. Silveirinha, “Additional Boundary Condition for the Wire Medium”, *IEEE Trans. Antennas Propag.*, vol. 54, p. 1766, 2006.

[31] M. G. Silveirinha, C. A. Fernandes, J. R. Costa, “Additional boundary condition for a wire medium connected to a metallic surface”, *New J. Phys.*, vol. 10, p. 053011, 2008.

[32] M. Born, E. Wolf, *Principles of Optics*, 6th ed., Pergamon Press, Oxford, 1993.

[33] M. G. Silveirinha, C. A. Fernandes, “Homogenization of 3D- Connected and Non-Connected Wire Metamaterials”, *IEEE Trans. Microwave Theory Tech.*, vol. 53, p. 1418, 2005.

[34] C. R. Simovski, P. A. Belov, “Low-frequency spatial dispersion wire media”, *Phys. Rev. E*, vol. 70, p. 046616, 2004.

[35] I. S. Nefedov, A. J. Viitanen, S. A. Tretyakov, “Electromagnetic wave refraction at an interface of a double wire medium”, *Phys. Rev. B*, vol. 72, p. 245113, 2005.

[36] M. G. Silveirinha, C. A. Fernandes, “Nonresonant structured material with extreme effective parameters”, *Phys. Rev. B*, vol. 78, p. 033108, 2008.

[37] M. G. Silveirinha, “Additional Boundary Conditions for Nonconnected Wire Media”, *New J. Phys.*, vol. 11, p. 113016, 2009.

IV. BROADBAND AND ULTRA-SUBWAVELENGTH WAVEGUIDING WITH A CROSSED WIRE MESH

IV.1. Introduction

The development of methods for confining and guiding the electromagnetic radiation has been instrumental to the progress of telecommunication systems and beyond. Waveguides and optical fibers are some examples of technologies developed for this purpose, and are nowadays crucial instruments for guiding electromagnetic waves. However, despite all the remarkable guiding properties of these structures, they have a fundamental constraint: the transversal dimension of a common hollow-pipe waveguide [1] as well as the diameter of an optical fiber [2-3] must be at least half of the wavelength inside the structure $\lambda_0 / 2n$ (λ_0 is the wavelength in free space and n is the refractive index of the dielectric material). Such physical limitation is simply a consequence of the well-known phenomenon of wave diffraction and represents a serious barrier to the miniaturization of several devices.

In the last few years, however, stimulated by the advent of nanotechnology, scientists have been working on novel mechanisms that may allow confining and guiding electromagnetic radiation in small volumes far beyond the diffraction limit. Perhaps the most effective approach is based on coupling the electromagnetic radiation to the collective oscillations of free electrons supported by metal-dielectric interfaces, forming the so-called surface plasmon polaritons (SPPs) [4-7]. Since this is a surface phenomenon, the degree of field concentration is not restricted by diffraction as in conventional waveguides and optical fibers. Actually, the field confinement achieved with SPPs is only dictated by the permittivity contrast between metal and dielectric, and by metallic losses. In particular, the SPP is strongly attached to the metal surface at optical frequencies where the dielectric constant of metals is predominantly real and negative (Fig. 4.1a) and thus contrasts with the positive permittivity of dielectrics. At these frequencies, the field confinement can be, indeed, deeply subwavelength (Fig. 4.1b)[1] - about two orders of magnitude smaller than the wavelength of the light in air (on the order of 10 nm). Such possibility of field localization on the nanoscale has triggered tremendous interest to this subdiscipline of photonics called plasmonics, owing to its promising applications in integrated optical circuits [6-11], sensing [10, 12], nanoscopy [7, 12], solar cells [6, 12], and even cancer therapy [9, 12].

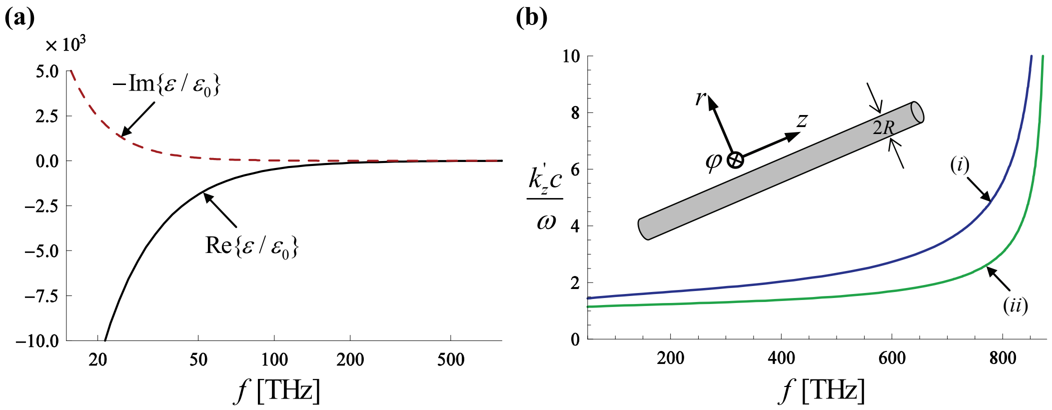

Fig. 4.1. (a) The real (black solid line) and imaginary (red dashed line) parts of the complex relative permittivity ($\varepsilon_r = \varepsilon_r^{'} - j\varepsilon_r^{''}$) of Ag as a function of the frequency calculated with the Drude model[2]. (b) Dispersion relation of SPPs on lossy Ag cylindrical wires of different radii R : (*i*) $R = 15$ nm ; (*ii*) $R = 30$ nm . These results were calculated using Eq. (7) of [14].

---

[1] It should be noted that the degree of field confinement is directly related to the value of $k_z^{'} c / \omega$, since the decay length into the dielectric material is given by $l_r = 1 / k_r^{''}$, with $k_r = (\omega / c)\sqrt{1 - (k_z c / \omega)^2}$.

[2] It was assumed that Ag follows the Drude dispersion model $\varepsilon_m = \varepsilon_\infty - \omega_p^2 / (\omega(\omega - j\Gamma))$, with $\varepsilon_\infty = 5$, $\omega_p / 2\pi = 2175$ THz , and $\Gamma / \omega_p = 0.002$, consistent with Ref. [13].

In contrast with optical frequencies, the prospects for low-frequency SPPs (i.e., far-infrared, terahertz, and microwave frequencies) are not so high. This fact is simply a consequence of the frequency dispersion of the permittivity of the metals (given by the Drude model [15]). Specifically, as we move from the optical to the microwave regime, both the real and imaginary parts of the metal's permittivity become huge (Fig. 4.1a), which means that metals lose the plasmonic-type response and begin to resemble perfect electric conductors (PECs), leading to weakly bounded SPPs (sometimes called Zenneck waves [16] or Sommerfeld waves [17] if the surface is cylindrical). Therefore, the electromagnetic fields are now extended over distances of several wavelengths into the dielectric region and, consequently, SPPs are no longer useful for compact waveguiding. Hence, alternative approaches are needed to achieve subwavelength confinement and guiding at microwave and terahertz frequencies.

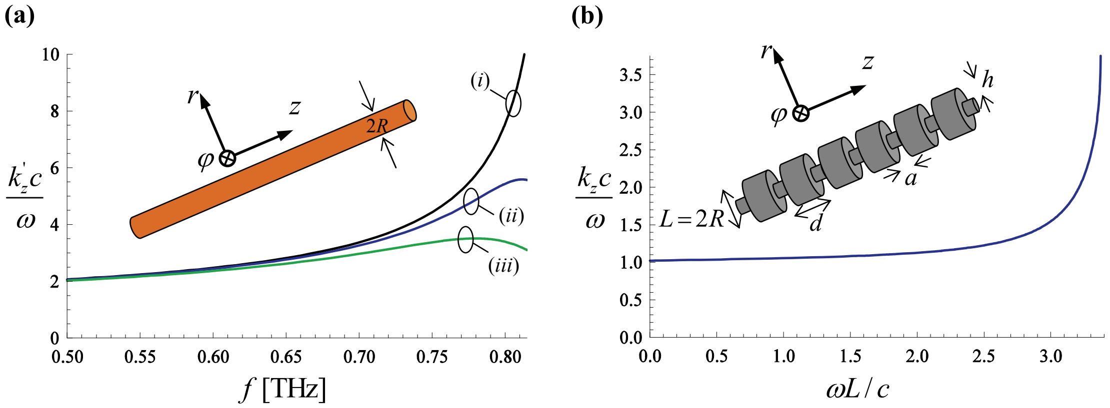

Fig. 4.2. (a) Real part of the normalized propagation constant k_z' of the SPP as a function of the frequency for a InSb [18] cylindrical wire in air with radius $R = 10\mu\text{m}$, calculated using Eq. (7) of [14]. The permittivity of the semiconductor at 225 K is described by the Drude model with $\varepsilon_\infty = 15.7$ and $\omega_p / 2\pi = 3.42$ THz. Black curve: $\Gamma / \omega_p = 0$; blue curve: $\Gamma / \omega_p = 0.02$; green curve: $\Gamma / \omega_p = 0.04$. (b) Normalized propagation constant k_z of the fundamental guided mode as a function of the frequency for a corrugated metallic wire [$a = 10\mu\text{m}$, $d = 50\mu\text{m}$, $R = 100\mu\text{m}$, $h = 65\mu\text{m}$ and $L = 2R$]. These results were calculated using Eq. (3) of [19].

One possibility at terahertz frequencies consists in using doped semiconductors (e.g., InSb) instead of metals, since these materials have a plasmonic-type response in the terahertz range [18]. However, the practical applications of this solution are greatly limited by the effects of losses (see Fig. 4.2a). Another possibility to mimic the role of SPPs at terahertz or even microwaves frequencies relies on structuring metal surfaces. In particular, several works have developed the concept of spoof SPPs [19-25] – geometry-controlled surface waves supported by metal surfaces tailored with subwavelength corrugations. However, these spoof SPPs topologies suffer from an important drawback: the characteristic size of the spoof plasmon waveguides is close to $\lambda/2$ (see Fig. 4.2b), which contrasts markedly with the ultra-subwavelength sizes of plasmonic wires at optical frequencies (see Fig. 4.1b). Moreover, even though these structured metal surfaces enable strong field confinement, all of them exhibit a narrowband electromagnetic response.

It would be highly desirable, however, that besides the strong field confinement, the subwavelength dimensions as well as the reasonably wide band of operation that characterize plasmonic waveguides at optical frequencies could also be achieved in the terahertz and microwave regimes. With this purpose in mind, we propose in this chapter a novel waveguiding solution based on strongly coupled grids of metallic wires that may enable overcoming the aforementioned physical limitations of the conventional spoof plasmon topologies, providing in this manner a truly broadband ultra-subwavelength waveguiding at microwave and terahertz frequencies.

IV.2. Resonantly Induced Surface Waves – Spoof Plasmons

Before introducing our subwavelength waveguiding proposal, it is helpful to briefly analyze the physics behind some relevant spoof plasmons topologies. In particular, we want to expose here in a simple form the physical origin of the narrowband response and physical size restriction intrinsic to all conventional spoof plasmons configurations.

To this end, let us first consider a periodically corrugated metallic wire (see inset of Fig. 4.2b). The possibility of exciting surface waves tightly bound to the structured surface of a corrugated metallic wire was hinted about sixty years ago [26], and explored in the last few years in some publications [19, 27]. In simple physical terms, the corrugated metallic wire can be seen as a set of coupled cavities (resonators). Each resonator is associated with a groove whose wavelength of resonance (for the configurations of Ref. [19-21, 27]) is about $\lambda \approx 4h$, where h is the depth of the groove (see inset of Fig. 4.2b). When the driving frequency is close to the resonance, the cavities are very strongly coupled by evanescent fields leaking out from them, and consequently an excitation can be propagated closely attached to the corrugated rod (spoof plasmon). Nevertheless, this phenomenon is resonant and extremely narrowband. Moreover, even at resonance, the overall diameter of the corrugated wire is roughly $2R \approx \lambda / 2$, as already anticipated in the previous section (see Fig. 4.2b).

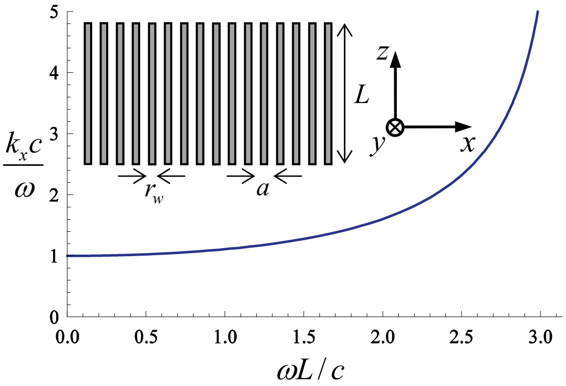

Fig. 4.3. Normalized propagation constant k_x of the fundamental guided mode as a function of the frequency for an array of metallic wires with lattice period $a = L/10$ and wire radius $r_w = 0.05a$.

Next, we consider an array of metallic wires with no corrugations, instead of a single continuous corrugated wire. Specifically, we examine a wire medium slab with thickness *L*, being all the wires perpendicular to the interfaces at $z=0$ and $z=L$ (inset of Fig. 4.3). The array period is *a*, and we are interested in propagation along the *x* direction with propagation constant k_x. Fig. 4.3 shows the dispersion of the fundamental guided mode (with field components E_x, E_z, and H_y), numerically calculated assuming perfectly electrical conducting (PEC) wires[3]. Similar to a periodically corrugated cylindrical wire (Fig. 4.2b), the array of metallic wires enables a strong field confinement, but only when the characteristic size of the waveguide is about $\lambda/2$. This is not really surprising since these strongly confined guided modes are rooted in the same physical mechanism in both cases. Indeed, in the wire medium slab each metallic wire may be regarded as a resonator (with resonant wavelength equal to $\lambda=2L$ for metals with high conductivity), and, similar to the corrugated wire, when $\lambda \approx 2L$ the resonators are strongly coupled by evanescent field tails. Interestingly, consistent with this intuitive explanation, it can be proven [28] that the dispersion relation of the guided modes supported by the wire medium slab is the same as the one obtained in Ref. [21] for the spoof plasmons supported by an array of grooves.

The question that arises at this point is the following: "How can we overcome these apparently fundamental limitations of bandwidth and physical size inherent to conventional spoof plasmon topologies?" Following the discussion above, an intuitive possibility is to

---

[3] We used the approach described in detail in Sec. II.3.1, which takes into account the effects of spatial dispersion and additional boundary conditions. In particular, we considered TM polarization (configuration I) and $\alpha = 0^\circ$ (α is the angle between the wires and the *z* direction). The dispersion characteristic was then obtained by calculating the values of k_x for which the wire medium can sustain a propagating wave attached to the interface with no incident field, $H_y^{\mathrm{inc}} = 0$. It should be noted that the coordinate system in this case is different from the considered in Sec. II.3.1 (see inset of Fig. 4.3 and Fig. 2.2a).

have strongly coupled resonators in a broad range of frequencies. In the next section, we will discuss in detail how this can be done.

IV.3. Spatially Induced Surface Waves – Interlaced Plasmons

IV.3.1. Heuristic Considerations

After the brief introduction into the physics of spoof plasmons made in the previous section, here we heuristically explain how their intrinsic limitations may be surpassed, so that broadband ultra-subwavelength waveguiding in the perfectly conducting limit (i.e. when $\varepsilon_m \to -\infty$, which corresponds to microwave and terahertz frequencies; see Fig. 4.1a) can be indeed achieved. The underlying idea is to force the surface plasmons to strongly interact on a length scale not determined by the wavelength of light. To see how this can be done, let us consider again the wire medium slab described before (inset of Fig. 4.3). From a microscopic point of view, the electric field associated with a guided mode supported by the array of parallel metallic wires is a superposition of the electromagnetic fields created by the currents flowing in each wire, and thus it can be regarded as the result of the interaction of weakly bounded and weakly coupled surface plasmons. On the other hand, from a macroscopic perspective (after some spatial averaging is considered) the only non-zero electric field components associated with the guided mode propagating along the x direction are E_x and E_z. Moreover, since the tangential electric field at the metallic wires is weak, for long wavelengths the dominant (macroscopic) electric field component is E_x (TEM mode). In order to explain how this can be used to enhance the interaction between surface plasmons, first let us suppose that all the wires are rotated by -45° around the y-axis, so that they become parallel to the unit vector $\hat{\mathbf{u}}_1 = (1,0,1)/\sqrt{2}$. In this case, nothing particularly exciting happens, except that the dominant component of the electric field is no longer E_x, but instead it is the projection of the electric field on $\hat{\mathbf{u}}_2 = (-1,0,1)/\sqrt{2}$. However, something really dramatic happens if we entangle two of such tilted wire medium slabs, with wires oriented along perpendicular directions. Specifically, we want to consider a crossed wire mesh such that the planes $y = la$ contain wires oriented along $\hat{\mathbf{u}}_1$, and the planes $y = la + a/2$ contain wires oriented along $\hat{\mathbf{u}}_2$, where l is an integer number (Fig. 4.4)[4].

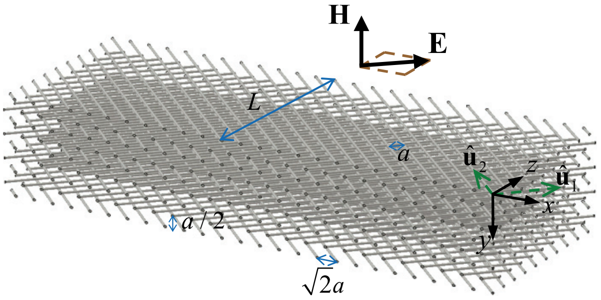

Fig. 4.4. Two tilted wire medium slabs are geometrically entangled resulting in the hybridization of the weakly bounded plasmons supported by each of them. The structure is formed by two sets of parallel wires arranged in square lattices with lattice constant a. The set of wires oriented along the direction $\hat{\mathbf{u}}_1$ is located in planes $y = la$ (l is an integer), whereas the complementary set is oriented along $\hat{\mathbf{u}}_2$ and located in planes $y = (l + 1/2)a$. The wires are embedded in a dielectric with relative permittivity ε_h.

In fact, this "double wire medium" has been considered in some previous works in many other contexts [29-31], and also in Sec. III.3 of this thesis, and thus some of its unique and unusual features have already been highlighted. What is really peculiar about this structure is that the wire mesh formed by wires oriented along $\hat{\mathbf{u}}_1$ creates an electric field mainly oriented along the direction $\hat{\mathbf{u}}_2$, which is thus strongly interacting with the set of wires

---

[4] It should be noted that the metamaterial geometry of Fig. 4.4 is exactly the same as that considered in the previous chapter (see Fig. 3.14 of Sec. III.3.2). However, the context of the problems is completely different in the two cases. While in Sec. III.3.2 the physical response of the crossed wire mesh was analyzed in terms of far-field excitation, here we are interested in the study of the guided modes excited by the near-field evanescent spectrum of a given source.

oriented along $\hat{\mathbf{u}}_2$, and vice-versa. Thus, each wire mesh effectively blocks the electric field created by the currents flowing in the complementary wire mesh, and thus effectively repels the electric field away forcing fluctuations of the charge density in a subwavelength scale, and thus a strong confinement of the associated fields. This enables a mesoscopic excitation designated here as “interlaced plasmon pair” to emphasize that its physical origin is rooted on the spatial entanglement of the charge density waves supported by perpendicular wire dipoles.

In order to verify these heuristic considerations, in the next section we introduce an analytical model to characterize the dispersion characteristic of the interlaced plasmons. After this, the dispersion properties of such spatially induced plasmons are presented and discussed in detail in the following sections.

IV.3.2. Analytical Model

The dispersion of the guided modes supported by the considered metamaterial slab (Fig. 4.4) can be obtained in the usual way by expanding the electromagnetic fields in the air and metamaterial regions in terms of plane waves. Supposing that the magnetic field is along the *y* direction we have that (a variation $e^{j(\omega t-k_x x)}$ of the fields is assumed but omitted):

$$\begin{aligned} H_y &= A_1 e^{-\gamma_0(z-L)}, \quad z>L \\ H_y &= B_1^+ e^{-jk_z^{(1)}z} + B_1^- e^{jk_z^{(1)}z} + B_2^+ e^{-jk_z^{(2)}z} + B_2^- e^{jk_z^{(2)}z} + \\ &\quad B_3^+ e^{-jk_z^{(3)}z} + B_3^- e^{jk_z^{(3)}z}, \quad 0<z<L \\ H_y &= A_2 e^{\gamma_0 z}, \quad z<0 \end{aligned} \tag{4.1}$$

In the above, $\gamma_0 = \sqrt{k_x^2 - \omega^2 \varepsilon_0 \mu_0}$ is the free space propagation constant, k_x is the wave number of the guided mode, $k_z^{(1,2,3)}$ are the propagation constants of the modes excited inside the double wire medium, and $A_{1,2}$ and $B_{1,2,3}^{\pm}$ are the complex amplitudes of the excited plane waves in the air and metamaterial regions, respectively. As in Sec. III.3.2, the propagation constants $k_z^{(1,2,3)}$ can be obtained by solving the plane wave dispersion characteristic given by Eq. (3.26) with respect to k_z. However, whereas in the problem of Sec. III.3 the wires are assumed to be perfectly electrical conducting (PEC) and thus ε_{11} and ε_{22} are simply given by Eq. (3.25), here we want to take into account the effect of finite conductivity of the metal. In such circumstances, it can be found that the permittivity components ε_{11} and ε_{22} are given by [32],

$$\varepsilon_{ii}\left(\omega,k_i\right)=1+\frac{1}{\dfrac{1}{(\varepsilon_m/\varepsilon_h-1)f_V}-\dfrac{\varepsilon_h\left(\omega/c\right)^2-k_i^2}{\beta_p^2}},\quad i=1,2 \tag{4.2}$$

where c is the speed of light in vacuum, $\beta_p=[2\pi/(\ln(a/2\pi r_w)+0.5275)]^{1/2}/a$ is the plasma wave number, $k_i=\mathbf{k}\cdot\hat{\mathbf{u}}_i$ (i=1,2), ε_h is the permittivity of the host dielectric, ε_m is the complex permittivity of the metal, r_w is the radius of the wires, and $f_V=\pi(r_w/a)^2$. (As an aside, it is worth noting that the particular case of PEC wires (Eq. (3.25)) can be regarded as the limit situation in which $\varepsilon_m=-\infty$ in Eq. (4.2)). It can be verified that, as in Sec. III.3.2, the characteristic equation is equivalent to a polynomial of degree three in the variable k_z^2, and this is why the magnetic field inside the metamaterial is a superposition of six waves (Eq. (4.1)); three waves propagate along the direction $+z$ and the other three along the direction $-z$, all of them associated with a magnetic field of the form $\mathbf{H}=H_0e^{-j\mathbf{k}\cdot\mathbf{r}}\hat{\mathbf{u}}_y$. It should be recalled that the emergence of additional waves is a consequence of the strong spatially dispersive of the crossed wire mesh [29, 33-34], as already discussed in the previous chapters.

As in Sec. III.3.2, the electric field can be written in all space using Eq. (3.28). Then, by applying the classical boundary conditions that impose the continuity of the tangential components of the electromagnetic fields, together with the set of additional boundary conditions (ABCs) that guarantee that the microscopic current associated with each wire vanishes at the interfaces (see Eq. 3.29 in Sec. III.3.2), we can obtain a 8×8 linear system. The dispersion characteristic of the guided modes supported by the structured material is then obtained by setting the determinant of this linear system equal to zero, and by computing the wave number k_x as a function of the frequency ω.

IV.3.3. Dispersion Characteristics

IV.3.3.1 PEC approximation

Here, we characterize the dispersion of the guided modes (interlaced plasmons) supported by the crossed wires substrate, assuming that the metallic wires are perfect electric conductors (PECs) (Fig. 4.4). In particular, Fig. 4.5a depicts the dispersion characteristic of the interlaced plasmons for structured slabs with a fixed thickness L and different densities of wires a/L. The results (solid lines) were calculated analytically using the procedure outlined in the previous section based on the nonlocal homogenization model. In order to check the accuracy of these results, we have as well calculated the dispersion characteristic of the guided modes with the eigenmode solver of CST Microwave Studio [35] (discrete symbols). Fig. 4.5a clearly shows that the analytical results follow remarkably well the full wave results.

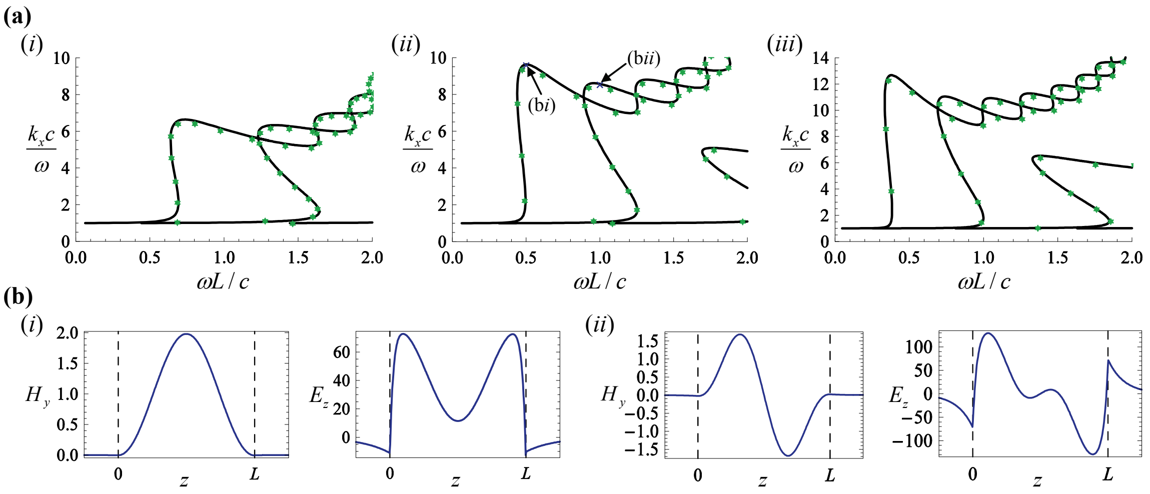

Fig. 4.5. (a) Normalized propagation constant k_x of the interlaced plasmons as a function of the normalized frequency, for a fixed waveguide thickness L and different lattice periods a. The wires are assumed to be PEC and its radius is $r_w = 0.05a$. (*i*) $a = L/10$, (*ii*) $a = L/15$, and (*iii*) $a = L/20$. The black solid curves were obtained from the homogenization model (Sec. IV.3.2), whereas the green discrete symbols were calculated using the eigenmode solver of CST Microwave Studio [35]. (b) Profiles of $H_y[A/m]$ and $E_z[V/m]$; (*i*) and (*ii*) correspond to the points (b*i*) and (b*ii*) of Fig. 4.5a(*ii*).

As seen in Fig. 4.5a, the considered slab has an exotic and intriguing dispersion diagram, where the peculiarity of the different branches of the dispersion characteristic being strongly interlaced one with another clearly stands out: a feature not seen in the dispersion diagrams of either dielectric or metal based planar waveguides. The physical origin of this dispersion entanglement is simply rooted in the geometry of the structure, as already heuristically predicted in Sec. IV.3.1. Specifically, it is a consequence of the strong non-resonant interaction between the weakly bounded plasmons supported by each array of wires.

The dispersion diagrams of Fig. 4.5a clearly show that the metamaterial slab supports highly confined guided modes (with $k_x c/\omega >> 1$) even when the thickness L of the waveguide is ultra-subwavelength ($L/\lambda \le 1/10$). This occurs, for example, in Fig. 4.5a(*ii*) for frequencies larger than $\omega L/c \approx 0.5$ as well as in Fig. 4.5a(*iii*) for frequencies larger than $\omega L / c \approx 0.4$, extending over a wide frequency band. Thus, unlike the spoof plasmons (see Fig. 4.2b and Fig. 4.3), the interlaced plasmons exhibit, indeed, a truly subwavelength nature and an extremely broadband response. Therefore, the crossed wires waveguide is significantly more robust in terms of bandwidth and reduced physical size than approaches based on spoof surface plasmons, which makes it a quite interesting solution for subwavelength field confinement and waveguiding. It is worth underlining, moreover, that since the spatial period of oscillations of the interlaced plasmons is mainly determined by the lattice constant of the wire grids rather than by the electrical length of the metal structures as is the case of spoof plasmons, the degree of field confinement can be simply enhanced by increasing the density of wires, i.e. by reducing a / L, even if the metal volume fraction is kept fixed (see Fig. 4.5a(*i*)-(*iii*)).

In order to further characterize the interlaced plasmons, we depict in Fig. 4.5b the transverse electromagnetic fields distributions of the guided modes for some chosen points marked in Fig. 4.5a(*ii*), calculated using the analytical model delineated in Sec. IV.3.2. These plots clearly confirm that the electromagnetic fields associated with the interlaced plasmons may be strongly confined inside the substrate despite its subwavelength thickness. In fact, these results were expected from the dispersion diagrams of the interlaced plasmons (Fig. 4.5a), since we should notice that the fields in the air regions decay with the attenuation constant $\gamma_0 = (\omega / c)\sqrt{(k_x c / \omega)^2 - 1}$, and thus the characteristic decay length in the transverse direction can be a tiny fraction of the wavelength in free-space. Moreover, it is interesting to note in Fig. 4.5b that the normal E_z-field component flips sign within a small layer close to the interface, similar to what happens in optics [36]. On the other hand, it is also noticeable in the results of Fig. 4.5b that, consistent with the results of the previous chapter (Sec. III.3), the transverse impedance of the crossed wire mesh may be relatively low, since the amplitudes of the transverse electric and magnetic fields inside the structured material are approximately of the same order. Finally, we should refer that in order to achieve a same level of confinement (same value of k_x) in a dielectric waveguide with the same thickness as in the example of Fig. 4.5a(*ii*), at the normalized frequency $\omega L / c = 0.5$, it would be necessary to use a dielectric with permittivity $\varepsilon_d \approx 130$.

At this point, it is also important to emphasize that the coupling between the two wire grids is particularly strong when the wires make angles $\alpha_1 = 45^\circ$ and $\alpha_2 = -45^\circ$ with respect to the interfaces. As shown in Appendix A in detail, if $\alpha_1 = 90^\circ$ and $\alpha_2 = 0^\circ$ the electromagnetic response of the structure is completely different. In particular, the dispersion characteristics of the guided modes are no longer characterized by that peculiar entanglement depicted in Fig. 4.5a. Moreover, the degree of field confinement provided in this case is significantly reduced, especially for low frequencies.

IV.3.3.2 Effects of losses and material dispersion

So far we have assumed that the metallic wires were perfect electric conductors (PECs). Even though the PEC approximation may be very accurate at microwaves, at higher frequencies (terahertz, infrared, and optical regimes) the effect of losses and the plasmonic response of metals cannot be neglected. Thus, in order to provide a more comprehensive understanding of the dispersion of the interlaced plasmons and better evaluate their waveguiding capabilities, we analyze next the variation of the propagation constant $k_x = k_x^{'} - jk_x^{''}$ with the frequency assuming that the wires are made up of a realistic metal (specifically, Ag) that follows the Drude dispersion model $\varepsilon_m = \varepsilon_\infty - \omega_p^2 / (\omega(\omega - j\Gamma))$, with the same parameters introduced above (see Fig. 4.1) and taken from the literature [13]. More specifically, we analyze the field confinement (related to the real part of the propagation constant k_x') and the propagation length (given by $\delta_x = 1/k_x''$) of the fundamental guided mode at different spectral windows from microwave to near-infrared frequencies using the analytical model described in Sec. IV.3.2 (Fig. 4.6).

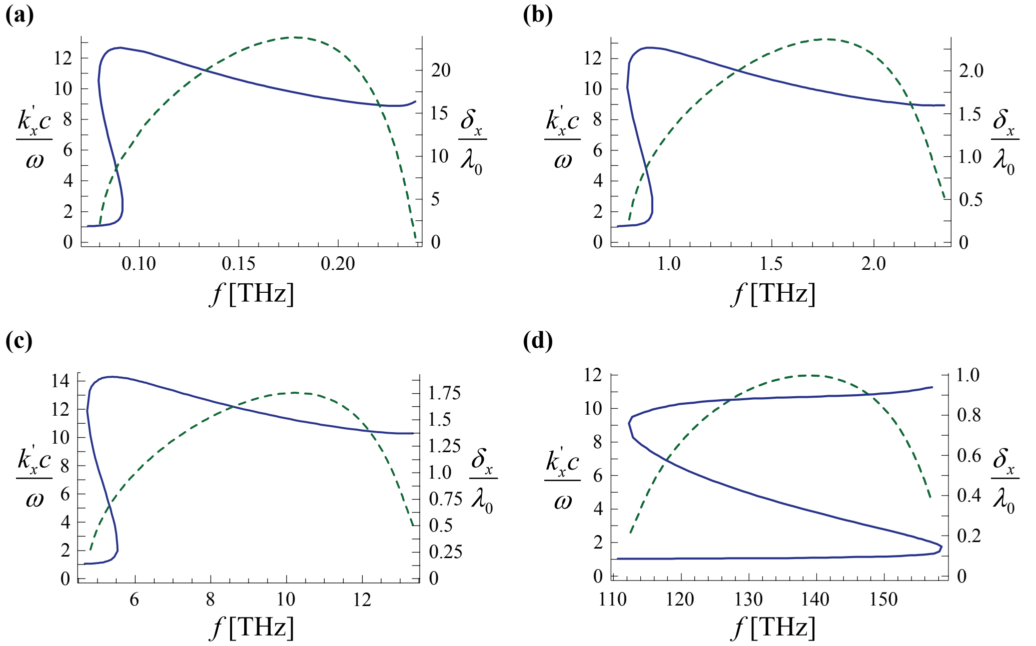

Fig. 4.6. Real part of the normalized propagation constant k_x' (solid blue curves) and normalized propagation length $\delta_x = 1/k_x''$ (dashed green curves) of the fundamental (even) interlaced plasmon pair at different frequency windows. (a) $L = 0.2$ mm, $a = L/20 = 10\ \mu$m, and $r_w = 0.05a = 0.5\ \mu$m; (b) $L = 20\ \mu$m, $a = L/20 = 1\ \mu$m, and $r_w = 0.05a = 50$ nm; (c) $L = 3\ \mu$m, $a = L/15 = 0.2\ \mu$m, and $r_w = 0.125a = 25$ nm; (d) $L = 0.2\ \mu$m, $a = L/3 = 66.7$ nm, and $r_w = 0.2a = 13.3$ nm. The wires are made of Ag. The results were obtained with the analytical model introduced in Sec. IV.3.2.

By comparing Fig. 4.6a with Fig. 4.5a(*iii*), one can conclude that in the microwave regime the behavior of the fundamental interlaced plasmon is, indeed, nearly unaffected by the metallic losses. In particular, the degree of field confinement (related to the real part of the propagation constant k_x') is very similar to that in PEC case (Fig. 4.5a(*iii*)). Moreover, the imaginary part of the propagation constant k_x'' is quite small ($k_x''/k_x' << 1$) and, consequently, the highly confined fundamental interlaced plasmon pair can propagate long distances before vanishes (of the order of twenty free-space wavelengths) (Fig. 4.6a). In fact, these results were completely expected, since at microwave frequencies real metals mimic closely perfect electric conductors (PECs), specifically, when the radius of the wires is much larger than the metal skin depth.

A closer look to Fig. 4.6a reveals, however, that there are some specific frequency regions where the effect of loss is more pronounced (i.e., $\delta_x \to 0$). Specifically, this happens in the frequency points where the dispersion curve bends over itself (we designate it as "dispersion elbows"), because in such regions the group velocity is extremely low and may vanish. This topic of the group velocity of the fundamental interlaced plasmon will be discussed in the next section.

At higher frequencies the metal progressively loses the conducting properties, and the plasmonic and loss effects become gradually more important (see Fig. 4.1a). Nevertheless, at terahertz frequencies (or low far-infrared frequencies) the level of field confinement (related to $k_x^{'}c/\omega$) remains very similar to the PEC case (see Fig. 4.6b and Fig. 4.5a(*iii*)). Hence, in contrast to the surface plasmons supported by semiconductor plasmonic-type waveguides at terahertz frequencies (see Fig. 4.2a), the behavior of the interlaced plasmons is weakly sensitive to material losses (Fig. 4.6b). On the other hand, the propagation length δ_x of the fundamental interlaced plasmon at terahertz frequencies is naturally shorter compared to the corresponding in the microwave regime. Still, Fig. 4.6b shows that a propagation length δ_x of two free-space wavelengths (which corresponds to about twenty guided wavelengths inside the structure) can be achieved. Actually, ensuring that $r_w > \delta_s$ (where δ_s is the skin depth of Ag), the strongly confined mode (with a similar field confinement as in Fig. 4.6a-b) can propagate nearly two free-space wavelengths before the amplitude of the field decreases by a factor $e^{-1} = 0.37$ (37%) even at higher far-infrared frequencies (Fig. 4.6c).

Naturally, by moving to an even higher frequency of operation (or shorter wavelength), the propagation length is further decreased. For example, it is seen in Fig. 4.6d that at near-infrared frequencies the fundamental interlaced plasmon propagates as far as λ_0 with a field attenuation less or equal than 37%. We would like to point out that, this value of the propagation length of the fundamental interlaced plasmon ($\delta_x = \lambda_0$), which may seem too small at first sight for waveguiding applications, corresponds to a considerably long distance when compared to the width of the waveguide ($\delta_x \approx 10L \approx 2\ \mu\text{m}$). In fact, even if a propagation length of $\delta_x \approx 2\ \mu\text{m}$ at near-infrared frequencies may not be enough in some specific waveguiding contexts, the deeply subwavelength characteristic of the interlaced plasmons may have other interesting applications. In particular, a tapered version of our structure can be potentially used to confine in a very subwavelength volume the electromagnetic radiation (nanofocusing) somehow similar to the effects reported in Refs. [19, 27].

Finally, it should be mentioned that due to the intrinsic plasmonic properties of noble metals in the infrared and optical regimes, it may be possible to have comparable values of $k_x^{'} c / \omega$ (i.e. the same level of field confinement) at higher frequencies with less dense meshes (i.e. meshes with larger values of a / L). In principle, the crossed wire mesh may be designed to operate at larger (near-infrared and optical) frequencies, but in such frequency bands its advantages as compared to a single metal rod (Fig. 4.1b) may be less evident (notice that the density of wires in Fig. 4.6d is already relatively low). Moreover, it is important to underline that in all the examples of Fig. 4.6 longer propagation distances are feasible if the radiation confinement is reduced (e.g. if the density of wires is decreased).

IV.3.4. Group Velocity

As already noted in the previous sections, an interesting part of the dispersion diagram of the interlaced plasmons (Fig. 4.5a and Fig. 4.6) corresponds to the regions where $n_{\text{eff}} = k_x c / \omega$ varies very steeply and then bends over itself. Notice that n_{eff} may be regarded as the effective index of refraction seen by the guided mode. In such branches the group velocity of the interlaced plasmon, given by $v_g = d\omega / dk_x = c / (n_{\text{eff}} + k_0\, dn_{\text{eff}} / dk_0)$ (with $k_0 = \omega / c$), can be extremely small, and even become negative (backward wave). Moreover, also in the wideband regions where $n_{\text{eff}} >> 1$ and n_{eff} varies little with the frequency, the group velocity $v_g \approx c / n_{\text{eff}}$ can be quite small. These properties of the interlaced plasmons may be quite interesting for slow light applications [37-39].

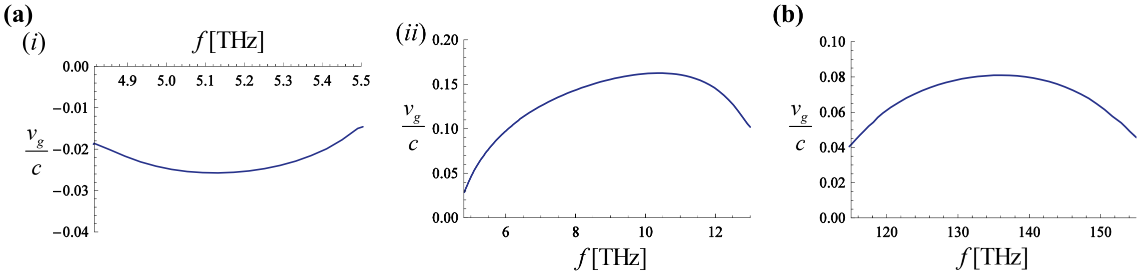

Fig. 4.7. Normalized group velocity v_g / c of the fundamental (even) interlaced plasmon pair as a function of the frequency for the metamaterial configurations of Fig. 4.6c (a) and Fig. 4.6d (b).

In order to illustrate these potential slow light regimes, in Fig. 4.7 we depict the group velocity of the fundamental interlaced plasmon for the metamaterial configurations of Fig. 4.6c-d at specific frequency ranges. Fig. 4.7a(*i*) shows the group velocity of the fundamental interlaced plasmon for the waveguide configuration of Fig. 4.6c at the frequency window $4.8\,\mathrm{THz} < f < 5.5\,\mathrm{THz}$. The group velocity in such frequency range is negative and approximately fifty times lower than the speed of light; hence there is a propagation of a slow backward guided wave. As the dispersion curve moves toward the dispersion elbow (see Fig. 4.6c), the fundamental interlaced plasmon turns from a backward wave into an extremely confined forward wave ($k_x c / \omega >> 1$ and $v_g > 0$), passing, of course, through a region of stopped light ($v_g = 0$) at the intermediate point. It is shown in Fig. 4.7a(*ii*) that in this wideband region of strong field confinement (approximately from $5\,\mathrm{THz}$ to $13\,\mathrm{THz}$), the group velocity of the fundamental interlaced plasmon may be of the order of $0.1c$ (where c is the speed of light in vacuum). At higher frequency regimes, the ultra-confined fundamental interlaced plasmon can propagate even more slowly and over a much wider spectral band (Fig. 4.7b). Specifically, in the near-infrared regime, the group velocity of the interlaced plasmon can be as low as $0.04c$ over a frequency band of about $40\,\mathrm{THz}$ (specifically, from $115\,\mathrm{THz}$ to $155\,\mathrm{THz}$).

As a final note, it is worth noting that in this wideband regime characterized by strong field confinement ($n_{\mathrm{eff}} = k_x c / \omega >> 1$), despite the fact that n_{eff} decreases with the frequency, the group velocity remains positive. This effect is closely related to the anomalous dispersion effect identified in Ref. [31].

IV.3.5. Experimental Verification

In order to further validate the theoretical findings of the previous sections, and to demonstrate that to obtain a huge field confinement it is enough to consider a few planes of metallic wires, we fabricated a prototype of the crossed wires waveguide (scaled to operate at microwaves) using standard printed circuit techniques (Fig. 4.8a). The width of the waveguide is $L = 20a = 31.48$ mm, the length along the x direction is $L_x = 4L$, and along the y direction the waveguide is formed by only four planes of wires. The cylindrical metallic wires are replaced by metallic strips with width $w_s = \pi r_w = \pi a / 20 \approx 0.25$ mm, and the host dielectric is RT/duroid 5880, characterized by $\varepsilon_h = 2.2$, loss tangent $\tan\delta \approx 6.5\times10^{-4}$, and thickness 0.787 mm. The metamaterial waveguide is excited by a short printed dipole-type antenna, and the y component of the magnetic field along and across the waveguide was measured using a near-field scanner with a round shielded loop probe and a vector analyzer (R&S ZVB20).

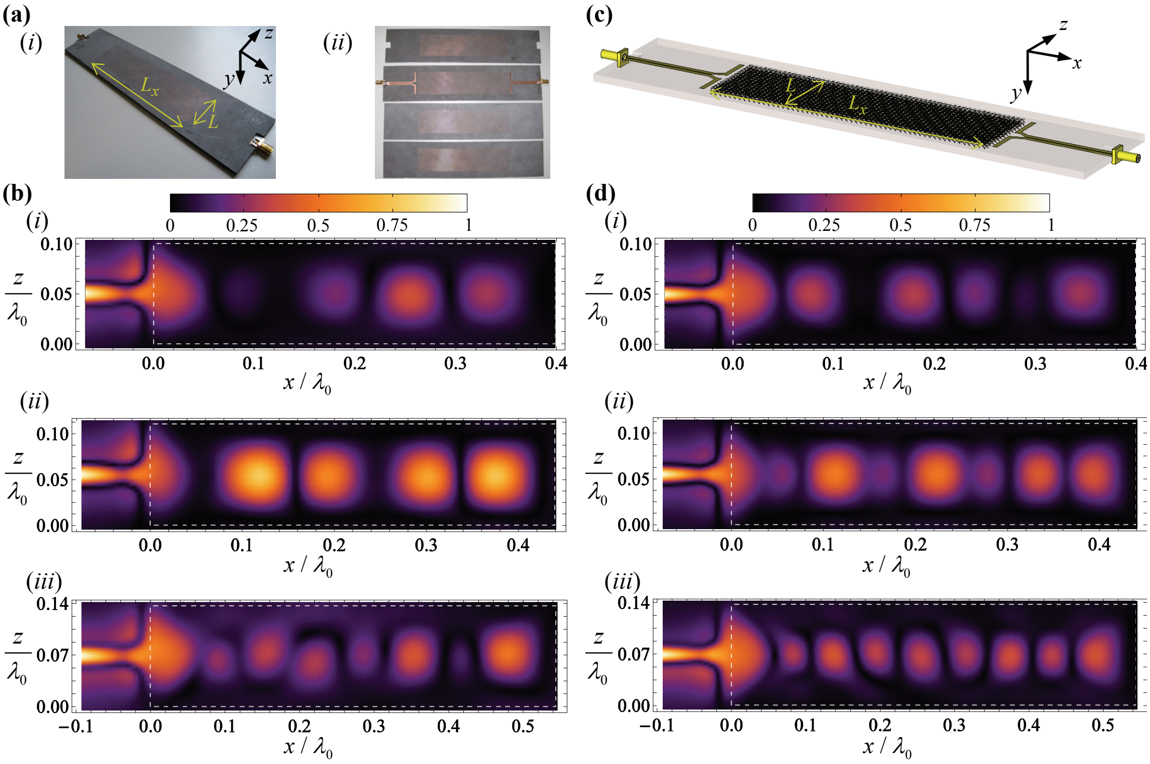

Fig. 4.8. (a) Photo of the crossed wires waveguide prototype. (*i*) General view; (*ii*) View of the four printed boards; The width of the waveguide is $L = 31.48$ mm, the length is $L_x = 4L$, the lattice constant is $a = L/20$, and the width of the metallic strips is $w_s = 0.25$ mm. (b) Normalized measured amplitude of H_y for (*i*) 950 MHz; (*ii*) 1.05 GHz; (*iii*) 1.3 GHz. (c) Crossed wires waveguide as simulated in Microwave Studio [35]. (d) The same as in panel (b), but calculated with Microwave Studio.

The measured normalized amplitude of H_y is depicted in Fig. 4.8b for different values of frequency (0.95-1.3 GHz). In all the density plots of Fig. 4.8b the excitation of the ultra-subwavelength guided modes (interlaced plasmons) inside the crossed wires waveguide by the near-field spectrum of the dipole antenna is quite evident, confirming the results of Fig. 4.5a(*iii*). One can clearly see that, notwithstanding the deeply subwavelength dimensions of the waveguide (of the order of one tenth of the wavelength), the considered substrate supports the propagation of the strongly confined interlaced plasmons. Notice that since the waveguide is not matched to the dipole antennas, in general, the field inside the slab is the superposition of two waves propagating along opposite directions (a standing wave). Moreover, it should be noted that the electromagnetic mode excited in the crossed wires waveguide corresponds to the fundamental one, since the magnetic field exhibits an even symmetry with respect to the transverse direction (*z* direction) (see Fig. 4.5b(*i*)).

In order to validate the experimental results, we have also simulated the response of the metamaterial waveguide using CST Microwave Studio [35]. The full wave results are depicted in Fig. 4.8d, from which one can see that the numerical and experimental results are in good agreement. Nevertheless, some minor discrepancies can be observed between the simulated and measured magnetic field distributions. The reason for the slight disagreement may be either related to fabrication imperfections or with deviations in the dielectric substrate permittivity. On the other hand, owing to its subwavelength dimensions, the printed dipole antenna used as the near-field source is extremely sensitive, and hence, may also contribute to the slight mismatch between the numerical and experimental results.

As a final note, we would like to point out that, consistent with our discussion in Sec. IV.3.3.2, the proposed structure may be scaled down to shorter wavelengths. Thus, it would be very interesting to fabricate a prototype of the crossed wires waveguide to operate at higher frequency regimes (terahertz or infrared ranges) using nanoimprint techniques.

IV.4. Concluding Remarks

In this chapter, it was shown that a crossed wire mesh supports highly confined eigenmodes and a slow light regime, even when the thickness of the waveguide is deeply subwavelength. Such charge density waves designated here as interlaced plasmons are mesoscopic excitations rooted in the strong non-resonant interaction between perpendicular wire grids that support weakly bounded plasmons, and their characteristic spatial period is determined by intrinsic geometrical features rather from the electric size of the metal elements (as is the case of conventional spoof surface plasmons). We have compared our crossed wires waveguide with other structures based on spoof plasmons or materials with a plasmonic response at terahertz frequencies, demonstrating the superior potential of waveguiding based on interlaced plasmons in terms of physical size, bandwidth and tolerance to absorption. Therefore, these spatially interlaced plasmons may have exciting applications in subwavelength waveguiding in the microwave, terahertz, and infrared frequency bands. Finally, the emergence of interlaced plasmons was experimentally verified at microwave frequencies.

References

[1] C. A. Balanis, *Advanced Engineering Electromagnetics*, New York: Wiley, 1989.

[2] M. Born and E. Wolf, *Principles of Optics*, 7th ed., Cambridge University Press, Cambridge, 1999.

[3] B. E. A. Saleh and M. C. Teich, *Fundamentals of Photonics*, New York: Wiley, 1991.

[4] S. A. Maier, *Plasmonics: Fundamentals and Applications*, Springer, New York, 2007.

[5] S. A. Maier and H. A. Atwater, "Plasmonics: Localization and guiding of electromagnetic energy in metal/dielectric structures", *J. Appl. Phys.*, vol. 98, p. 011101, 2005.

[6] W. L. Barnes, A. Dereux, T. W. Ebbesen, "Surface plasmon subwavelength optics", *Nature*, vol. 424, p. 824, 2003.

[7] D. K. Gramotnev, S. I. Bozhevolnyi, "Plasmonics beyond diffraction limit", *Nature Photon.*, vol. 4, p. 83, 2010.

[8] E. Ozbay, "Plasmonics: Merging Photonics and Electronics at Nanoscale Dimensions", *Science*, vol. 311, p. 189, 2006.

[9] H. A. Atwater, "The Promise of Plasmonics", *Sci. Am.*, vol. 296, p. 56, 2007.

[10] S. Lal, S. Link, and N. J. Halas, "Nano-optics from sensing to waveguiding", *Nature Photon.*, vol. 1, p. 641, 2007.

[11] T. W. Ebbesen, C. Genet, and S. Bozhevolnyi, "Surface-plasmon circuitry", *Phys. Today*, vol. 61, p. 44, 2008.

[12] M. I. Stockman, "Nanoplasmonics: The physics behind the applications", *Phys. Today*, vol. 64, p. 39, 2011.

[13] M. A. Ordal, R. J. Bell, R. W. Alexander, Jr, L. L. Long, M. R. Querry,"Optical properties of fourteen metals in the infrared and far infrared: Al, Co, Cu, Au, Fe, Pb, Mo, Ni, Pd, Pt, Ag, Ti, V, and W", *Appl. Opt.*, vol. 24, p. 4493, 1985.

[14] J. Takahara, S. Yamagishi, H. Taki, A. Morimoto, and T. Kobayashi, "Guiding of a one-dimensional optical beam with nanometer diameter", *Opt. Lett.*, vol. 22, p. 475, 1997.

[15] Craig F. Bohren, Donald R. Huffman, *Absorption and Scattering of Light by Small Particles*, John Wiley & Sons, 1983.

[16] J. Zenneck, "Ueber die Fortpflanzung ebener elektromagnetischer Wellen laengs einer ebenen Leiterflaeche und ihre Beziehung zur drahtlosen Telegraphie", *Annu. Phys.*, vol. 23, pp. 846, 1907.

[17] A. Sommerfeld, "Ueber die Fortpflanzung elektrodynamischer Wellen laengs eines Drahtes", *Ann. Phys. Chem.*, vol. 67, p. 233, 1899.

[18] J. G. Rivas, C. Janke, P. H. Bolivar and H. Kurz. “Transmission of THz radiation through InSb gratings of subwavelength aperture”, *Opt. Express*, vol. 13, p. 847, 2005.

[19] S. A. Maier, S. R. Andrews, L. Martín-Moreno, and F. J. García-Vidal, “Terahertz Surface Plasmon-Polariton Propagation and Focusing on Periodically Corrugated Metal Wires”, *Phys. Rev. Lett.*, vol. 97, p. 176805, 2006.

[20] J. B. Pendry, L. Martín-Moreno, F.J. Garcia-Vidal, “Mimicking Surface Plasmons with Structured Surfaces”, *Science*, vol. 305, p. 847, 2004.

[21] F. J. Garcia-Vidal, L. Martín-Moreno, and J. B. Pendry, “Surfaces with holes in them: new plasmonic metamaterials”, *J. Opt. A: Pure Appl. Opt.*, vol. 7, p. 97, 2005.

[22] C. R. Williams, S. R. Andrews, S. A Maier, A. I. Fernández-Dominguéz, L. Martín-Moreno and F. J. García-Vidal, “Highly confined guiding of terahertz surface plasmon polartions on structured metal surfaces”, *Nature Photonics*, vol. 2, p. 175, 2008.

[23] A. P. Hibbins, B. R. Evans, J. R. Sambles, “Experimental Verification of Designer Surface Plasmons”, *Science*, p. 308, p. 670, 2005.

[24] S. H. Mousavi, A. B. Khanikaev, B. Neuner III, Y. Avitzour, D. Korobkin, G. Ferro, and G. Shevts, “Highly Confined Hybrid Spoof Surface Plasmons in Ultrathin Metal-Dielectric Heterostructures”, *Phys. Rev. Lett.*, vol. 105, p. 176803, 2010.

[25] M. Navarro-Cía, M. Beruete, S. Agrafiotis, F. Falcone, M. Sorolla, and S. Maier, “Broadband spoof plasmons and subwavelength electromagnetic energy confinement on ultrathin metafilms”, *Opt. Express*, vol. 17, p. 18184, 2009.

[26] G. Goubau, “Surface Waves and Their Application to Transmission Lines”, *J. Appl. Phys.*, vol.21, p. 1119, 1950.

[27] A. I. Fernández-Domínguez, L. Martín-Moreno, F. J. García-Vidal, S. R. Andrews, and S. A. Maier, “Spoof Surface Plasmon Polariton Modes Propagating Along Periodically Corrugated Wires”, *IEEE Journal of Selected Topics in Quantum Electronics*, vol. 14, p. 1515, 2008.

[28] F. Lemoult, G. Lerosey, and M. Fink, “Why the wire medium with finite dimensions makes a resonant metalens”, available at arxiv.org/abs/1006.0829v2.

[29] M. G. Silveirinha and C. A. Fernandes, “Nonresonant structured material with extreme effective parameters”, *Phys. Rev. B*, vol. 78, p. 033108, 2008.

[30] M. G. Silveirinha, C. A. Fernandes, J. R. Costa, "Superlens made of a metamaterial with extreme effective parameters", *Phys. Rev. B*, vol. 78, p. 195121, 2008.

[31] M. G. Silveirinha, "Anomalous dispersion of light colors by a metamaterial prism", *Phys. Rev. Lett.*, vol. 102, p. 193903, 2009.

[32] M. G. Silveirinha, "Nonlocal homogenization model for a periodic array of epsilon-negative rods", *Phys. Rev. E*, vol. 73, p. 046612, 2006.

[33] M. G. Silveirinha and C. A. Fernandes, "Homogenization of 3D- Connected and Non-Connected Wire Metamaterials", *IEEE Trans. Microwave Theory Tech.*, vol. 53, p. 1418, 2005.

[34] C. R. Simovski and P. A. Belov, "Low-frequency spatial dispersion in wire media", *Phys. Rev. E*, vol. 70, p. 046616, 2004.

[35] CST Microwave Studio 2010 (http://www.cst.com).

[36] A. Alù, N. Engheta, "Optical Nanotransmission Lines: Synthesis of Planar Left-Handed Metamaterials in the Infrared and Visible Regimes", *J. Opt. Soc. Am. B*, vol. 23, p. 571, 2006.

[37] J. T. Mok, B. J. Eggleton, "Expecting more delays", *Nature (London)*, vol. 433, p. 811, 2005.

[38] A. Karalis, E. Lidorikis, M. Ibanescu, J. D. Joannopoulos, and M. Soljačić, "Surface-Plasmon-Assisted Guiding of Broadband Slow and Subwavelength Light in Air", *Phys. Rev. Lett.*, vol. 95, p. 063901, 2005.

[39] Q. Gan, Z. Fu, Y. J. Ding, F. J. Bartoli, "Ultrawide-Bandwidth Slow-Light System Based on THz Plasmonic Graded Metallic Grating Structures", *Phys. Rev. Lett.*, vol. 100, p. 256803, 2008.

V. CONCLUSIONS

V.1. Main Results

In this thesis, we have presented a collection of exciting theoretical, numerical and experimental results on the potential applications of several different configurations of structured materials formed by metallic wires (not necessarily straight wires).

In Chapter II, we investigated the near-field imaging capabilities of a wire medium lens formed by tilted metallic wires. It was shown, as a generalization of the results of [1-2], that the considered metamaterial lens enables the transport of the subwavelength details associated with the electric field component parallel to the wires through an oblique projection. Such property implies that it is possible to image fields created by *s*-polarized sources, for which the electric field is parallel to the interfaces of the lens. This is a key advance since the standard wire medium lens configuration [1] is polarization sensitive and only enables subwavelength imaging of *p*-polarized waves. Then, taking advantage of the increased degrees of freedom provided by the tilted wire medium lens, we have established a simple and novel method to fully restore the electric near-field of an arbitrary source. The strategy is to rotate successively by 120° the near-field source (or equivalently the metamaterial lens) around the direction perpendicular to the interface plane so that three linearly independent components of the electric field can be measured. This theoretical possibility was successfully demonstrated experimentally at microwave frequencies using a fabricated prototype of the tilted wire medium lens. It is envisioned that the proposed system may find exciting applications in near-field measurement at the microwave and terahertz regimes.

In Chapter III, we explored two distinct routes to achieve negative refraction and, consequently, far-field focusing. In particular, in Sec. III.2 we demonstrated theoretically and numerically that by using helical shaped wires instead of straight wires, it is possible to suppress the spatial dispersion effects that characterize wire media even at low frequencies (microwave and low infrared frequencies), and that this enables a strong all-angle negative refraction effect. Subsequently, it was shown that a partial focusing of electromagnetic radiation may be achieved with a planar lens formed by such metamaterial structure by exploiting the negative refraction effect at both metamaterial interfaces. In Sec. III.3, we demonstrated numerically as well as experimentally a similar partial focusing effect using a different metamaterial structure formed by nonconnected crossed metallic wires. In this case, however, it was shown that the phenomenon of negative refraction responsible for this focusing effect relies on the spatially dispersive (or nonlocal) response of the metamaterial structure, in contrast to the local response of the helices medium. Lastly, it was theoretically predicted and numerically verified a simple way to boost the strength of the negative refraction effect in the crossed wire mesh, which consists in using crossed wire mesh configurations with angles between the two sets of parallel wires larger than 90°.

In Chapter IV, we studied both theoretically and experimentally the waveguiding properties of ultra-compact metamaterials formed by crossed metallic wires. It was analytically, numerically, and experimentally demonstrated that a waveguide formed by such structured material supports highly confined modes with a very peculiar entangled dispersion (interlaced plasmons), even for very long wavelengths (or ultra-subwavelength thicknesses). Moreover, it was shown that this waveguiding solution is significantly more robust in terms of bandwidth, reduced physical size, and tolerance to absorption than the known approaches based on spoof plasmons or materials with a plasmonic response at terahertz frequencies (semiconductor plasmonic-type waveguides). These characteristics are very encouraging for future practical applications of the proposed structure in ultra-subwavelength waveguiding from microwave to near-infrared frequencies.

V.2. Future Work

To conclude the thesis, we discuss possible extensions for the presented studies as well as other research directions.

Future work on the near-field reconstruction with a tilted wires lens might include testing the accuracy of the proposed experimental setup under different and more complex radiation sources. On the other hand, it would be interesting to numerically investigate the possibility of fully restoring the electric near-field at terahertz or even infrared frequencies using the introduced approach based on three independent measurements. This can be done using an electromagnetic simulator (e.g., CST Microwave Studio). This problem can also be studied analytically by expanding the field source into a Fourier integral of plane waves. In particular, the electromagnetic field at the image plane can be obtained in the usual way by integrating the incident electromagnetic field multiplied by the transmission coefficient of the metamaterial lens over all spatial harmonics. To this end, a general analytical formula for the transmission coefficient, applicable to arbitrarily polarized waves incident from arbitrary directions, should be derived. In principle, this can be done using an approach similar to the one reported in [C.3].

Another topic that merits further investigation is the negative refraction and partial focusing with a metamaterial lens formed by helical shaped wires. In particular, we intend to fabricate a prototype of the proposed focusing lens. For this purpose, instead of using the original configuration formed by cylindrical helical shaped wires, we will consider the alternative configuration formed by segmented helices (see inset of Fig. 3.9). As already anticipated in Sec. III.2.4.2, this alternative configuration may be fabricated using a layer by layer design with interconnecting vias, similarly to the mushroom-type structures [3-4]. At the same time, it may be interesting to investigate the effect of introducing air gaps in between the several metamaterial layers, as was done for the mushroom structures in [5]. Such modified structure may be much easier to fabricate than the original one formed by continuous helical shaped wires.

Still regarding the artificial medium formed by helical shaped metallic wires, it would be interesting to study the electromagnetic response of this structured material under transverse electric (TE) excitations (i.e, *s*-polarized waves), and to investigate if the non-bianisotropic helices medium (Fig. 3.1) may behave as an array of magnetic wires somewhat similar to the so-called Swiss rolls [6-7]. If so, this structure may be capable of transferring the subwavelength details of *s*-polarized waves from the source to the image plane.

As to the crossed wires waveguide, it would be interesting to fabricate a high-frequency prototype to operate at mid-infrared or even near-infrared frequencies using nanoimprint lithography. In addition, the physics of interlaced plasmons propagation in an adiabatically tapered crossed wires waveguide deserves a careful study. Based on the dispersion properties of the interlaced plasmons presented in Chapter IV, one may expect that a funnel-shaped version of the crossed wires waveguide may allow broadband and ultra-subwavelength energy concentration at terahertz and infrared frequencies. Also the possibility of slowing down or even stopping light in the crossed wires waveguide deserves further investigations.

References

[1] P. A. Belov, Y. Hao, and S. Sudhakaran, "Subwavelength microwave imaging using an array of parallel conducting wires", *Phys. Rev. B*, vol. 73, p. 033108, 2006.

[2] P. A. Belov and M. G. Silveirinha, "Resolution of subwavelength imaging devices formed by a wire medium", *Phys. Rev. E*, vol. 73, p. 056607, 2006.

[3] O. Luukkonen, P. Alitalo, F. Costa, C. Simovski, A. Monorchio, and S. Tretyakov, "Experimental verification of the suppression of spatial dispersion in artificial plasma", *Appl. Phys. Lett.*, vol. 96, p. 081501, 2010.

[4] M. J. Lockyear, A. P. Hibbins, and J. R. Sambles, "Microwave Surface-Plasmon-Like Modes on Thin Metamaterials", *Phys. Rev. Lett.*, vol. 102, p. 073901, 2009.

[5] C. S. R. Kaipa, A. B. Yakovlev, M. G. Silveirinha, "Characterization of negative refraction with multilayered mushroom-type metamaterials at microwaves", *J. Appl. Phys.*, vol. 109, p. 044901, 2011.

[6] M. Wiltshire, J. Hajnal, J. B. Pendry, and D. Edwards, "Metamaterial endoscope for magnetic field transfer: near field imaging with magnetic wires", *Opt. Express*, vol. 11, p. 709, 2003.

[7] M. C. K. Wiltshire, J. B. Pendry, W. Williams, and J. V. Hajnal, "An effective medium description of "Swiss-Rolls", a magnetic metamaterial", *J. Phys.: Condens. Matter*, vol. 19, p. 456216, 2007.

APPENDICES

A1. Guided Modes in a Crossed Wire Mesh with $\alpha_1 = 90^\circ$ and $\alpha_2 = 0^\circ$

In the present appendix, we characterize the dispersion characteristic of the guided modes supported by a crossed wire grid formed by sets of wires perpendicular and parallel to the interface plane (Fig. A.1). More specifically, one set of wires is oriented along the x direction, whereas the complementary set is oriented along the z direction. The two orthogonal sets of wires are spaced by $a/2$.

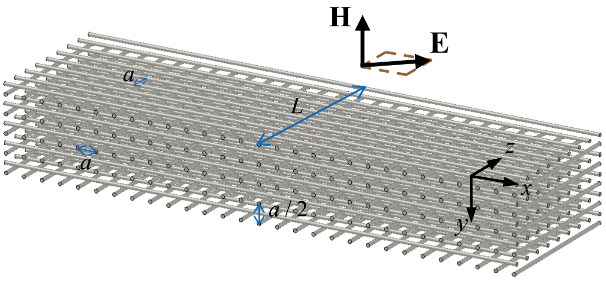

Fig. A.1. Modified crossed wire mesh configuration formed by two mutually orthogonal and nonconnected sets of wires oriented along x and z directions. The spacing between parallel wires is a, and the spacing between orthogonal wires is $a/2$.

In order to calculate the guided modes supported by a crossed wire grid slab with finite thickness L, we use an analytical model based on the transverse averaged (TA)-field approach introduced in Ref. [1], which takes into account the effects of spatial dispersion and additional boundary conditions [2]. The propagation problem (calculation of the guided modes) can be solved by setting the determinant of the linear system obtained from the matching of the tangential TA-electromagnetic fields (i.e., E_x and H_y) as well as of the normal component of the TA-electric field (E_z), and by computing the wave number k_x as a function of frequency. For more details about the analytical model the reader is referred to Ref. [1], especially Sec. VI.E.

Fig. A.2 depicts the dispersion characteristic of the TM-guided modes supported by a crossed wire grid slab (Fig. A.1) with a fixed thickness L and different densities of wires a/L. The solid curves were obtained using the analytical model based on the transverse averaged (TA)-field approach, whereas the discrete symbols were calculated with the eigenmode solver of CST Microwave Studio [3]. As seen in Fig. A.2, the results obtained using the two different methods concur very well.

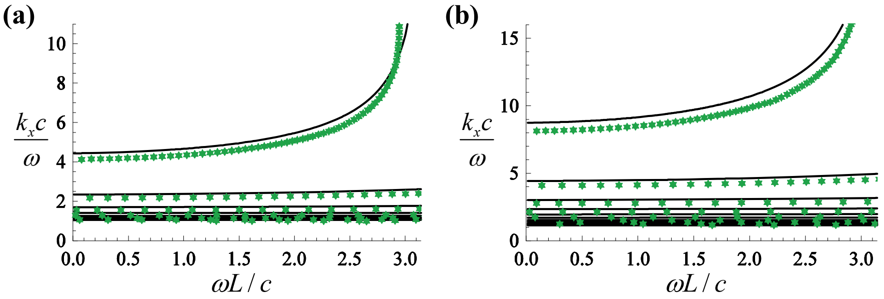

Fig. A.2. Normalized propagation constant k_x of the guided modes as a function of the normalized frequency, for a fixed waveguide thickness L and different lattice periods a. The wires are assumed to be PEC and its radius is $r_w = 0.05a$. (a) $a = L/10$, and (b) $a = L/20$. The black solid curves were obtained from the homogenization model, whereas the green discrete symbols were calculated using the eigenmode solver of CST Microwave Studio [3].

As one can see from Fig. A.2, the dispersion characteristic of the guided modes supported by the modified crossed wires waveguide (Fig. A.1) is completely different from that of the configuration studied in Sec. IV.3 (Fig. 4.5a). In particular, the absence of the entanglement of the different branches of the dispersion characteristic that characterizes the interlaced plasmons (Fig. 4.5a) promptly stands out from Fig. A.2. In contrast, this crossed wire mesh configuration (Fig. A.1) supports the propagation of several nearly dispersionless (flat) bands that are likely to be related to the weakly bounded surface plasmons supported by the wires oriented along the x direction. In addition, it sustains the propagation of a considerably more confined guided mode along the entire frequency band. Similar to the guided mode supported by the array of parallel metallic wires (Fig. 4.3), the degree of field confinement of the considered guided mode is strongly enhanced when the frequency is close to $\omega L / c = \pi$. However, in contrast to the single wire medium where $k_x c / \omega >> 1$ only for $\omega L / c \approx \pi$ (see Fig. 4.3), in this case $k_x c / \omega$ is substantially above the light line even for $\omega L / c << \pi$ (or equivalently, $L << \lambda_0 / 2$). Most likely, this fact is a consequence of some kind of interaction between the two perpendicular wire grids, which may deserve a more detailed investigation in the future.

References

[1] M. G. Silveirinha, C. A. Fernandes, "Transverse-average field approach for the characterization of thin metamaterials slabs", *Phys. Rev. E*, vol. 75, p. 036613, 2007.

[2] M. G. Silveirinha, "Additional Boundary Condition for the Wire Medium", *IEEE Trans. Antennas Propag.*, vol. 54, p. 1766, 2006.

[3] CST Microwave Studio 2010 (http://www.cst.com).